

# Fluid Structure Interaction of a Submerged Flexible Circular Cylinder Mounted on an Experimental Rig

by

© *Erkan Cakir, B. Sc.*

A thesis submitted to the  
School of Graduate Studies  
in partial fulfilment of the requirements for the degree of  
Master of Engineering

Department of *Ocean and Naval Architectural Engineering*  
Memorial University of Newfoundland

*October 2016*

St. John's

Newfoundland

Canada

## **Abstract**

This study aims to develop a numerical tool for investigating the FSI and dynamic reactions of a scale model of a deeply submerged cylindrical flexible offshore structure mounted on an experimental rig that will be used for future studies. The flow around a finite cylinder with an aspect ratio of four causes smaller drag and lift forces compared to an infinite cylinder. However, for cylinders with flexible material properties these forces cause non-negligible deformations which require the investigation of FSI. For this purpose, a two-way coupled partitioned approach was used by coupling the FLUENT and Transient Structural modules in ANSYS with the help of dynamic meshing algorithms in order to communicate force and deformation data alternately between the solvers. Compared to two-way coupling, one-way coupling demands less effort and computational resources, however, it overestimates the deformations for the flexible cylinder. Two-way coupling requires more effort and computational resources, yet it is advantageous enough to justify extra work and computational resources.

## Acknowledgements

I would like to express my sincerest thanks and appreciation to my supervisors Dr. Bruce Colbourne and Dr. Ayhan Akinturk, without whose support and guidance this research would not be possible. Also to Dr. Alejandro Allievi whose guidance is valued.

My gratitude also goes to Dr. Bruce Quinton, for his remarkable help, knowledge and patience concerning my use of the MUN Engineering Cluster.

I would also like to acknowledge the support and help from my friends particularly from Ms. Rebecca Jenkins, who was a great friend and support during my research.

Finally, a sincere thank you to my parents and my family who supported me in every possible way with their understanding, patience and encouragement throughout my entire time in St. John's at Memorial University. Without your sacrifices I would not be able to achieve this degree.

This thesis is dedicated to you.

# Contents

|  |             |
|--|-------------|
| <b>Abstract</b>  | <b>ii</b>   |
| <b>Acknowledgements</b>                                  | <b>iii</b>  |
| <b>List of Tables</b>                                    | <b>viii</b> |
| <b>List of Figures</b>                                   | <b>ix</b>   |
| <b>Nomenclature</b>                                      | <b>xv</b>   |
| <b>Abbreviations</b>                                     | <b>xvii</b> |
| <b>1 Introduction</b>                                    | <b>1</b>    |
| 1.1 Background . . . . .                                 | 1           |
| 1.2 Scope and Objectives . . . . .                       | 3           |
| <b>2 Literature Review</b>                               | <b>5</b>    |
| 2.1 Hydrodynamics Background . . . . .                   | 5           |
| 2.1.1 Flow Around a Circular Cylinder . . . . .          | 6           |
| 2.1.1.1 Flow Regimes Around a Two-Dimensional Cylinder . | 7           |

|          |   |           |
|----------|---|-----------|
| 2.2      | Review of the Literature . . . . .                      | 11        |
| 2.2.1    | Experimental Studies . . . . .                          | 12        |
| 2.2.1.1  | Separation . . . . .                                    | 12        |
| 2.2.1.2  | Fluid forces on the cylinder . . . . .                  | 13        |
| 2.2.1.3  | Vortex Shedding . . . . .                               | 15        |
| 2.2.2    | Computational Fluid Dynamics . . . . .                  | 19        |
| 2.3      | Structural Analysis . . . . .                           | 25        |
| 2.4      | Fluid-Structure Interaction . . . . .                   | 27        |
| 2.4.1    | Monolithic Approach . . . . .                           | 28        |
| 2.4.2    | Partitioned Approach . . . . .                          | 29        |
| <b>3</b> | <b>Methodology</b>                                      | <b>33</b> |
| 3.1      | Experimental Rig Design . . . . .                       | 33        |
| 3.2      | Assumptions and Simplifications . . . . .               | 42        |
| 3.3      | Numerical Structural Model . . . . .                    | 43        |
| 3.3.1    | Geometry . . . . .                                      | 44        |
| 3.3.2    | Computational FE Mesh . . . . .                         | 45        |
| 3.3.2.1  | Mesh Dependence Study for Structural FE Model . . . . . | 46        |
| 3.3.3    | Simulation Setup . . . . .                              | 51        |
| 3.3.3.1  | Materials . . . . .                                     | 52        |
| 3.3.3.2  | Boundary Conditions . . . . .                           | 52        |
| 3.4      | Numerical Fluid Flow Model . . . . .                    | 55        |
| 3.4.1    | Geometry . . . . .                                      | 55        |
| 3.4.2    | Computational Fluid Mesh . . . . .                      | 57        |

|          |   |           |
|----------|---|-----------|
| 3.4.2.1  | Mesh Dependence Study for Wall to Wall Cylinder . . . | 57        |
| 3.4.2.2  | Mesh Dependence Study for Truncated Cylinder . . .    | 64        |
| 3.4.2.3  | Mesh Optimization for Experimental Rig in Flow . . .  | 73        |
| 3.4.3    | Turbulence Model . . . . .                            | 76        |
| 3.4.3.1  | Near Wall Treatment . . . . .                         | 80        |
| 3.4.4    | Simulation Setup . . . . .                            | 82        |
| 3.4.4.1  | Boundary Conditions . . . . .                         | 82        |
| 3.4.4.2  | Solver Settings . . . . .                             | 85        |
| 3.4.4.3  | Time Step Dependence Study for CFD Model . . . . .    | 86        |
| 3.5      | System Coupling . . . . .                             | 88        |
| 3.5.1    | One-Way Coupling . . . . .                            | 89        |
| 3.5.2    | Two-Way Coupling . . . . .                            | 90        |
| 3.6      | Different Simulation Cases . . . . .                  | 93        |
| <b>4</b> | <b>Results and Discussion</b>                         | <b>94</b> |
| 4.1      | Validation of the CFD Model . . . . .                 | 94        |
| 4.2      | Investigated Cases . . . . .                          | 102       |
| 4.2.1    | Base case . . . . .                                   | 103       |
| 4.2.2    | Case 1 . . . . .                                      | 106       |
| 4.2.3    | Case 2 . . . . .                                      | 109       |
| 4.2.4    | Case 3 . . . . .                                      | 111       |
| 4.2.5    | Case 4 . . . . .                                      | 115       |
| 4.3      | Comparison of the Cases . . . . .                     | 119       |

|          |   |            |
|----------|---|------------|
| 4.3.1    | Comparison of Hydrodynamic Cylinder Forces and Structural Responses . . . . . | 119        |
| 4.3.1.1  | Comparison of the Rig Endurance Calculation . . . . .                         | 132        |
| 4.4      | Summary . . . . .   | 141        |
| <b>5</b> | <b>Conclusion and Recommendations</b>   | <b>143</b> |
| 5.1      | Conclusion . . . . .  | 143        |
| 5.2      | Recommendations . . . . .   | 145        |
|          | <b>Bibliography</b>   | <b>147</b> |
| <b>A</b> | <b>Velocity Plots for CFD Solutions</b>                                       | <b>156</b> |

# List of Tables

|      |   |     |
|------|---|-----|
| 3.1  | Hydrodynamic Forces on the Rig . . . . .                              | 47  |
| 3.2  | Element size and node count . . . . .                                 | 48  |
| 3.3  | von-Mises Stresses . . . . .  | 48  |
| 3.4  | Deformations . . . . .  | 49  |
| 3.5  | Changes in von-Mises Stresses and deformations for different meshes . | 49  |
| 3.6  | Mesh convergence study for wall to wall cylinder . . . . .            | 59  |
| 3.7  | Mesh convergence study for wall to wall cylinder . . . . .            | 64  |
| 3.8  | Meshing parameters for truncated cylinder mesh study . . . . .        | 65  |
| 3.9  | Meshing parameters for additional meshes . . . . .                    | 66  |
| 3.10 | Meshing parameters for mesh convergence study for truncated cylinder  | 67  |
| 3.11 | CFD Boundary Conditions . . . . .                                     | 84  |
| 3.12 | FLUENT Solver Settings . . . . .                                      | 85  |
| 3.13 | Parameters . . . . .  | 87  |
| 3.14 | Different simulation cases . . . . .                                  | 93  |
| 4.1  | FSI Cases . . . . .   | 103 |
| 4.2  | Highest deformations of the cylinder . . . . .                        | 130 |
| 4.3  | Highest deformations on the rig (plate) . . . . .                     | 132 |

# List of Figures

|     |  |    |
|-----|--|----|
| 2.1 | Creeping flow [1] (adapted with permission) . . . . .  | 7  |
| 2.2 | Attached eddies [1] (adapted with permission) . . . . .  | 8  |
| 2.3 | Laminar vortex shedding by Heseltine[1] (adapted with permission) .                              | 9  |
| 2.4 | Flow in subcritical regime by Heseltine[1] (adapted with permission) .                           | 9  |
| 2.5 | Flow in critical regime by Heseltine[1] (adapted with permission) . . .                          | 10 |
| 2.6 | Flow in supercritical regime by Heseltine[1] (adapted with permission)                           | 11 |
| 2.7 | Flow in transcritical regime by Heseltine[1] (adapted with permission)                           | 11 |
| 2.8 | Vortex structure around cylinders with different aspect ratios, by Kawamura et al. [2] . . . . . | 13 |
| 3.1 | Experimental rig perspective view . . . . .  | 35 |
| 3.2 | Experimental rig front view . . . . .  | 36 |
| 3.3 | Experimental rig top view . . . . .  | 37 |
| 3.4 | Experimental rig side view . . . . .   | 38 |
| 3.5 | Stiffener frame underneath the plate . . . . .   | 39 |
| 3.6 | Experimental rig in towing tank . . . . .  | 40 |
| 3.7 | Structural geometry . . . . .  | 45 |
| 3.8 | Rig meshing parameters . . . . .   | 46 |

|      |  |    |
|------|--|----|
| 3.9  | Structural mesh . . . . .  | 50 |
| 3.10 | Structural mesh convergence study . . . . .  | 51 |
| 3.11 | Rig structural model . . . . .   | 53 |
| 3.12 | CFD domain view . . . . .  | 56 |
| 3.13 | Wall to wall cylinder mesh study focus area, around the cylinder . . .                         | 58 |
| 3.14 | Drag coefficients over flow time for wall to wall cylinder mesh study .                        | 60 |
| 3.15 | Lift coefficients over 3.25 sec of flow time for wall to wall cylinder mesh<br>study . . . . . | 61 |
| 3.16 | $C_L$ RMS values for wall to wall cylinder mesh study . . . . .                                | 62 |
| 3.17 | Strouhal number for wall to wall cylinder mesh study . . . . .                                 | 63 |
| 3.18 | Meshing parameters for the truncated cylinder . . . . .  | 66 |
| 3.19 | Aspect ratio calculation, from [3] . . . . .   | 68 |
| 3.20 | Drag coefficients over flow time for truncated cylinder mesh study . .                         | 69 |
| 3.21 | Lift coefficients over flow time for truncated cylinder mesh study . . .                       | 70 |
| 3.22 | Drag Coefficient convergence . . . . .   | 71 |
| 3.23 | Lift Coefficient RMS convergence . . . . .   | 72 |
| 3.24 | $C_L RMS$ vs. element aspect ratio . . . . .   | 72 |
| 3.25 | Strouhal vs. element aspect ratio . . . . .  | 73 |
| 3.26 | CFD mesh views . . . . .   | 75 |
| 3.27 | Near wall region divisions, from [4] . . . . .   | 80 |
| 3.28 | Wall functions, from [4] . . . . .   | 81 |
| 3.29 | Strouhal convergence . . . . .   | 87 |
| 3.30 | Workbench coupling work scheme . . . . .   | 88 |
| 3.31 | One-way coupling scheme . . . . .  | 90 |

|      |   |     |
|------|---|-----|
| 3.32 | Coupling setup, one-way (left) and two-way (right) . . . . .                    | 91  |
| 3.33 | Two-way coupling scheme . . . . .   | 92  |
| 4.1  | Pressure coefficients for a circular cylinder from literature . . . . .         | 96  |
| 4.2  | Drag coefficients for circular cylinder from literature . . . . .               | 97  |
| 4.3  | RMS lift coefficient for circular cylinder from literature . . . . .            | 98  |
| 4.4  | Ratio of lift force coefficient on finite cylinder to that on infinite cylinder | 99  |
| 4.5  | Strouhal number for circular cylinder from literature . . . . .                 | 101 |
| 4.6  | Lift and drag coefficients for base case over time . . . . .                    | 104 |
| 4.7  | Cylinder directional deformations for base case . . . . .                       | 105 |
| 4.8  | Base case maximum von-Mises stress over time . . . . .                          | 105 |
| 4.9  | Base case peak von-Mises Stress . . . . .                                       | 106 |
| 4.10 | Case 1 cylinder directional deformations vs. force coefficients over time       | 107 |
| 4.11 | Case 1 von-Mises stress on the rig . . . . .                                    | 108 |
| 4.12 | Case 2 cylinder directional deformations vs. force coefficients over time       | 109 |
| 4.13 | Case 2 von-Mises stress on the rig . . . . .                                    | 110 |
| 4.14 | Case 3 lift and drag coefficients over time . . . . .                           | 111 |
| 4.15 | Case 3 directional deformations of cylinder on X and Y axes . . . . .           | 112 |
| 4.16 | Case 3 cylinder directional deformations vs. force coefficients over time       | 113 |
| 4.17 | Case 3 von-Mises stress on the rig . . . . .                                    | 114 |
| 4.18 | Case 4 lift and drag coefficients over time . . . . .                           | 115 |
| 4.19 | Case 4 directional deformations of cylinder on X and Y axes . . . . .           | 116 |
| 4.20 | Case 4 cylinder directional deformations vs. force coefficients over time       | 117 |
| 4.21 | Case 4 von-Mises stress on the rig . . . . .                                    | 118 |

|      |   |     |
|------|---|-----|
| 4.22 | Comparison of drag coefficients for one-way (Case 1, 2) and two-way (Case 3) cases . . . . .          | 120 |
| 4.23 | Comparison of one-way and two-way directional deformations along x axis . . . . .                     | 120 |
| 4.24 | Comparison of drag coefficients for one-way (Case 1, 2) and two-way (Case 4) cases . . . . .          | 121 |
| 4.25 | Comparison of one-way and two-way directional deformations along x axis . . . . .                     | 122 |
| 4.26 | Comparison of drag coefficients for all cases . . . . .   | 123 |
| 4.27 | Comparison of lift coefficients for one-way (Case 1, 2) and two-way coupling (Case 3) cases . . . . . | 124 |
| 4.28 | Comparison of one-way and two-way directional deformations along y axis . . . . .                     | 125 |
| 4.29 | Comparison of lift coefficients for one-way (Case 1, 2) and two-way (Case 4) cases . . . . .          | 126 |
| 4.30 | Comparison of one-way and two-way directional deformations along y axis . . . . .                     | 127 |
| 4.31 | Comparison of lift coefficients for all cases . . . . .   | 129 |
| 4.32 | Deformations of the cylinder solved with one-way coupling . . . . .                                   | 131 |
| 4.33 | Deformations of the cylinder solved with two-way coupling . . . . .                                   | 131 |
| 4.34 | Deformations of rig for all cases . . . . .   | 133 |
| 4.35 | Maximum deformation on the rig for one-way coupling . . . . .   | 134 |
| 4.36 | Maximum deformation on the rig for two-way coupling . . . . .   | 134 |

|   |     |
|---|-----|
| 4.37 Case 1 FSI von-Mises vs. flow velocity and pressure at highest deformation . . . . .         | 136 |
| 4.38 Case 2 FSI von-Mises vs flow velocity and pressure at highest deformation                    | 137 |
| 4.39 Case 3 FSI von-Mises vs. flow velocity and pressure at highest deformation . . . . .         | 138 |
| 4.40 Case 4 FSI von-Mises vs. flow velocity and pressure at highest deformation . . . . .         | 139 |
| 4.41 Maximum von-Mises stress on rig for all cases . . . . .                                      | 140 |
| A.1 Velocity plots on horizontal and vertical planes at time=0.25 sec for one-way cases . . . . . | 157 |
| A.2 Velocity plots on horizontal and vertical planes at time=0.50 sec for one-way cases . . . . . | 158 |
| A.3 Velocity plots on horizontal and vertical planes at time=0.75 sec for one-way cases . . . . . | 159 |
| A.4 Velocity plots on horizontal and vertical planes at time=1.00 sec for one-way cases . . . . . | 160 |
| A.5 Velocity plots on horizontal and vertical planes at time=1.25 sec for one-way cases . . . . . | 161 |
| A.6 Velocity plots on horizontal and vertical planes at time=1.50 sec for one-way cases . . . . . | 162 |
| A.7 Velocity plots on horizontal and vertical planes at time=1.75 sec for one-way cases . . . . . | 163 |

|      |   |     |
|------|---|-----|
| A.8  | Velocity plots on horizontal and vertical planes at time=2.00 sec for one-way cases . . . . . | 164 |
| A.9  | Velocity plots on horizontal and vertical planes at time=2.25 sec for one-way cases . . . . . | 165 |
| A.10 | Velocity plots on horizontal and vertical planes at time=2.50 sec for one-way cases . . . . . | 166 |
| A.11 | Velocity plots on horizontal and vertical planes at time=0.10 sec for Case 3 . . . . .        | 167 |
| A.12 | Velocity plots on horizontal and vertical planes at time=0.20 sec for Case 3 . . . . .        | 168 |
| A.13 | Velocity plots on horizontal and vertical planes at time=0.30 sec for Case 3 . . . . .        | 169 |
| A.14 | Velocity plots on horizontal and vertical planes at time=0.40 sec for Case 3 . . . . .        | 170 |
| A.15 | Velocity plots on horizontal and vertical planes at time=0.10 sec for Case 4 . . . . .        | 171 |
| A.16 | Velocity plots on horizontal and vertical planes at time=0.20 sec for Case 4 . . . . .        | 172 |
| A.17 | Velocity plots on horizontal and vertical planes at time=0.25 sec for Case 4 . . . . .        | 173 |
| A.18 | Velocity plots on horizontal and vertical planes at time=0.40 sec for Case 4 . . . . .        | 174 |

# Nomenclature

|   |   |
|---|---|
| $A_0, A_S$                              | Realizable K- $\varepsilon$ model constants                         |
| $C_D$                                   | Drag coefficient  |
| $C_L$                                   | Lift coefficient  |
| $C'_L$                                  | RMS value of lift coefficient                                       |
| $C_\mu$                                 | Eddy viscosity coefficient  |
| $(C)$                                   | Damping matrix  |
| $D$                                     | Diameter of cylinder  |
| $[D]$                                   | Elastic stiffness matrix  |
| $E$                                     | Young's modulus   |
| $\gamma_{yz}, \gamma_{xz}, \gamma_{xy}$ | Shear strains   |
| $\{\varepsilon\}$                       | Strain vector   |
| $G$                                     | Shear modulus   |
| $(K)$                                   | Stiffness matrix  |
| $(M)$                                   | Mass matrix   |
| $N_c$                                   | Number of circumferential elements                                  |
| $N_y$                                   | Number of elements in normal direction to circumference of cylinder |

|                          |   |
|--------------------------|---|
| $N_z$                    | Number of elements along height of cylinder |
| $Re$                     | Reynolds number                             |
| $St$                     | Strouhal number                             |
| $U$                      | Flow velocity                               |
| $\{u\}$                  | Nodal displacement vector                   |
| $\{\dot{u}\}$            | Nodal velocity vector                       |
| $\{\ddot{u}\}$           | Nodal acceleration vector                   |
| $Y_+, (Y_{plus})$        | Dimensionless wall distance                 |
| $[\sigma]$               | Stress vector                               |
| $\sigma_e$               | von-Mises Stress                            |
| $\rho$                   | Density                                     |
| $\mu$                    | Dynamic viscosity                           |
| $\mu_t$                  | Turbulent viscosity                         |
| $\nu$                    | Kinematic viscosity                         |
| $\bar{u}_i, u'_i$        | Mean and fluctuating velocity components    |
| $\nu_t$                  | Eddy viscosity                              |
| $\overline{\Omega_{ij}}$ | The mean rate-of-rotation tensor            |
| $\omega_k$               | Angular velocity                            |

# Abbreviations

|        |   |
|--------|---|
| CFD    | Computational fluid dynamics                                    |
| DES    | Detached-Eddy Simulations                                       |
| FE     | Finite element  |
| FEM    | Finite element method   |
| FSI    | Fluid-structure interaction                                     |
| FVM    | Finite volume method  |
| ID, OD | Inner diameter, outer diameter                                  |
| LE     | Large-Eddy  |
| LES    | Large-Eddy simulations  |
| OERC   | Ocean Engineering Research Center                               |
| PCG    | Preconditioned Conjugate Gradient                               |
| PISO   | Pressure Implicit with Splitting of Operator                    |
| RANS   | Reynolds Averaged Navier-Stokes                                 |
| QUICK  | Quadratic Upstream Interpolation for Convective Kinetics scheme |
| SST    | Shear Stress Transport  |
| URF    | Under relaxation factors  |

# Chapter 1

## Introduction

### 1.1 Background

In recent years, the advancement of the oil and gas industry into deeper waters and harsher environments has increased the need for safer and more advanced engineering solutions. Considering both safety and financial costs, the performance prediction of these engineering solutions under the aforementioned conditions are a highly significant part of the design process.

Flexible structures are relatively new in offshore applications. Due to their large deformations under load, conventional numerical analyses are not sufficient to predict the behaviour and stresses in highly flexible structures. Thus the complexity of the required engineering analysis increased and the need for higher accuracy of numerical simulations arose. This necessitates the consideration of more than one single physical factor [5], rather than only hydrodynamics or structural aspects. Moreover, with the increasing significance of these factors' influence on the response of the system, fluid-

structure interactions carry greater importance than just the sum of the structural or hydrodynamic aspects of the problem. The underlying reason for this is the inherent mutual dependence between the structural responses and fluid dynamics aspects of the problem. The flow behaviour around the structure is defined by the shape of the structure whereas the motion and the deformations of the structure are defined by the forces acting on the structure from the fluid. As a result, with the increasing significance of these mutual influences and responses on each other, fluid-structure interaction effects carry great importance.

However, in modeling and computational calculations, FSI problems can be the most challenging problems to simulate. Due to the complexity of the multi-physics problems combined with the non-linear and time dependent nature of FSI, it is generally challenging to solve this class of problem analytically. There are still relatively few published cases in which FSI problems have been studied analytically, although significant computational FSI research has been conducted in the last decades. In engineering applications FSI carries a significant role in the design procedure resulting in a requirement for numerical simulations or experiments in order to predict the performance of the flexible system. In addition, the choice of an appropriate solution method for a FSI problem is crucial when developing a numerical tool. The monolithic approach aims to solve all fluid flow and structural displacement equations simultaneously. However, the partitioned approach uses more specified and advanced solvers which were developed particularly for structural or fluid simulations. Companies like ANSYS, COMSOL and CD-adapco have developed efficient multi-physics software with versatile features in the last decades. These commercial codes let users choose the specific solvers for their requirements while dealing with fluid and structural me-

chanics aspects along with their close relations within the system. Despite all the improvements on computational FSI, the use of the method is still challenging.

## 1.2 Scope and Objectives

Due to the shape dependency of hydrodynamic forces on structures and the structural deformations resulting from hydrodynamic loads, current problems require exclusive analysis for each application. Considering the wide use of cylindrical shaped structures such as risers, moored and tethered structures along with sub sea umbilicals and spar hulls, this study focuses on FSI investigation of an assembly composed of a fixed cylinder with flexible material properties mounted on a test rig designed for future experimental investigations. One-way and two-way coupled partitioned approach was used by the aid of ANSYS Workbench environment using Mechanical and Fluent solvers. Since the one-way coupled partitioned approach only transmits force values one way between the solvers, this approach lacks displacement effects on the hydrodynamic loads. This causes a lack of accuracy when the effect of deformations on the structure is significant. Thus, it can only be used when the deformations of the system are small or can be neglected. On the other hand, the two-way coupled method sends deformation values to the fluid solvers by upgrading the mesh of the fluid domain for every time step of the solution. This method provides a more realistic and advanced simulation of the physical problem especially when the deformations are large and their resulting effects on the hydrodynamic loads are significant.

This study aims to develop a numerical model and method for simulating the deformations and dynamic reactions of a scale model of a deeply submerged cylindrical

flexible offshore structure mounted on a supporting measurement rig that will be used for future experimental studies. For this purpose, a two-way coupled partitioned approach was used for the FSI problem by coupling the FLUENT and Transient Structural Analysis modules in the ANSYS Workbench environment. This allows both the investigation of the realistic behaviour of the cylindrical structure and the testing the endurance of the designed experimental rig.

# Chapter 2

## Literature Review

The work proposed for this thesis is a coupled model of a circular cylinder in a steady flow in which both the hydrodynamic forces and the structural responses are modeled simultaneously. This is a relatively new area in numerical FEA modeling and as such, there are relatively few studies of such coupled modeling. There are however, a large number of studies in which either fluid models or structural models are exercised separately. The purpose of this chapter is to review the current state of the art in fluid and structural modeling and to cover the smaller body of literature on coupled modeling in order to provide a better understanding of the fluid-structure interaction of the proposed submerged flexible cylinder.

### 2.1 Hydrodynamics Background

The flow around a circular cylinder has long been a focus of interest. The following section provides a summary of the flow around a circular cylinder from references [6],[7] and aims to provide insight into the basic flow regimes around a cylinder,

dependent mainly on flow velocity.

### 2.1.1 Flow Around a Circular Cylinder

When a fluid flow encounters an obstacle, the flow is required to move around the body and is thus disturbed from its previous path. The same occurs in the case of an obstacle moving within the flow. Though there are a wide variety of parameters that affect the nature and form of the flow deviation, the most important ones can be identified as the shape and size of the body, the velocity of the flow and the viscosity of the fluid. Reynolds introduced a numerical relation between these parameters, known as Reynolds number (Re), which has been the most important variable used to categorize the flow around cylinders since 1883 [8]. Reynolds number refers to the ratio between inertia and viscosity forces and can be written as below for a smooth circular cylinder where the diameter of the cylinder is shown as D, the velocity of the flow is U and  $\nu$  represents the kinematic viscosity.

$$Re = \frac{DU}{\nu} \quad (2.1)$$

Along with Reynolds number, the flow around a cylinder is affected by other parameters such as the effects of nearby boundaries, the aspect ratio of cylinder height over cylinder diameter, the surface roughness of the cylinder and the existence of a free end (three-dimensional effects). In this study, the cylinder surface is presumed smooth, thus the effects of roughness were not considered. In order to learn more about flow around a circular cylinder, flow regimes, which are significantly affected by relative flow speed, must be understood. Flow patterns show significant changes under different conditions, thus the identification of differences and similarities between

flow behaviours are required as a function of Reynolds number.

### 2.1.1.1 Flow Regimes Around a Two-Dimensional Cylinder

Two-dimensional flow around a smooth circular cylinder shows significant similarities with three-dimensional flow and presents a simplified understanding of the flow regimes which can be slightly modified later to account for three-dimensional effects. The three-dimensional flow investigations around the cylinder will be discussed later for comparison. References [6] and [7] have divided the flow around a two-dimensional cylinder into different Reynolds number regimes according to hydrodynamic forces, vortex formation, flow structure and boundary layer characteristics. These regimes are briefly reviewed in the following sections.

#### Creeping Flow, $Re < 5$

For very small  $Re$ , such as values less than 5, the flow moves around the cylinder and does not separate from the cylinder with the flow pattern as seen in Figure 2.1 by [1]. Separation, which is the detachment of flow streamlines from the surface of the body and the creation of turbulent flow in the wake, begins when the  $Re$  reaches 5 and the length of the wake increases with subsequent increases of the  $Re$ .

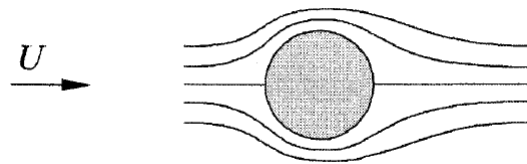


Figure 2.1: Creeping flow [1] (adapted with permission)

### **Attached Eddies, $5 < Re < 40$**

As shown in Figure 2.2 [1], flow separation behind the body leads to formation of a pair of attached vortices (or eddies) that develop symmetrically behind the cylinder as the  $Re$  increases to a value of 40. The flow separation occurs at approximately  $80^\circ$  from the forward stagnation point, which is the point on the front of the body where the velocity is zero. The length of the attached vortex structure behind the body increases with increasing  $Re$ .

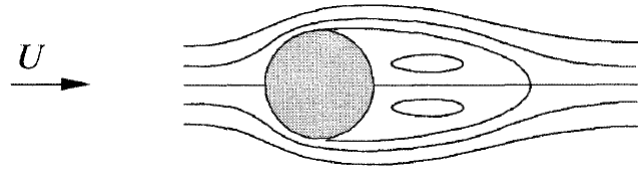


Figure 2.2: Attached eddies [1] (adapted with permission)

### **Laminar Vortex Regime, $40 < Re < 350$**

With increasing Reynolds number, the wake behind the cylinder becomes unstable resulting in the shedding of the attached vortices as shown in Figure 2.3 [1]. When the Reynolds number is between 40 and 200, the detaching vortices form a laminar vortex street showing only two-dimensionality. As mentioned by Sumer in [6], Bloor [9] reported that as the  $Re$  increases further, transition of the turbulent flow in the wake approaches the cylinder and the vortices that form at Reynolds numbers bigger than 300 show turbulent behaviour in the wake and present three-dimensionality. In other words, vortex shedding varies across the span of the cylinder.



Figure 2.3: Laminar vortex shedding by Heseltine[1] (adapted with permission)

**Subcritical Regime,  $350 < Re < 2 \times 10^5$**

For a Reynolds number greater than 300, the wake behind a cylinder becomes completely turbulent while the boundary layer on the cylinder continues to be laminar. A non-dimensional Strouhal number generally describes the oscillation of the flow. When the Reynolds number is between 350 and  $2 \times 10^5$ , in the subcritical regime, a fully turbulent Karman vortex street forms with a nearly constant Strouhal number of 0.20. With an increasing  $Re$ , the length of the vortex formation behind the cylinder shrinks. In this regime, the drag coefficient is usually 1.2. Demonstration of the flow can be seen in Figure 2.4.



Figure 2.4: Flow in subcritical regime by Heseltine[1] (adapted with permission)

**Critical Regime,  $2 \times 10^5 < Re < 7 \times 10^5$**

$Re = 2 \times 10^5$  is known as the critical Reynolds number. When the  $Re$  is between  $3 \times 10^5$  and  $3.5 \times 10^5$ , the boundary layer on one side of the cylinder becomes turbulent at the separation point. This results in a laminar boundary layer on one side and

a turbulent boundary layer on the other side. As shown in Figure 2.5, during this process, turbulent separation switches sides alternately, causing a small lift force that changes direction from one side to another. The wake is at its shortest length when the  $Re$  is  $3 \times 10^5$ . This point, also known as the drag crisis, is where the drag coefficient drops drastically from the value of 1.2 to 0.3 and the Strouhal number increases to 0.46 from 0.2 [1].



Figure 2.5: Flow in critical regime by Heseltine[1] (adapted with permission)

**Supercritical Regime,  $7 \times 10^5 < Re < 3.5 \times 10^6$**

The next flow regime is called supercritical flow regime for a  $Re$  between  $7 \times 10^5$  and  $3.5 \times 10^6$ . In this regime, the separation of boundary layer becomes fully turbulent on both sides of the cylinder when  $Re$  reaches  $1.5 \times 10^6$ . However, a full transition within the boundary layer is not completed. Within the upper-transition flow regime, which extends up to the Reynolds number of  $4.5 \times 10^6$ , the boundary layer displays fully turbulent behaviour on one side of the cylinder and shows a combination of laminar and turbulent behaviour on the other side of the cylinder. Flow behavior in this regime is shown in Figure 2.6.

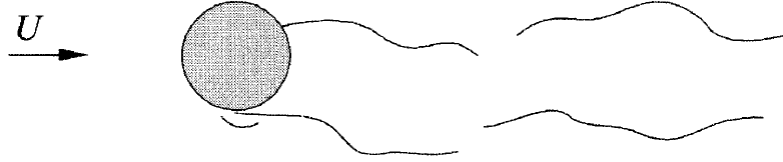


Figure 2.6: Flow in supercritical regime by Heseltine[1] (adapted with permission)

### Transcritical Regime, $Re > 3.5 \times 10^6$

As the  $Re$  reaches  $4.5 \times 10^6$  and extends to the larger values within the transcritical flow regime, the boundary layer becomes fully turbulent. As shown in Figure 2.7, separation bubbles do not form and the drag value increases from 0.5 to 0.7 where the  $St$  shows a near constant value of 0.30 [1].



Figure 2.7: Flow in transcritical regime by Heseltine[1] (adapted with permission)

## 2.2 Review of the Literature

Until the 1980s, it appears that the experimental work on circular cylinders generally involved two-dimensional flows. Subsequently several experiments have been done on finite cylinders where the presence of the free-end affects the three-dimensionality of the flow. Several authors tried to explain this effect [10], [2], [11]. Even though this

study focuses on the Fluid-Structure interaction of a relatively short flexible cylinder and supporting experimental rig, the literature review was guided by the availability of literature covering the constituent ideas of flow phenomena.

## 2.2.1 Experimental Studies

### 2.2.1.1 Separation

Compared to the two-dimensional cylinder, numerous authors reported a shifted separation point towards the stagnation point of the cylinder for the three-dimensional flow past a finite length cylinder. Luo [11] performed experiments within the sub-critical regime in an open loop wind tunnel using smoke wire flow visualization. He measured the separation angle from the stagnation point as  $80^\circ$  to  $85^\circ$  for normal conditions, however, he noted that it might delay until  $90^\circ$  near the free end for cylinders with an aspect ratio of 8 or less.

Okamoto et al. [10] reported an unchanged separation point for cylinders with a length to diameter ratio equal to and greater than 12, however, a forward move was measured with ratios smaller than 12. This was attributed to an increased base pressure associated with the existence of a free end with a decreasing length to diameter ratio. On the other hand, Kawamura et al. [2] observed a similar forward shift of the separation point with decreasing length to diameter ratio from oil-film photographs. However, they argued that this shift should be attributed to the decrease of acceleration of the side flow. Furthermore, this decrease in acceleration can be attributed to the three-dimensionality of the flow resulting in a lower separation velocity than that of the two-dimensional flow. In addition, Kawamura et al. [2] re-

ported a reattachment of the separated flow for cylinders with an aspect ratio of 8 or less and observed a "mushroom" type vortex flow in the absence of this reattachment. Moreover, Kawamura et al. [2] modelled the flow for cylinders with values above and below the critical aspect ratio as shown in Figure 2.8.

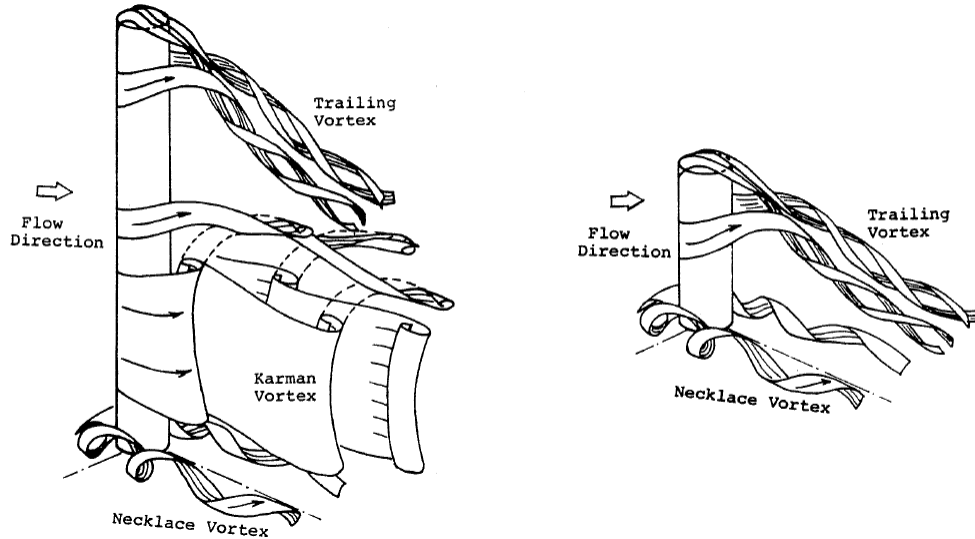


Figure 2.8: Vortex structure around cylinders with different aspect ratios, by Kawamura et al. [2]

### 2.2.1.2 Fluid forces on the cylinder

Understanding the fluid flow loading on offshore structures is important in optimizing their design to minimize the dangerous effects of fluid loads. Much work has been done to measure hydrodynamic forces on the cylinder with different flow regimes using force and pressure based methods [12].

Before Roshko[13]'s study, the existence of the transcritical flow regime was not recognized [14]. Roshko [13] performed experiments on cylinders in both supercritical

and transcritical flow regimes with a Reynolds number varying between  $1 \times 10^6$  and  $1 \times 10^7$ . He measured the drag coefficient as 0.7 at  $Re = 3.5 \times 10^6$  which is an increase from its value of 0.3 at  $Re = 1 \times 10^6$ . Moreover, similar to Achenbach & Heinecke [15]’s findings, he reported a constant trend for the drag coefficient for the rest of the supercritical regime. On the contrary, Delany & Sorensen [16] measured the drag coefficient between  $Re = 11000$  and  $2.3 \times 10^5$  and reported a significantly different drag value for the subcritical regime due to the gaps in their wind tunnel. Nevertheless, their measurements of critical Reynolds number  $5 \times 10^5$  and  $6 \times 10^5$  were in agreement with the other authors. Within the critical regime, several authors detected a steep decrease in drag force. This phenomenon, known as the drag crisis, was attributed to laminar separation bubbles by numerous authors. Schewe [17] conducted wind tunnel experiments from a subcritical regime to the transcritical Reynolds numbers  $2.3 \times 10^4 - 7.1 \times 10^6$  and measured the forces on the cylinder with a 3-component piezoelectric force-measuring element. He observed a steeper decline in  $C_D$  for  $Re < 50000$  compared to previous experiments due to differences in surface roughness of the cylinders tested by other authors. He also mentioned two intermittent drops of  $C_D$ . At  $Re$  around  $3.5 \times 10^5$  he measured  $C_D$  as 0.22 with a stationary trend in  $Re$  up to  $1 \times 10^6$ . Further in the supercritical range, he measured an increased  $C_D$  value of 0.52 until  $Re = 5 \times 10^6$ . Moreover, Schewe [17] also measured  $C_L$  R.M.S. with a maximum value of 0.38 in the subcritical regime and 0.02 in the supercritical regime at  $Re = 3.5 \times 10^6$ . In addition, Bearman [14] also observed a steep decrease in the drag coefficient immediately after the critical range ( $Re = 2 \times 10^5$ ) and noted a minimum value at  $Re = 4.16 \times 10^5$ .

Due to the flow over the end, the flow around a finite cylinder shows significant

differences when compared to the flow around an infinitely long cylinder. One of the most fundamental differences between the finite and infinite cylinders is the difference in flow induced cylinder forces. Many authors have reported a lower mean drag coefficient for a finite cylinder compared to an infinite cylinder due to the presence of a free end. Luo [11] attributed this phenomenon to less negative wake pressure and stated that the mean drag coefficient is always lower for a finite length cylinder. Moreover, on cylinders with aspect ratios between 4 and 30 Fox & West [18] examined the mean pressure distribution at Re of 4400. They observed the direct effect of the cylinder aspect ratio on the local drag. Their circumferential pressure distribution measurements showed a decrease in the local drag value towards the bottom of the cylinder for aspect ratios smaller than 13. However, this effect was not observed for aspect ratios greater than 13. Thus, Fox & West [18] concluded by reporting an increase of the local drag force starting at a distance of 4 diameters from the bottom and reaching the infinite cylinder value at 20 diameters. In addition, Kawamura et al. [2] performed experiments on cylinders mounted on flat plates and calculated the drag coefficient as an integration of the surface pressure. They reported a lower drag coefficient for a finite cylinder than a two-dimensional cylinder due to lower separation velocity of the flow on the side of the cylinder wall. Moreover, they observed a decreasing  $C_D$  with a decreasing aspect ratio. Finally, they concluded that  $C_D$  decreases with a thicker boundary layer from the plate.

### **2.2.1.3 Vortex Shedding**

In addition to the magnitude of the hydrodynamic forces, the oscillation frequency arising from pressure changes associated with vortex shedding is also crucial. One of

the topics for which several authors obtain similar measurements is the investigation of the Strouhal number. For instance, there is strong convergent evidence for the Strouhal value at both the upper supercritical and transcritical regimes. Roshko [13] did not detect regular vortex shedding for  $Re$  between  $0.9 \times 10^6$  and  $3.5 \times 10^6$  during his detailed hot-wire investigation. However, he did report a definite start of vortex shedding at  $Re = 3.5 \times 10^6$  with a Strouhal number of 0.27. Although he extended the investigation up to a higher Reynolds number of  $1 \times 10^7$ , he did not observe the frequencies reported by Delany & Sorensen [16] at a Reynolds number between  $1 \times 10^6$  and  $2 \times 10^6$ . He attributed this inconsistency to a difference in the distance of the probe behind the cylinder. While Roshko's probe was positioned at 7.3 diameters [13], the other authors measurements were made from one or two diameters behind the cylinder.

Similar to Roshko, Achenbach & Heinecke[15] also measured the Strouhal number as 0.25 at  $Re = 4 \times 10^6$  using a hot-wire probe. They also noted a constant Strouhal at 0.205 for subcritical regime. However, they did not find regular signals in the wake of the cylinder beyond the critical regime due to three-dimensionality of the wake formation. Achenbach [19] detected a decrease in Strouhal from a value of 0.5 at  $Re = 1.5 \times 10^6$  to 0.25 from  $Re = 4 \times 10^6$  which, again, shows good agreement with other studies.

Bearman [14] examined the flow over a two-dimensional cylinder between  $Re$  of  $1 \times 10^5$  to  $7 \times 10^5$ . He reported two regular occurrences of shedding: one in the one-bubble range with a Strouhal number of 0.32 and another one in the two-bubble range with a higher Strouhal number of 0.46. Schewe [17] examined flows in the range from the subcritical regime ( $Re = 2.3 \times 10^4$ ) to the transcritical regime ( $7.1 \times 10^6$ ). He

measured the Strouhal number as 0.2 in the subcritical range. In the critical range, he reported two intermittent transitions for Strouhal number, which are coupled with the drop of  $C_D$  and measured Strouhal Number as 0.3 and 0.48. As mentioned in [17], these measured values are confirmed by Bearman (1969) and Achenbach & Heinecke (1981). At supercritical range, Schewe [17] noted a nearly constant Strouhal number. In the upper transition range he measured a decreased Strouhal as 0.4 at  $Re = 2 \times 10^6$ . Finally, at his highest measurement of  $Re = 7.1 \times 10^6$ , he measured the Strouhal number as 0.29. This was close to what Jones et al. measured in 1969 [17]. The Strouhal measurements of Schewe [17] show very good agreement with Roshko's [13] value of 0.27 and Achenbach & Heinecke's [15] Strouhal of 0.25 at  $Re = 4 \times 10^6$ .

When it comes to the differences between finite and infinite cylinder for the Strouhal number, Ayoub and Karamcheti [20] detected a distinct vortex shedding frequency at the free end of the cylinder that differs from the shedding at the main body. They also noted that this shedding could be unstable, intermittent, and generally lower than the frequency of an infinite version of the cylinder.

Most authors measured the vortex shedding frequency from the velocity fluctuations of the flow behind the cylinder. However, Fox & West [18] took a different approach; they analyzed the surface pressure on the cylinder and obtained the Strouhal number based on the fluctuations in pressure. For cylinders with aspect ratios smaller than 13, they reported a relation between the aspect ratio and the Strouhal number. On the other hand, they noted an independent Strouhal number for aspect ratios of 13 and greater. For aspect ratios smaller than 13, they could not detect vortex shedding at the tip of the cylinder. However, they reported an increase in Strouhal number from its minimum value near the tip of the cylinder to its constant value at

around 6 diameters distance in span from the end. In addition, for cylinders with aspect ratios greater than 13, the Strouhal number was constant regardless of the aspect ratio. The described investigations were made at  $Re = 4.4 \times 10^4$ .

During his experiments, Luo [11] detected regular vortex shedding only with a cylinder aspect ratio of 8. Furthermore, he reported a non-uniform wake pressure near the free end due to the strong three-dimensionality of the flow causing disturbance and a slightly smaller Strouhal number compared to the two-dimensional case. Similar to Luo [11], Kawamura et al. [2] also detected periodic vortex shedding for cylinders with an aspect ratio of 8 which was absent for cylinders with an aspect ratio of 4.

Okamoto & Yagita [10] measured the surface pressure on the cylinder and noted a decrease in the Strouhal number with a decreasing aspect ratio. On the other hand, Park & Lee (2000) [21] used a different approach, performing a detailed hot-wire investigation and measuring the wake velocity. Regardless of the different measurement methodology, they also noted that the Strouhal number decreased with a decreasing aspect ratio and attributed this to descending downwash flow. As can be seen from the previous section, the vortex-shedding phenomenon is the most important common feature of all flow regimes. This phenomenon arises from the adverse pressure gradient at the backside of the cylinder caused by the change of the geometry, and is common to all flows with  $Re > 40$ .

Despite the fact that the flow around cylinders has been investigated extensively, there are still unresolved issues. For instance, when a cylinder is placed in a boundary layer the effect of the incoming boundary layer on vortex shedding characteristics are still unknown [22].

## 2.2.2 Computational Fluid Dynamics

Understanding and predicting the flow around cylinders to allow optimization of engineering aspects such as structural design is essential. However, experiments with minimum human and instrumentation error for very high Reynolds number flow conditions are technically challenging and financially expensive. Considering this, computer aided tools to predict and calculate the flow around cylinders are potentially very beneficial. Along with improvements in computer science, both commercial and independent numerical tools have shown significant improvement over the years. In this chapter, some of the numerical methods for calculating the flow around cylinders are discussed. Until the 1970s, computers were not powerful enough to solve Navier-Stokes equations for three dimensional flows [23]. Even later on, numerical studies were limited to laminar flows, coarse meshes, or steady flows, due mainly to computational limitations. As one of the early examples of CFD studies within practical engineering flows, Majumdar and Rodi [23] used the standard K- model with wall functions and finite volume method using the SIMPLE algorithm. The flow simulated was at  $Re = 5 \times 10^5$  and the aspect ratio of the cylinder was two. Even though they reported that the model successfully captured the complex flow features such as separation and vortex systems, the base pressure was calculated as being too high resulting in a lower drag than the experimental measurements. They attributed this to the steady calculation of the flow that could not account for the shedding of the vortices. Over time, turbulence models and calculation methodologies improved in parallel with the computational possibilities; however, until the late 1990s the initial versions of the turbulence models did not suffice when solving complicated

flows and hydrodynamic forces with high accuracy. Menter [24] compared the performances of the four popular turbulence models at the time: The Baldwin-Lomax (BL), Johnson-King (JK), Baldwin-Barth (BB) and Wilcox K- models for solving the flows with adverse pressure gradients. He performed the computations with a numerical method that solved the incompressible RANS equations using the method of pseudo-compressibility. In his study [24], Menter reported an inferior performance for the BL model compared to the rest of the models. The JK model was reported as the superior model owing to its capability of solving both the turbulent shear stress and the shape of the velocity profiles with the highest accuracy. The BB model predicted the pressure coefficient well, however, it was insufficient in determining the velocity profile shapes. On the other hand, the K- $\omega$  model presented better predictions for the velocity profiles but produced excessive turbulent shear stress values. In the case of flows at a Reynolds number greater than 180, it is a known fact that the flow around the cylinder shows three-dimensional effects. However, until the late 1990s, computational fluid simulations were generally conducted in two-dimensions or at low Reynolds numbers. Thanks to the development of high performance computing technologies and new turbulence models, it was possible to extend CFD investigations to higher Re and three-dimensions with higher accuracy.

In 1994, Menter developed two new empirical based eddy-viscosity turbulence models for engineering applications [25]. He stated that these models were developed from the combination of different elements from existing models and the formulations of K- which show the best numerical stability. The new Baseline model (BSL) was developed to utilize the original K- model in the sub and log-layer and to switch to the K- model in the wake region of the boundary layer. By using this strat-

egy, the model avoids the strong free stream dependency of the flow. Secondly, the Shear-Stress Transport Model was designed to provide significant improvements for flows with adverse pressure gradients. The Shear-Stress Transport Model is the only two-equation model that is capable of predicting the pressure-induced separation and viscous-inviscid interaction. These two models require more programming effort compared to the standard  $K$ - model, however, both models were tested for a wide variety of challenging research flows and subsequently fine-tuned. As a result, they show a good performance and high stability.

While RANS models were gaining popularity, early examples of a computationally more intense method, called Large-Eddy Simulations, began to emerge. For instance, Kalro and Tezduyar [26] carried out some of the early examples of LE simulations and performed numerical investigations at Reynolds numbers of 300, 800, and 10 000. They used the simplest version of the Smagorinsky LES model at  $Re=10\ 000$  with 3D finite element formulations and employed the 2D unsteady solutions as the initial boundary conditions. They reported excellent agreement for drag coefficient and Strouhal numbers with experimental results.

Despite the advancements in the development of turbulence modeling, there is unfortunately still no universal model that can be used for all flow applications with high accuracy. On some occasions, the selection of a turbulence model might be challenging. However, the comparison of these models and their most suitable applications can be found in the literature. As seen in the following paragraphs, RANS models have been examined by numerous authors. For instance, Rahman et al. [27] compared the Standard  $K - \varepsilon$ , Realizable  $K - \varepsilon$ , and the Shear-Stress Turbulence (SST)  $K - \omega$  turbulence models for predicting the force coefficients along with the

vortex shedding frequency. They performed the numerical investigation using a 2D finite volume method with a second order numerical scheme. As per the result of their evaluation, they reported that the Standard  $K - \varepsilon$  model was the most successful in predicting the drag coefficient. However, the Realizable  $K - \varepsilon$  captured the separating flow better than the Standard  $K - \varepsilon$  model. Finally, they recommended the (SST)  $K - \omega$  model when dealing with high Reynolds numbers.

Ong et al. [28] evaluated the suitability of the standard  $K - \varepsilon$  model for engineering applications. They carried numerical investigations of flow around a 2D smooth cylinder at  $Re = 1 \times 10^6$ ,  $2 \times 10^6$ , and  $3.6 \times 10^6$  using 2D Unsteady Reynolds-Averaged Navier-Stokes (URANS) equations. They noted that although the mentioned model had drawbacks and lacked a certain level of accuracy for predicting the flow with strong anisotropic turbulence, it still showed satisfactory results for engineering design purposes compared to other numerical [29] and experimental work [19]. With advancements in computer science and access to increased computational capabilities, Large-Eddy Simulations started to gain popularity. However, due to the requirement for more computational power, their feasibility and performance over RANS models was frequently investigated. As an example, Catalano et al. [29] numerically investigated the flow around a cylinder in the supercritical regime and compared the reliability of the LES and RANS solutions. They used a simple wall stress model with a Smagorinsky LES model to provide initial boundary conditions. This made the LES simulations possible by mitigating the requirements for resolving the near wall. On the other hand, the commercial CFD code FLUENT was used with second order finite volume discretization for RANS simulations. Though the simulations they performed were unable to accurately capture the Re dependency and drag coefficient for higher

$Re$  numbers due to the poor grid distribution, they measured the drag coefficient well for  $Re = 0.5 \times 10^6$  and  $1 \times 10^6$ . According to them [29], it is worth noting that LES was more successful than RANS simulations for predicting the delayed boundary layer separation and reduced drag coefficient after the drag crisis, which was also in good agreement with experimental measurements.

Frhlich & Rodi [30] performed numerical LES investigations for cylinders with an aspect ratio of 2.5 and a flow at  $Re = 43000$ . The calculations were made with the finite-volume based LESOCC2 code, which solves the incompressible Navier-Stokes equations on curvilinear block-structured grids [30]. They reported successful solution of the complexity of the flow with the Smagorinsky sub-grid scale model. Furthermore, they detected an arch-type vortex behind the cylinder, which was previously observed for a wall-mounted cube but unprecedented for a cylinder. They attributed this to the small height of the cylinder, which prevented the formation of the two-dimensional von Karman vortices. Similarly, Salvador et al. [31] carried out numerical investigations of the flow around finite cylinders with similar aspect ratios of 2.5 and 5 and a  $Re$  varying between 22000 and 43000. However, they used a finite-volume method based LES code called MGLET on a staggered Cartesian grid. They reported a good agreement with the results of previous experiments by Kappler [32]. The authors [31] noted the requirement of a very fine mesh for the finite cylinders near the free end in order to solve the details of the very complex flow behaviours close to the wall.

Compared to previous researchers, Singh and Mittal [33] took a different approach and used a stabilized finite element method with two-dimensional LES for their studies. However, the objective of their study was not to resolve the three-dimensional

effects of the flow. They aimed to show the connection between the shear layer instability (which was noted as two-dimensional) and drag crisis by numerically investigating the flows between  $Re = 100$  and  $1 \times 10^7$ . They reported that for a  $Re$  greater than 200, their computations were not able to predict the correct drag coefficient as expected. However, they did successfully predict the drag-crisis. One of the challenges of using foremost CFD methods within FSI problems is the requirement of a very fine mesh resulting in excessive computational costs. Thus, this type of application is not widely common within FSI simulations for industrial applications. However, it has been a focus of interest for numerous researchers.

For instance, Lee et al. [34] used one of the new hybrid methods of CFD, detached-eddy simulation (DES), which combines the best aspects of the RANS and LES models. Lee et al. [34] investigated the fluid-structure interaction of a self-oscillating cylinder due to vortex shedding by coupling a delayed-detached-eddy simulation (DDES) and a nonlinear finite element analysis simulation. They investigated the flow past a cylinder with an aspect ratio of 2D at a  $Re$  of 5000 with the aid of an open source software package, OpenFOAM. For the Strouhal number and values of drag and lift coefficients, they reported good agreement with previous experimental work involving numerical models with mesh that featured a  $Y+$  value around 1. In addition, Feymark [35] used an LES based FSI methodology to investigate the hydro-elasticity of a deforming hydrofoil and noted good agreement with the experimental data.

## 2.3 Structural Analysis

In fluid-structure interactions, the oscillating dynamic fluid forces cause deformations on the structure, which conversely results in a change in the fluid forces due to the new shape of the structure. This inherent relation between the structure shape and hydrodynamic forces requires a good prediction of the structural responses. In the fluid-structure interaction investigations of underwater and offshore structures, the finite element method is traditionally the most practical and efficient standard numerical modelling method for investigating structural behaviors [36]. Numerous authors report nonlinear finite element analysis applications within Fluid-Structure Investigations. For instance, Phadke and Cheung [37] studied the nonlinear behaviour of a bottom-mounted membrane under the influence of gravity waves. By using a linear isoparametric element along with an approach originated from the virtual work principle that accounts for geometrical nonlinearities, they examined the membrane deformations by solving the nodal coordinates and deformations as linear functions. In addition, Relvas and Suleman [38] presented a method to model the geometric nonlinearities on an aeroelastic wing as part of an FSI procedure. For the structural aspect of the problem that calculates the nonlinear structural response of the wing, they employed a dynamic co-rotational approximately-energy-conserving algorithm to solve the nonlinear structural responses with existing linear finite element codes. They compared their demonstrated process with the nonlinear implicit Newmark method within an FSI investigation and reported a higher stability for their method [38]. There are various finite element formulations based on geometry, including point, line, surface and solid elements. Even though solid elements offer the opportunity to

couple fluid and structure geometries in three dimensions, they may not offer the best performance when the wall thickness of the structures is considered. Thus, new formulations such as solid-shell elements have been a focus of interest for several authors.

With regard to solid-shell elements, Meraim et al. [39] developed a new formulation for the existing finite element, SHB8PS, with a three-dimensional approach that accounts for locking. The new solid-shell element features 8 nodes and displacement as the only degrees of freedom per node in addition to arbitrary number of integration points that are distributed along the thickness. By employing an in-plane one-point quadrature scheme, the element becomes computationally more cost effective. Lastly, they concluded that the enhanced element both effectively eliminated occurrences of membrane and shear locking and performed accurately when calculating bending problems without requiring multiple elements along the thickness.

Wasfy and Noor [40] investigated the dynamic response and sensitivity of large, flexible structures with multiple bodies consisting of beams, shells and solids with a new computational procedure. They selected the Cartesian coordinate system as three degrees of freedom and used slopes within elements for the new beam, shell and solid elements. For predicting the kinematics of large body motion, they used the Lagrangian formulation with the co-rotational frame approach. The governing semi-discrete finite element equations of motion were solved by a semi-explicit temporal integration where the sensitivity equations were calculated by directly differentiating the equations of motion.

In the last several years, numerous commercial software packages have been developed for structural investigations. For partitioned FSI studies in particular, know-

ing the best practices and drawbacks of these solvers is crucial for successful FSI investigations. Examples of these types of comparisons can be found in the literature. For instance, Rust and Schweizerhof [41], performed structural investigations on structures with thin walls under different loading scenarios. They compared the two commercial software packages, ANSYS and LS-DYNA, with implicit and explicit methods respectively. They reported the benefits of both tools and concluded that LS-DYNA is more beneficial when solving the quasi-static load analyses with systems that demonstrate numerous highly nonlinear effects.

## 2.4 Fluid-Structure Interaction

Generally, most problems in nature are related to more than one physical phenomenon. For instance, the interaction between fluids and solids can be seen in numerous examples in nature. Moreover, in most of these problems the two aspects that control the problem cannot be solved separately from each other. Problems like this can be defined as Multiphysics problems [42]. As a branch of multiphysics problems, FSI problems must be solved within various different industries. Some examples of these challenging problems include cardio-vascular dynamics and the design of aircraft wings, turbine blades, tall structures and buildings and offshore and underwater structures. The literature review for the fluid-structure interaction will be presented under the following main categories: the monolithic approach and the partitioned approach.

### 2.4.1 Monolithic Approach

In the monolithic approach, a single solver solves the combined equations of solid and fluid domains simultaneously. Since the fluid and solid domains are not separate, monolithic solutions generally provide better accuracy than the partitioned approach [43]. For this reason, numerous researchers have been showing great interest in FSI investigations using the monolithic approach. Some of the solution methodologies for the monolithic approach can be named as The Arbitrary Lagrangian Eulerian (ALE), Distributed Lagrangian Multiplier, Extended Finite Element Method (XFEM), Immersed Boundary Method (IBM) and Immersed Finite Element method (IFEM) [44]. Over the last few decades, researchers from different areas have contributed to these numerical methodologies for numerical FSI investigations. As one of many examples, Zhang & Gay [44] improved the Immersed Boundary (IB) method by using a new interpolation function with higher order and advanced its proficiency with boundary conditions and non-uniform and independent meshes for fluid and solid domains. This new method, Immersed Finite Element Method (IFEM), allows the investigation of detailed stress distributions for immersed deformable structures [44].

Michler et al. [45] compared the monolithic and partitioned solution schemes based on numerical stability, computational cost and accuracy. They reported significantly more accuracy with the monolithic approach compared to the partitioned approach despite the requirement of three to four times more computational cost.

## 2.4.2 Partitioned Approach

In most engineering problems, partitioned FSI methods are used out of convenience [43]. The partitioned approach, also known as the staggered approach, is divided into two sub categories as one-way and two-way partitioned approach. The difference between one-way and two-way coupling is the additional data transfer of the structural displacements to the fluid domain and the solver during a two-way coupling. Within the FSI solution, if the convergence of two individual solvers is desired at a certain level, the coupling is considered to be strong two-way coupling. In recent years, the partitioned approach has gained great popularity owing to its convenience in allowing researchers to use existing and validated solvers instead of developing a completely new all-inclusive solver for fluid and solid domains.

Relvas and Suleman [38] coupled their dynamic structural algorithm with the vortex-ring method using a staggered technique in order to investigate the aeroelastic behaviour of a nonlinear plate-type wing subjected to low speed airflow. They reported stable and accurate solutions along with the demonstration of limit cycle oscillations. Benra et al. [42] investigated the differences between one-way and two-way coupling methods for numerical FSI analysis. One of the cases they investigated includes a structure consisting of a square cylinder and a thin plate attached to a cylinder at the downstream side. The FSI between the structure and flow was investigated under different flow speeds and plate materials that produced different vortex shedding and natural frequencies. The commercial software package ANSYS CFX was used for fluid calculations whereas ANSYS Mechanical was used for the structural aspect and ANSYS MFX was used for two-way coupling. They reported a

similar frequency prediction with one-way and two-way coupling for the deflections of the plate when the vortex shedding and the natural frequency of the structure were similar. However, when the vortex shedding frequency was distinct from the natural frequency of the structure, the results of one-way and two-way couplings for displacement magnitude and the mean frequency of oscillations were significantly different. In addition, the one-way coupling method showed lower deflections than two-way coupling. They evaluated both of the methodologies and concluded that one-way coupling is more advantageous considering the smaller solution time and mesh quality consistency due to the lack of mesh deformations. On the other hand, they noted that two-way coupling is superior in accuracy and provides more realistic results and energy conservation at the fluid-solid interface.

In addition to Benra et al. [42], numerous authors support the claim that the two-way coupling approach requires significantly longer solution time than one-way coupling. Lee et al.[34] investigated the FSI on a self-oscillating cylinder using an open sourced software package, OpenFOAM, and noted an extensive 8 to 10 times longer computational time compared to rigid cylinder investigations due to the continuous data transfer between two solvers.

Phadke and Cheung [37] investigated the nonlinear responses of the wave-membrane interaction problem by solving the coupled membrane motions along with the internal and external fluids. For the calculations of the potential flows on the inside and outside, they used a two-boundary element model. Furthermore, they coupled the fluid models with the finite element model of the membrane to solve the nonlinear responses. They used an efficient approach to solve the spatial and temporal formulations with a single iteration and reported good agreement with other numerical and

experimental work in the literature.

When compared to the monolithic approach, another advantage of the partitioned approach is that it offers flexibility when selecting individual solvers, which permits configurations or improvements on a separate solver. For instance, Gordnier & Fithen [46] developed a new three-dimensional aeroplastic solver by improving an existing structural solver. By implicitly coupling the new nonlinear finite element structural model with the finite difference method Navier-Stokes code, they advanced the capabilities of the solver so that it could handle isotropic and orthotropic materials.

### **Literature Summary**

In summary for the issue of finite length cylinders under steady flow loads, it appears that many authors have reported an upstream shifted separation point and lower hydrodynamic forces and vortex shedding frequency for finite length cylinders when compared to infinite cylinders. Although there is rapidly growing literature on the experimental and numerical investigation of hydrodynamics around cylinders, relatively little research has been carried out on the fluid-structure interaction of flexible and low aspect ratio finite cylinders. Considering the exposure of cylinders to flow-induced forces in extreme offshore environments, the fluid-interaction investigation of these structures is important for their design. The hydrodynamic forces that form around the cylinder due to the shape dependency causes deformations on the structures that conversely affect the hydrodynamic forces and create a cyclic relation between the fluid and structure. This relation and its effect on the structural responses and endurance can only be solved with the aid of an FSI investigation.

Considering this, the main objective of the presented work was to develop a nu-

merical model and method that simulates the deformations and dynamic reactions of a scale model of a deeply submerged cylindrical flexible offshore structure mounted on a supporting measurement rig, which will be used for future experimental studies. For this purpose, a two-way coupled partitioned FSI approach is proposed by coupling the FLUENT and Transient Structural Analysis modules in the ANSYS Workbench environment. Based on the current literature this method offers a practical compromise between solution accuracy and computational cost.

To sum up, the method developed within this thesis allows investigation of the realistic behaviour of the flexible cylindrical structure and testing of the endurance of the designed experimental rig, which can provide insight for other engineering applications and offer a guideline for further research.

# Chapter 3

## Methodology

This study formed part of a larger effort to develop improved numerical and experimental methods of estimating the forces on fully submerged cylinders in transverse flows. The work of this study was to numerically model the response of a simple cylinder mounted on an experimental towing apparatus (the Experimental Rig). The numerical model was developed to simulate the interplay between fluid and structural forces and responses. The numerical model will be used to help design the experimental apparatus.

### 3.1 Experimental Rig Design

In order to develop the numerical model, some preliminary design work on the experimental apparatus was carried out. While choosing the dimensions and materials of the experimental rig and the test cylinder, the dimensions of the Ocean Engineering Research Center (OERC) tow tank, the availability of materials from providers and the resources of the Engineering Tech Services were all taken into account. The

dimensions of the cylinder were adapted from a proposed sub sea structure. Experimentally, the rig will be capable of housing a range of cylinder sizes. Similarly, the selected Reynolds is also within the range of the tests planned with the experimental model.

The study was focused on a flexible cylinder mounted on an experimental rig. Thus, it is crucial to have a reliable system for measuring the flow forces around the cylinder with minimum vibrations in order to avoid unintentional instabilities on the test subject. Given that, the structural resistance of the system opposing to the fluid forces is essential as well. The flow around the cylinder should be isolated from reflecting flows and any kinds of disturbances. For this purpose, an experimental rig was designed for towing the test subject, a circular cylinder with 0.1524 m diameter and 0.60 m length, in different depths and speeds. The cylinder was designed to be attached to a plate that is 0.243 m long and 0.9144 m wide in order to simulate the ocean floor in different operating conditions. The plate was designed to be attached to the OERC tow tank carriage with a main support consisting of a 0.1016 m diameter pipe and a fin that was used in order to delay vortex formations around the main support.

Towing a submerged large plate without being exposed to severe vibrations under the prescribed speeds ( $3m/s - 4m/s$ ) is a challenge resulting in the requirement of a sturdy supporting system. Considering this, based on the preliminary numerical simulations, two cylindrical front supports were designed in order to introduce more stiffness to the system. Furthermore, they are placed 0.5 m away from the cylinder in downstream direction in order to provide more stability without disturbing the flow around the cylinder. Initial 2D fluid flow simulations show that the flow around these

supports are not affecting the test cylinder. Taking these challenges into account, the design demonstrated in Figures 3.1,3.2,3.3 and 3.4 was developed after several optimization trials.

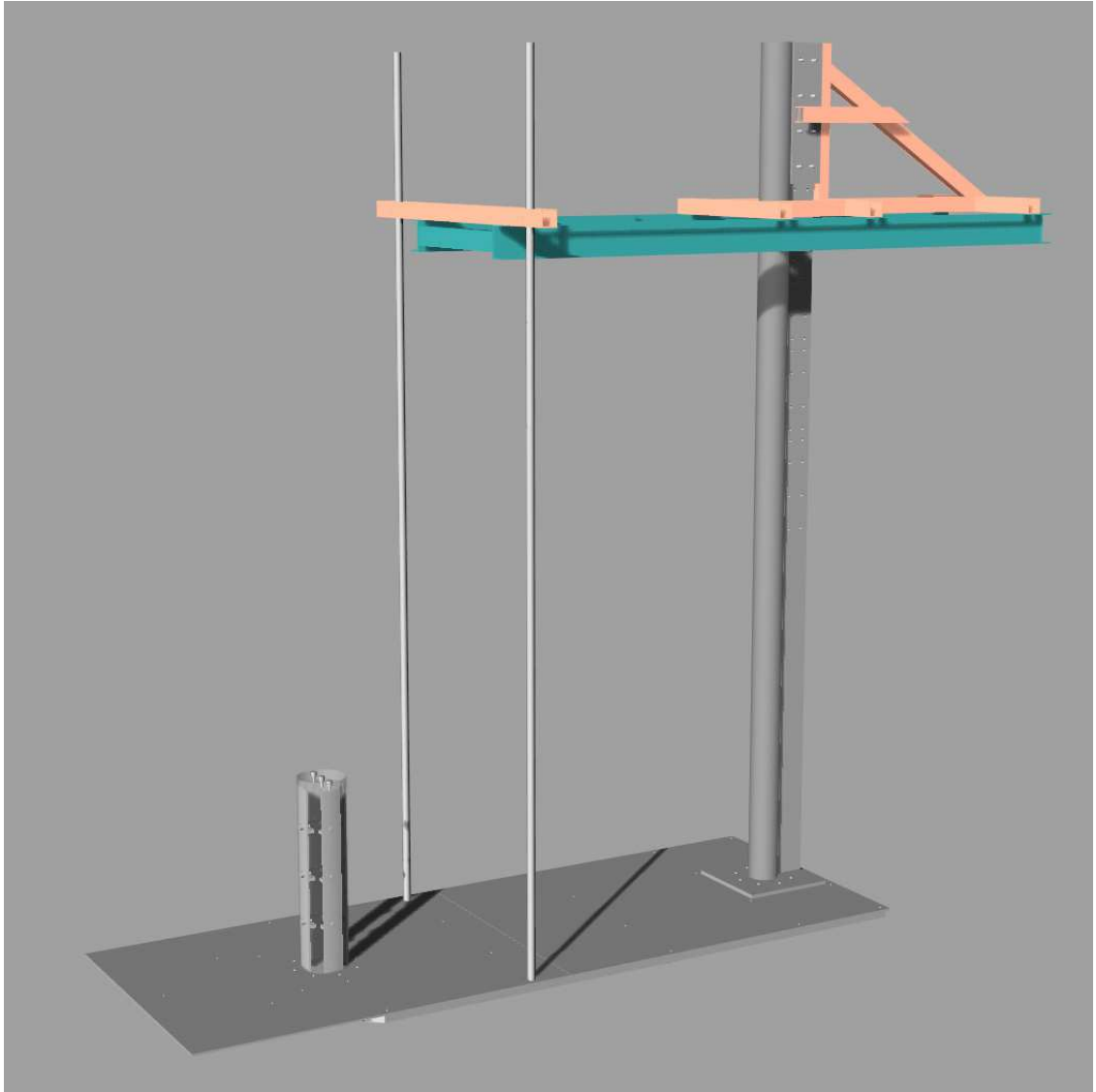


Figure 3.1: Experimental rig perspective view

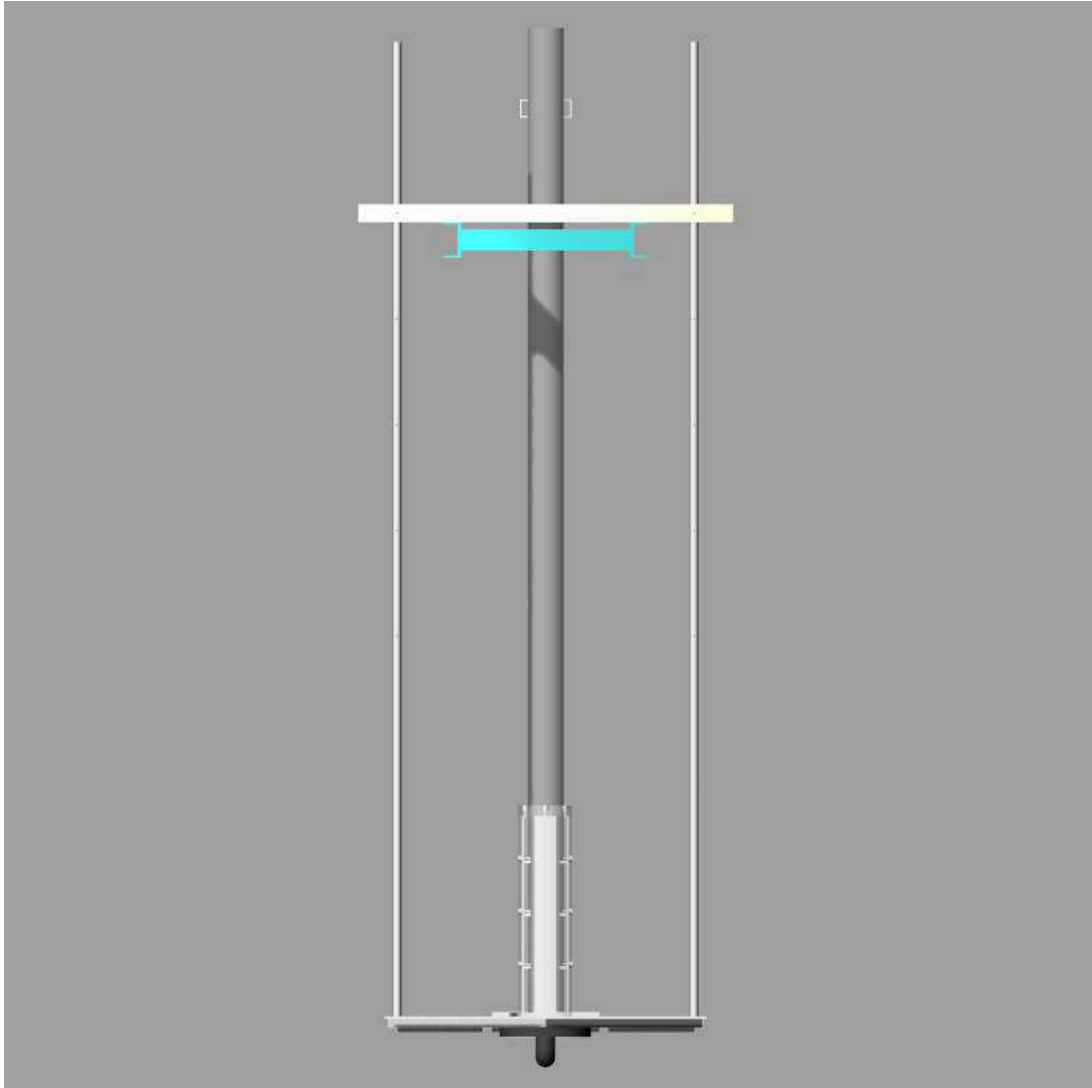


Figure 3.2: Experimental rig front view

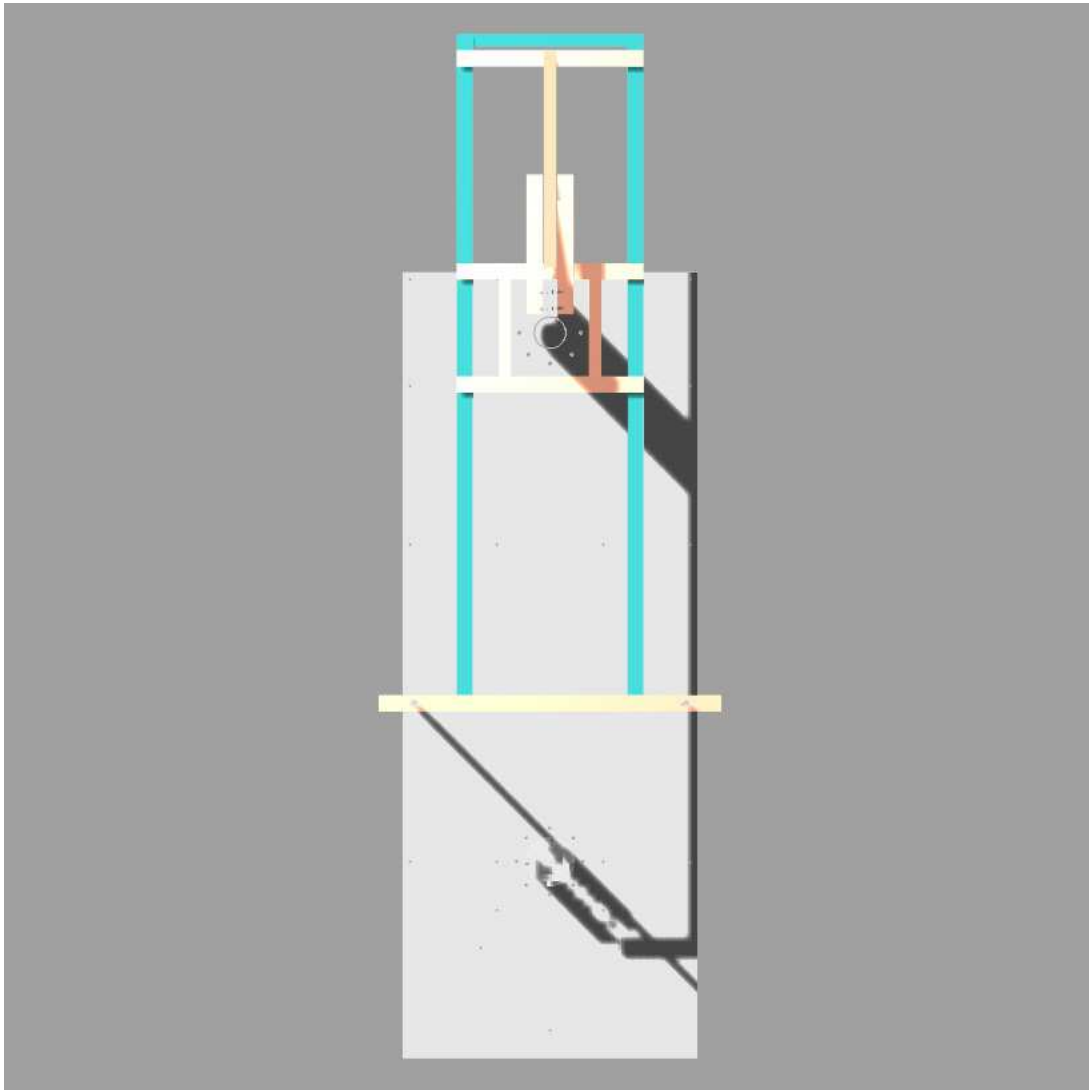


Figure 3.3: Experimental rig top view

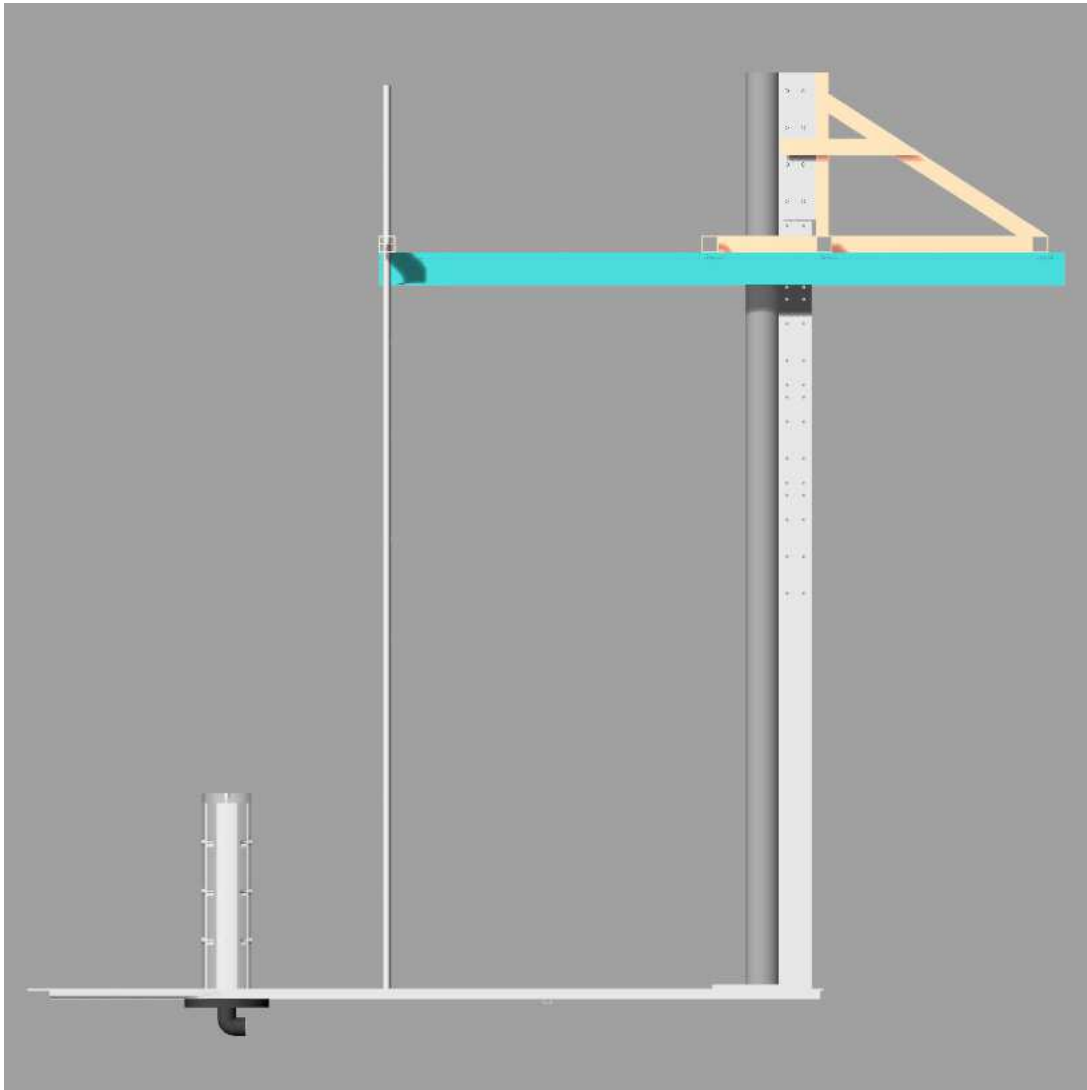


Figure 3.4: Experimental rig side view

The plate was strengthened with a frame stiffener system from the bottom of the plate as shown in the Figure 3.5.

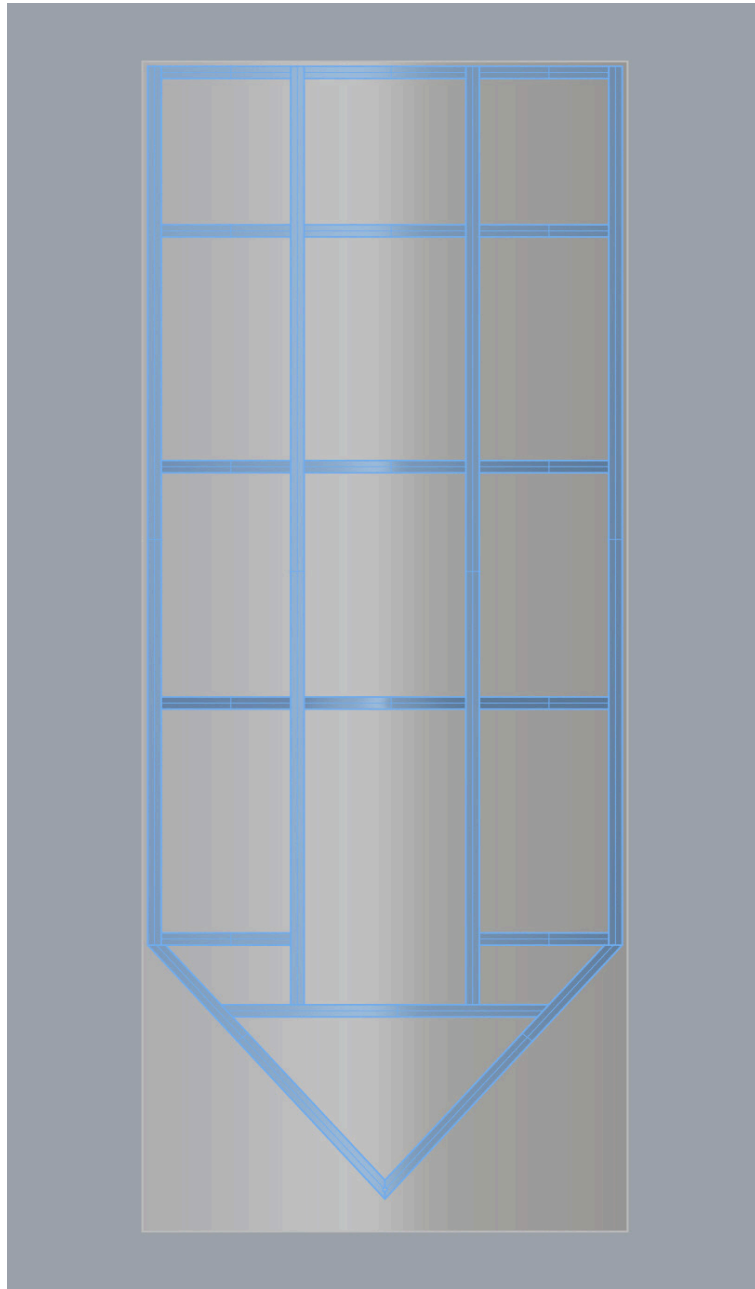


Figure 3.5: Stiffener frame underneath the plate

The experimental rig in a towing tank setup is shown in Figure 3.6.

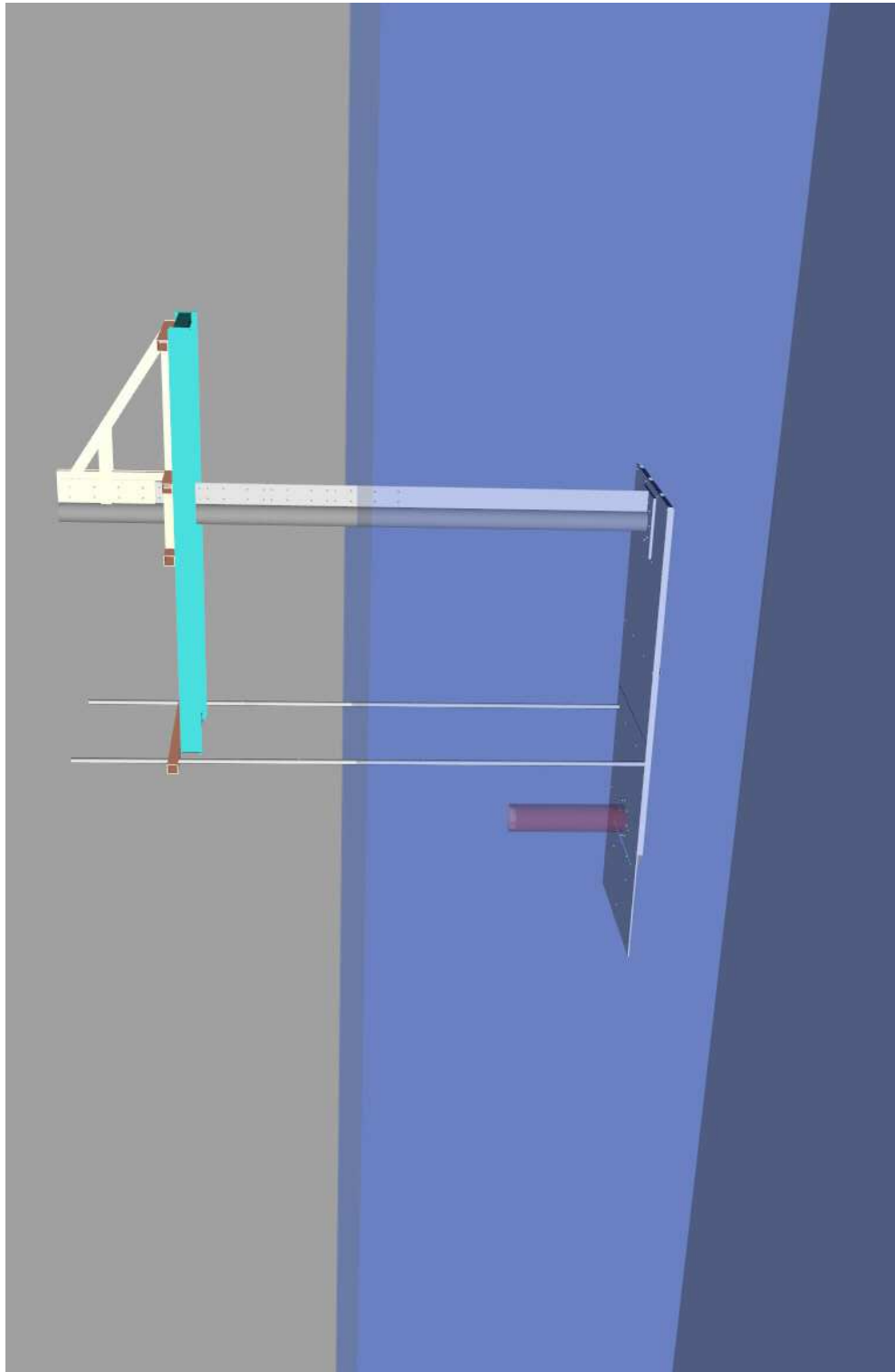


Figure 3.6: Experimental rig in towing tank

The fluid-structure interaction problem of the flexible submerged cylinder on an experimental rig was investigated numerically. With the aid of the commercial software package ANSYS, an integrated coupled model was created using FLUENT and Transient Structural modules. The numerical tool was created not only for the investigation of FSI on the cylinder but also on the test rig. This was intended to provide insight about the experimental rig's endurance for future experimental studies.

### **Numerical Models**

The main goal in computational numerical simulations is to reach the solution with the desired level of accuracy and minimized computational cost. While developing the numerical models within this research, an empirical approach was employed based on the assistance of ANSYS technical support and prior literature research. Considering the computational costs and the feasibility of the research, both the structural and hydrodynamics models were simplified as explained in the following sections. In order to develop a numerical tool using ANSYS Multiphysics for investigating the FSI of the cylinder and the experimental rig, both structural and fluid domain geometries were created together using ANSYS DesignModeler. The hydrodynamics and the structural model geometries were created as a whole in order to provide complete enclosure and prevent low quality data mapping that may happen during the coupling. Mapping data is a procedure to map variables such as pressure and deformations between the meshes of fluid and structure domains on the associated cell and faces. When creating the structural mesh, the CFD domain was suppressed whereas the opposite was done while creating the CFD mesh. Moreover, these geometries were meshed using the ANSYS Meshing within ANSYS Workbench environment. These

meshes carry different specifications such as element type, cell size and resolution due to distinctive requirements by their particular solvers. Furthermore, completed meshes were imported to the solvers separately in order to set the simulations individually. Both simulations require essential settings such as selection of the solver type, material selection or modification, setting the boundary conditions, numerical scheme selection and solution settings.

After completion of the model set up, the CFD model and the structural model were obtained within ANSYS Workbench environment. The structural model contains the experimental rig and the cylinder and the CFD model includes a single phase fluid domain around the rig and the cylinder. To complete the setup these two simulations were coupled using the System Coupling module within Workbench. Moreover, data transfers were created between the participants and their preassigned FSI regions. Multiphysics simulation settings of time step size, duration of the solution and restart points were set within the System Coupling module.

## **3.2 Assumptions and Simplifications**

In order to reach the project goals within a reasonable time frame, several simplifications and assumptions were made to decrease computational expenses.

- Two-way coupled analyses were carried out on the flexible cylinder only, whereas the response of the experimental rig, was investigated with one-way coupling for all of the case studies.
- Even though it would not be possible to see flexible structural behaviour from

a steel cylinder under the investigated conditions, the structural steel material model was modified by decreasing its Young's modulus for the purpose of creating a flexible material.

- Front supports that were designed to provide more sturdiness to the rig's plate were numerically introduced to the structural model as boundary conditions.
- A stiffener frame which was placed underneath the plate was introduced to the system numerically by modifying the plate's material properties.
- In the design process of the experimental rig, Styrofoam blocks were determined to be attached to the system in order to equalize the buoyancy forces and the weight of the system, hence gravitational effects along with damping were not included in the numerical models.
- For the wall surfaces of the experimental rig along with the cylinder, smooth and no slip wall boundary conditions were used in the CFD model.

### **3.3 Numerical Structural Model**

A static structural analysis of a system is capable of showing if the system will withstand the steady-state loading conditions. However, this may not be sufficient especially when the loading conditions alternate with time. In this case a dynamic analysis is used to determine the structural responses of a system considering the time dependent loading conditions. On the other hand, a modal analysis determines a structure's vibration characteristics. In order to understand the structural responses of the experimental rig under operation loading conditions and investigate its natural

frequency, a modal and static structural analysis model was created initially. After reaching a mesh independent solution on the static case, the model was upgraded to a dynamic structural analysis model. The following equation is solved by a transient dynamic analysis [47];

$$(M) \{\ddot{u}\} + (C) \{\dot{u}\} + (K) \{u\} = \{F(t)\} \quad (3.1)$$

In this equation (M) represents the mass matrix where (C) represents the damping matrix. Furthermore, (K) indicates the stiffness matrix and  $\{\ddot{u}\}$  indicates the nodal acceleration vector. Finally,  $\{\dot{u}\}$  illustrates the nodal velocity vector where  $\{u\}$  nodal displacement vector.

### 3.3.1 Geometry

A finite element model was created in order to investigate the structural responses of the experimental rig and the test cylinder. Transient Structural module of ANSYS Mechanical was used for the purpose. Multiple bodies were created for each individual section of the experimental rig using ANSYS DesignModeler. In order to avoid contact problems the parts composing the geometry were grouped and converted to a multi-body part.

For the purpose of simplifying the structural module, front supports were introduced as a fixed support condition onto the region of their attachment point with the plate. Thus, they were not included in the model geometrically. Figure 3.7 shows the experimental rig's structural geometry including six bodies.

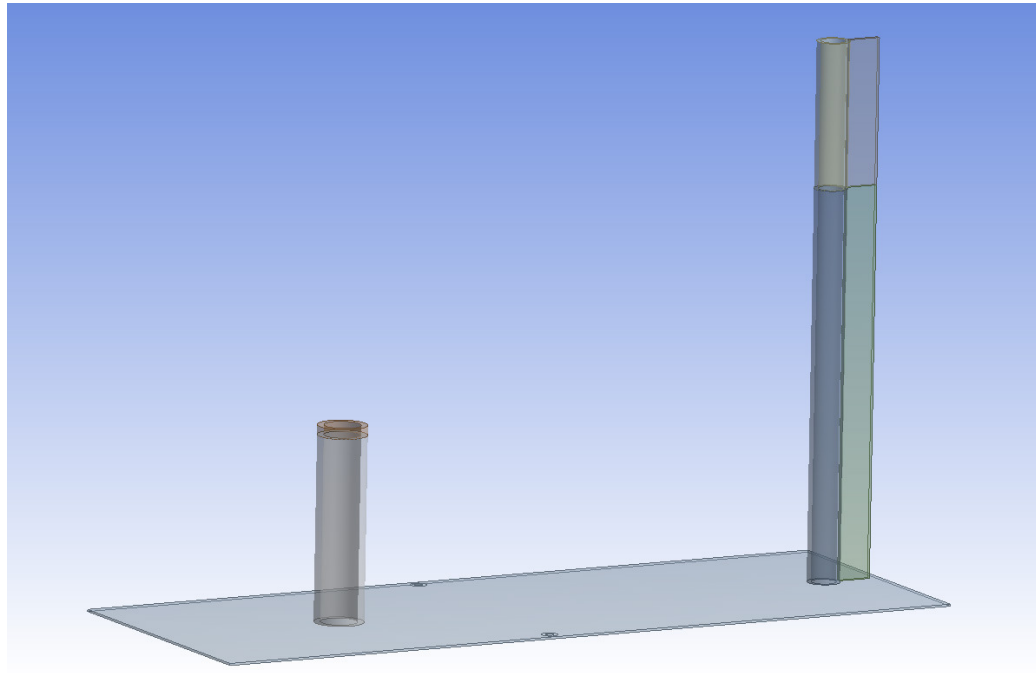


Figure 3.7: Structural geometry

### 3.3.2 Computational FE Mesh

Following the geometry creation, the generation of a mesh is required. Due to coupling requirements between the structural and fluid dynamics models and considering the fact that the parts forming the experimental rig are thin plates, the finite element model was created using solid/shell elements. For this purpose, SOLSH190 type elements were used in ANSYS Mechanical. These elements allow geometry and mesh coupling for FSI problems and far less expensive than the solid elements. Furthermore, SOLSH190 features eight node connectivity and 3 DOF for each node. They support large deflections and large strain capabilities along with plasticity, hyper elasticity, creep and stress stiffening [48].

In order to obtain a constructed mesh, local mesh sizing controls applied on the

edges are shown in the Figure 3.8. The figure shows the element sizes that are used in order to create the optimal mesh for the structural model.

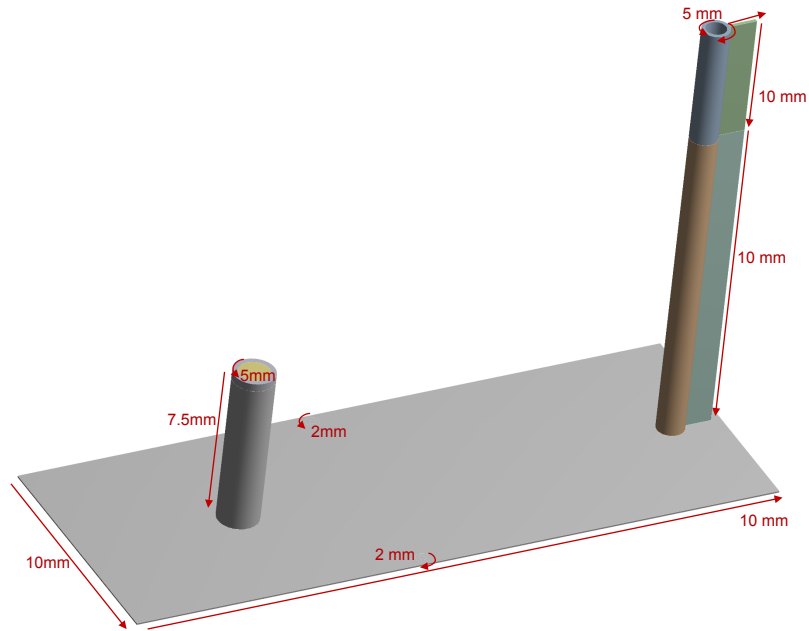


Figure 3.8: Rig meshing parameters

### 3.3.2.1 Mesh Dependence Study for Structural FE Model

Considering the need for a vibration free, stable and durable experimental rig, predicting its stability and endurance was crucial. Although a structural analysis can provide significant insight about these considerations, its performance is strongly dependent on the mesh and the use of correct boundary conditions. A mesh dependence study was conducted focusing on the resultant displacement and a very fine

mesh was chosen in order to achieve maximum accuracy. Moreover, in order to set a static structural simulation, the loads acting on the cylinder and experimental rig were obtained from an individual CFD simulation. These hydrodynamic forces along with their directions acting on the FSI geometries are shown in Table 3.1.

Table 3.1: Hydrodynamic Forces on the Rig

| Geometry | Force Direction | Force Magnitude (N) |
|----------|-----------------|---------------------|
| Cylinder | X               | 154.13              |
| Cylinder | Y               | 3.03                |
| Cylinder | Z               | 83.94               |
| Plate    | X               | 76.87               |
| Plate    | Y               | 0.3                 |
| Plate    | Z               | -69.32              |
| Support  | X               | 241.15              |
| Support  | Y               | 22.99               |
| Support  | Z               | -0.43               |

The fixed support boundary conditions were applied to the system on the attachment surfaces of the frontal supports and the carriage. The gravitational acceleration of the earth was not introduced to the system due to the design principal of keeping the weight of the rig and buoyancy forces equal in order to avoid vibrations. After completion of the static structural analysis model setup, different element sizes shown

in Table 3.2 were chosen in order to create different meshes with various mesh concentrations on the rig. Different mesh element sizes, ranging from 10 mm to 1.5 mm, were used to create various meshes as shown in Table 3.2.

Table 3.2: Element size and node count

| Element Size (mm) | Node Count |
|-------------------|------------|
| 10                | 70,468     |
| 5                 | 250,042    |
| 2.5               | 1,055,679  |
| 2                 | 2,021,665  |
| 1.5               | 3,944,884  |

Table 3.3: von-Mises Stresses

| Mesh | Number of Nodes | von-Mises Stress (MPa) |
|------|-----------------|------------------------|
| 1    | 70,468          | 36.065                 |
| 2    | 250,042         | 45.705                 |
| 3    | 1,055,679       | 51.196                 |
| 4    | 2,021,665       | 55.379                 |
| 5    | 3,944,884       | 55.215                 |

Table 3.4: Deformations

| Mesh | Number of Nodes | Deformations (mm) |
|------|-----------------|-------------------|
| 1    | 70,468          | 0.774             |
| 2    | 250,042         | 0.774             |
| 3    | 1,055,679       | 0.775             |
| 4    | 2,021,665       | 0.775             |
| 5    | 3,944,884       | 0.775             |

Table 3.5: Changes in von-Mises Stresses and deformations for different meshes

| Mesh | Number of Nodes | Change in von-Mises Stresses | Change in Deformations |
|------|-----------------|------------------------------|------------------------|
| 1    | 70,468          | -                            | -                      |
| 2    | 250,042         | 26.7%                        | 0.056%                 |
| 3    | 1,055,679       | 12%                          | 0.076%                 |
| 4    | 2,021,665       | 8.2%                         | 0.052%                 |
| 5    | 3,944,884       | -0.3 %                       | 0.03%                  |

It can be clearly seen from Table 3.3, 3.4 and 3.5 that the element size of 2 mm was the most accurate and efficient size for the model. The model created with this element size contained around two million nodes which was an excessive number of

equations to solve within an FSI simulation. Considering the continuous calculation of the structural model during the coupling iterations, this amount of equations would extend the computational time beyond feasible limits. Thus, an optimized model was needed. In order to achieve an optimized model, the high stress areas on the structure were meshed with more concentrated mesh and the mesh concentration around the low stress areas was coarsened. This optimized model of the experimental rig including the plate, cylinder, cylinder cap and support system contains 71052 elements with 123860 nodes. The average aspect ratio of the mesh was 2.26 and the average skewness was 0.061. This mesh can be seen in Figure 3.9.

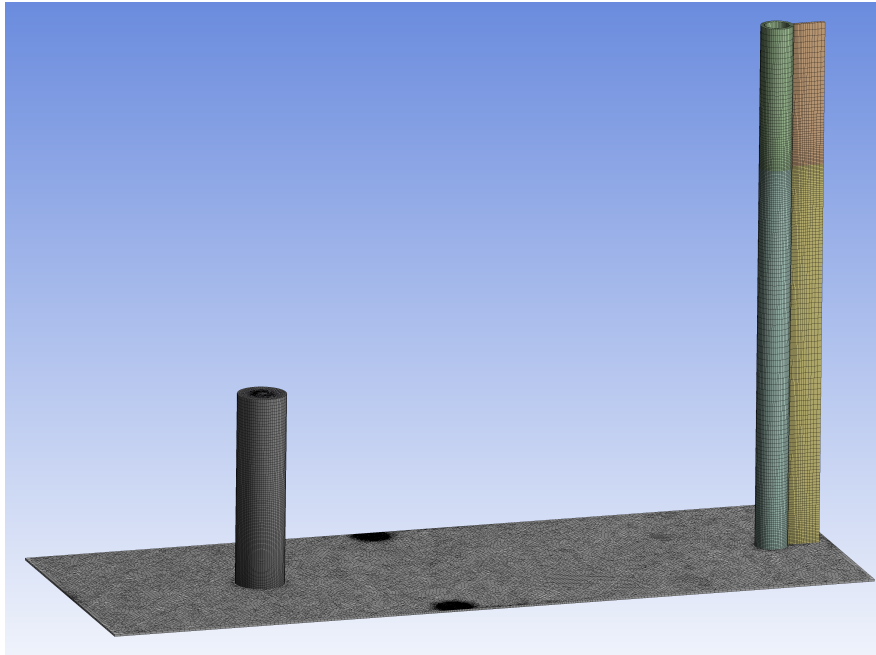


Figure 3.9: Structural mesh

The changes in the Von-misses stresses regarding the different mesh concentrations is shown in Table 3.5. Moreover, the plot showing the prediction of the von-Mises

stresses based on the increased node count can be seen in Figure 3.10. The point shown in red represents the optimized structural FE mesh that was further used in the FSI simulations.

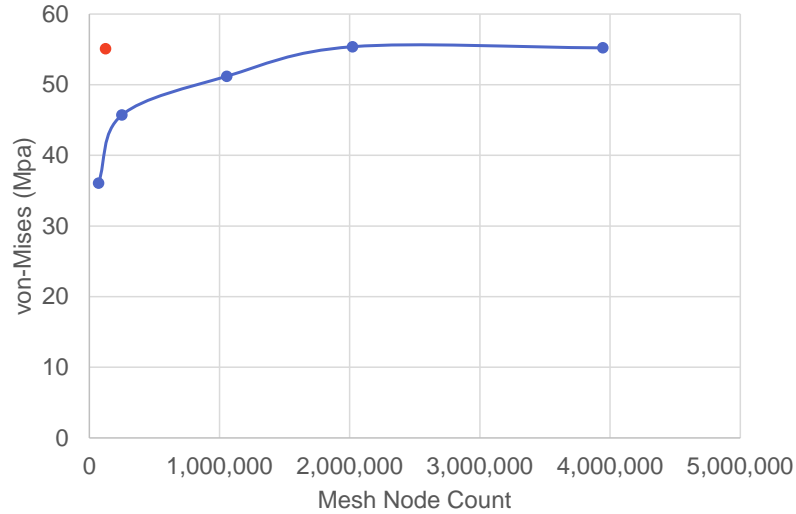


Figure 3.10: Structural mesh convergence study

### 3.3.3 Simulation Setup

One of the challenges of a numerical investigation of the FSI problems is the demand for computational resources and the solution time. In order to obtain numerical results in the reasonable time, solver performances of both the Mechanical and Fluent modules in ANSYS were critical. Even though the CFD portion of the FSI problem requires more computational resources, due to the size of the structural solution and the necessity for repetition at the end of each coupling iteration, the performance of the Mechanical solver was also crucial. A numerical benchmark test for comparison

of solver type vs. calculation time was conducted to choose the most robust solver for this particular problem. Even though a direct solver would be more robust for the analysis of the static structural responses of the experimental rig, due to the extensive output file sizes and non-linearities in the system, an iterative solver, Preconditioned Conjugate Gradient (PCG), was used for its efficiency in memory and storage usage. It was also evident that for this specific solver, the use of eight parallel processors gave the most speed-up in the solution time.

### **3.3.3.1 Materials**

Considering the difficulties of FEA on hyper elastic materials due to the large deformations and their ability to withstand greater strains than conventional materials [49], the default structural steel model from ANSYS Material Database [50] was used as material for the support system and rigid cylinder. For the flexible cylinder, structural steel model was modified by decreasing its Young's modulus to provide a more stable flexible behaviour. On the other hand, structural steel model was modified by increasing its Young's modulus in order to introduce the sturdiness gained by the stiffener frame underneath the plate. Initial calculations and simulations showed that this frame stiffens the plate resulting in 1/10 of the initial deformations. Thus, the Young's modulus of the structural steel material model was increased from 200 GPa to 2000 GPa.

### **3.3.3.2 Boundary Conditions**

Following the creation of the geometry and the mesh, boundary conditions had to be applied to the structural analysis model in order to constrain the system. As shown

in Figure 3.11 with letters A and B, four fixed support boundary conditions were introduced to the structural model on the points of attachments between the plate and the frontal cylindrical supports and the 45cm portion of the wake plate which was attached to the main cylindrical support.

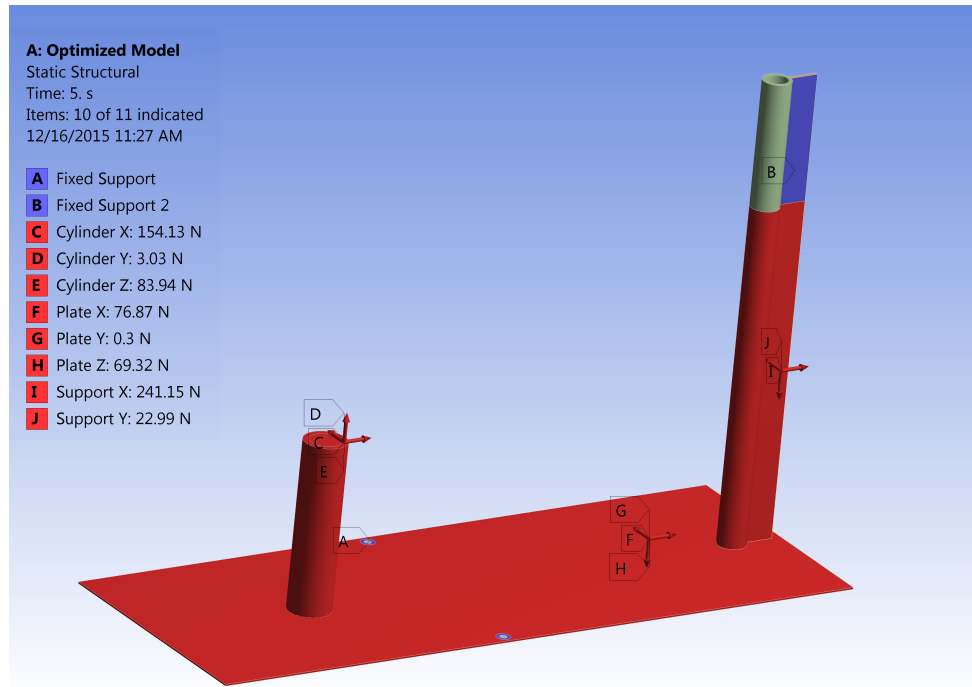


Figure 3.11: Rig structural model

Figure 3.11 shows the FE geometry and the supports along with the marked FSI data transfer regions in red. Forces that are shown with the letters C, D, E, F, G, H, I and J were not used as force boundary conditions in the FSI model. These areas were set as fluid-solid interface and the forces were calculated by the CFD portion of the simulation.

ANSYS Mechanical employs the finite element analysis approach for calculating the

stresses and deformations. Some of the governing stress equations that mechanical solvers address can be shown as follows [51]:

$$\{\sigma\} = [D]\{\varepsilon\} \quad (3.2)$$

in the equation, [D] represents elastic stiffness matrix and  $[\sigma]$  represents stress tensor which can also be written as:

$$\{\sigma\} = [\sigma_{xx}\sigma_{xy}\sigma_{xz}\sigma_{yx}\sigma_{yy}\sigma_{yz}\sigma_{zx}\sigma_{zy}\sigma_{zz}] \quad (3.3)$$

where  $\sigma_{xy} = \sigma_{yx}$ ,  $\sigma_{xz} = \sigma_{zx}$  and  $\sigma_{yz} = \sigma_{zy}$ .

The total strain tensor  $\{\varepsilon\}$  can also be written as:

$$\{\varepsilon\} = \text{total strain tensor} = [\varepsilon_{xx}\varepsilon_{xy}\varepsilon_{xz}\varepsilon_{yx}\varepsilon_{yy}\varepsilon_{yz}\varepsilon_{zx}\varepsilon_{zy}\varepsilon_{zz}] \quad (3.4)$$

where  $\varepsilon_{xy} = \varepsilon_{yx}$ ,  $\varepsilon_{xz} = \varepsilon_{zx}$  and  $\varepsilon_{yz} = \varepsilon_{zy}$ .

$\varepsilon_{xy}$ ,  $\varepsilon_{yz}$ ,  $\varepsilon_{xz}$  represent the shear strains. Shear strains can be expressed as follows by the aid of Shear modulus and stresses:

$$\gamma_{xy} = \frac{\sigma_{xy}}{G_{xy}} \quad (3.5)$$

$$\gamma_{yz} = \frac{\sigma_{yz}}{G_{yz}} \quad (3.6)$$

$$\gamma_{xz} = \frac{\sigma_{xz}}{G_{xz}} \quad (3.7)$$

whereas shear modulus can be written as follows for isotropic and homogeneous materials:

$$G = \frac{E}{2(1 + \nu)} \quad (3.8)$$

Finally von-Mises Stresses are calculated with the following formula[51]:

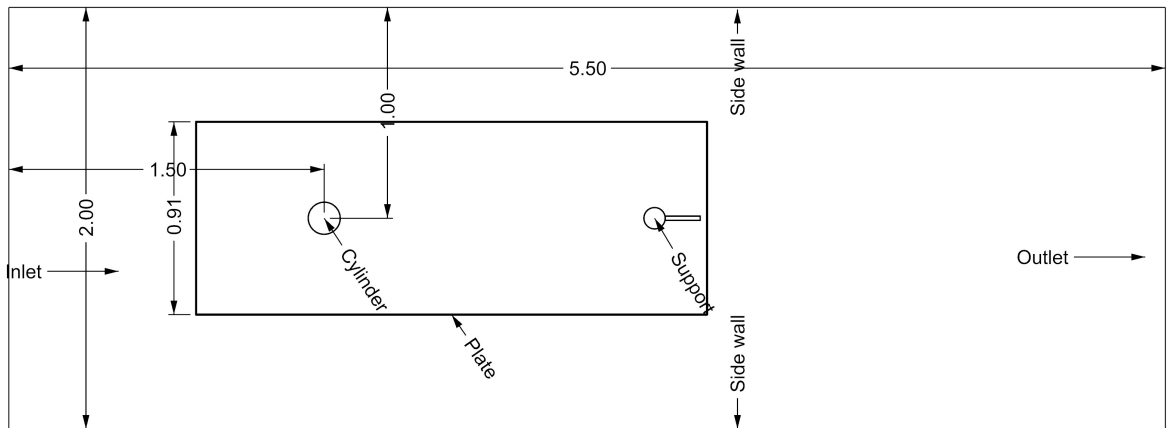
$$\sigma_e = \sqrt{\left[ \frac{(\sigma_{xx} - \sigma_{yy})^2 + (\sigma_{yy} - \sigma_{zz})^2 + (\sigma_{zz} - \sigma_{xx})^2 + 6(\sigma_{xy}^2 + \sigma_{yz}^2 + \sigma_{xz}^2)}{2} \right]} \quad (3.9)$$

## 3.4 Numerical Fluid Flow Model

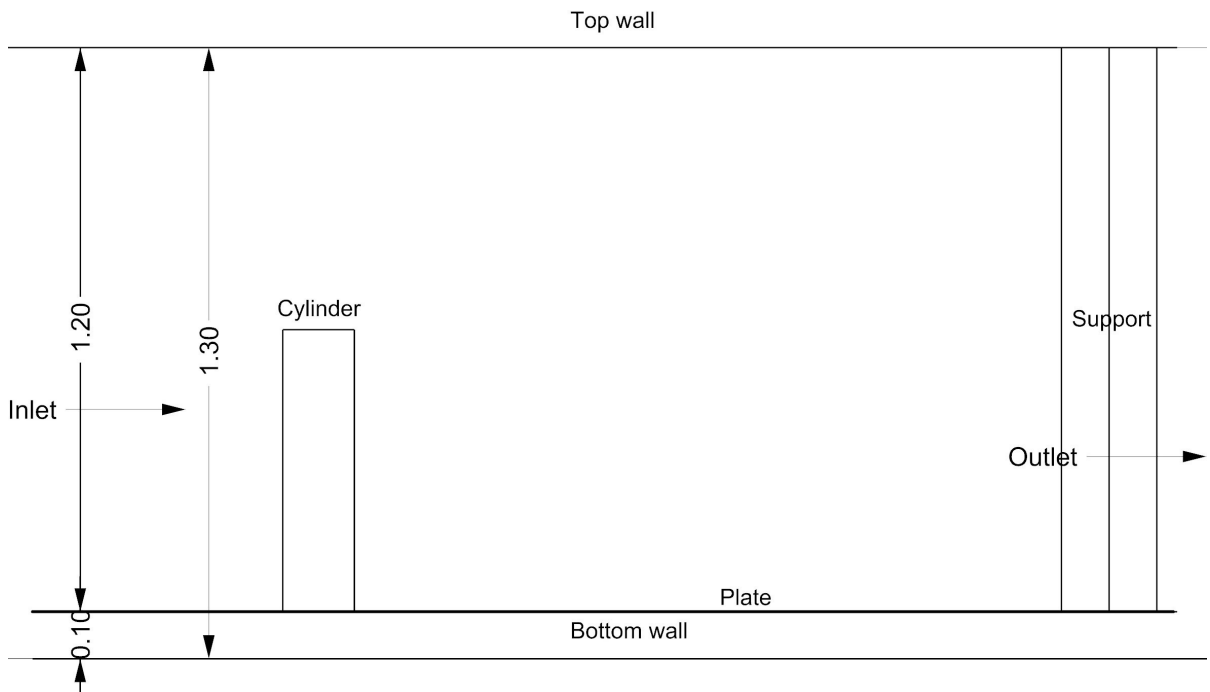
### 3.4.1 Geometry

ANSYS Fluent uses volume of fluid method (VOF) to simulate fluid dynamics. In order to simulate fluid flow around the cylinder and the experimental rig, a three dimensional CFD domain, or in other words, a numerical towing tank, was created. To simulate the previously determined test scenario, a single phase fluid flow model was used. The domain dimensions and the placement of the test rig can be seen in Figure 3.12a. The CFD domain is 5.5 meters long and 2 meters wide. The test subject, the cylinder, is placed at the origin of the domain. The inlet distance from the center of the cylinder is 1.5 meters upstream and the outlet distance is 4 meters downstream. The experimental rig along with the test cylinder is centered between the side walls giving 1 meters distance from the cylinder center to the walls.

Figure 3.12 b shows the vertical placement of the test apparatus and the cylinder in the CFD domain. The cylinder was submerged to 1.2 meters of depth which was twice its height. The distance from the bottom wall to the plate that was initially designed to simulate the ocean floor scenarios was determined as 0.1 meters. The domain has 1.3 meters of height in total. The geometry that is being used for the CFD model is a multi-body part which is divided into 102 bodies in order to obtain practical and successful meshing controls.



(a) CFD domain top view



(b) CFD domain side view

Figure 3.12: CFD domain view

### **3.4.2 Computational Fluid Mesh**

CFD mesh was created using ANSYS Meshing. Thirteen local mesh sizing controls, three multi zone mesh methods and 4 inflation controls were applied in order to create a constructed hexahedron mesh. Following the initial mesh creation and preliminary CFD simulation results it was seen that further refinement in the CFD mesh was required. Several refinements were made based on the mesh dependence studies each focusing on different dimensions around the cylinder. First, a mesh study on a wall to wall cylinder was conducted focusing on the element concentration in the perpendicular direction of the cylinder circumference. Nine different meshes were created and the results investigated. The most accurate and efficient mesh defined the meshing parameters for the subsequent mesh dependence study. Moreover, another mesh study was conducted on a truncated cylinder. Lastly, a general refinement which focuses on not only the cylinder but also on the experimental rig was made on the CFD mesh. As a result, the mesh consisting of 3027800 elements with an average of 0.043 skewness, 0.987 orthogonal quality and 9.371 aspect ratio was created. The aspect ratio value is bigger than desired; however, it represents the averaged aspect ratio of the whole CFD mesh which intentionally involves coarser mesh in the less significant areas. This mesh is shown in Figure 3.26.

#### **3.4.2.1 Mesh Dependence Study for Wall to Wall Cylinder**

Considering that the most of the experimental work was done with infinite cylinders, initially a wall to wall cylinder was investigated for the mesh study. Even though a circular cylinder shows basic geometrical features, the flow passing over it shows com-

plex physics. When capturing the physics of the fluid around a circular cylinder, the surrounding mesh carries a high significance. Along with an appropriate turbulence model and near wall treatment, the size and number of elements define the success of the flow solution. Considering this, a mesh dependence study was conducted around an infinite (wall to wall) cylinder by changing the element concentration in the area shown in Figure 3.13. Considering the convergence of residual values, initially a time step size of 2.5 milliseconds was chosen.

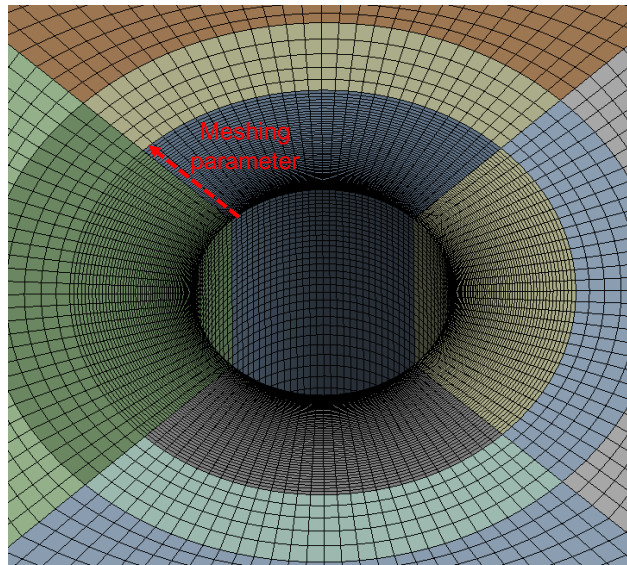


Figure 3.13: Wall to wall cylinder mesh study focus area, around the cylinder

Eight different meshes were created using incremental numbers of elements around the cylinder. The number of elements and the element size that were used to create different meshes are defined in Table 3.6. A biasing factor of 5, with a decreasing element size towards the cylinder, was used in order to provide a smoother transition

within the mesh.

Table 3.6: Mesh convergence study for wall to wall cylinder

| Mesh   | Number of Elements | Mesh Changes                     |
|--------|--------------------|----------------------------------|
| Mesh A | 1101750            | 25 elements around the cylinder  |
| Mesh B | 1326750            | 50 elements around the cylinder  |
| Mesh E | 1434750            | 62 elements around the cylinder  |
| Mesh C | 1551750            | 75 elements around the cylinder  |
| Mesh D | 1776750            | 100 elements around the cylinder |
| Mesh F | 2001750            | 125 elements around the cylinder |
| Mesh G | 2226750            | 150 elements around the cylinder |
| Mesh H | 2676750            | 200 elements around the cylinder |

The plots of the drag coefficients are shown in Figure 3.14, while the plots for lift coefficients can be found in Figure 3.15. Furthermore, the comparison of the root mean squares of the lift coefficients,  $C'_L$ , and Strouhal numbers can be seen in Figures 3.16 and 3.17 respectively.

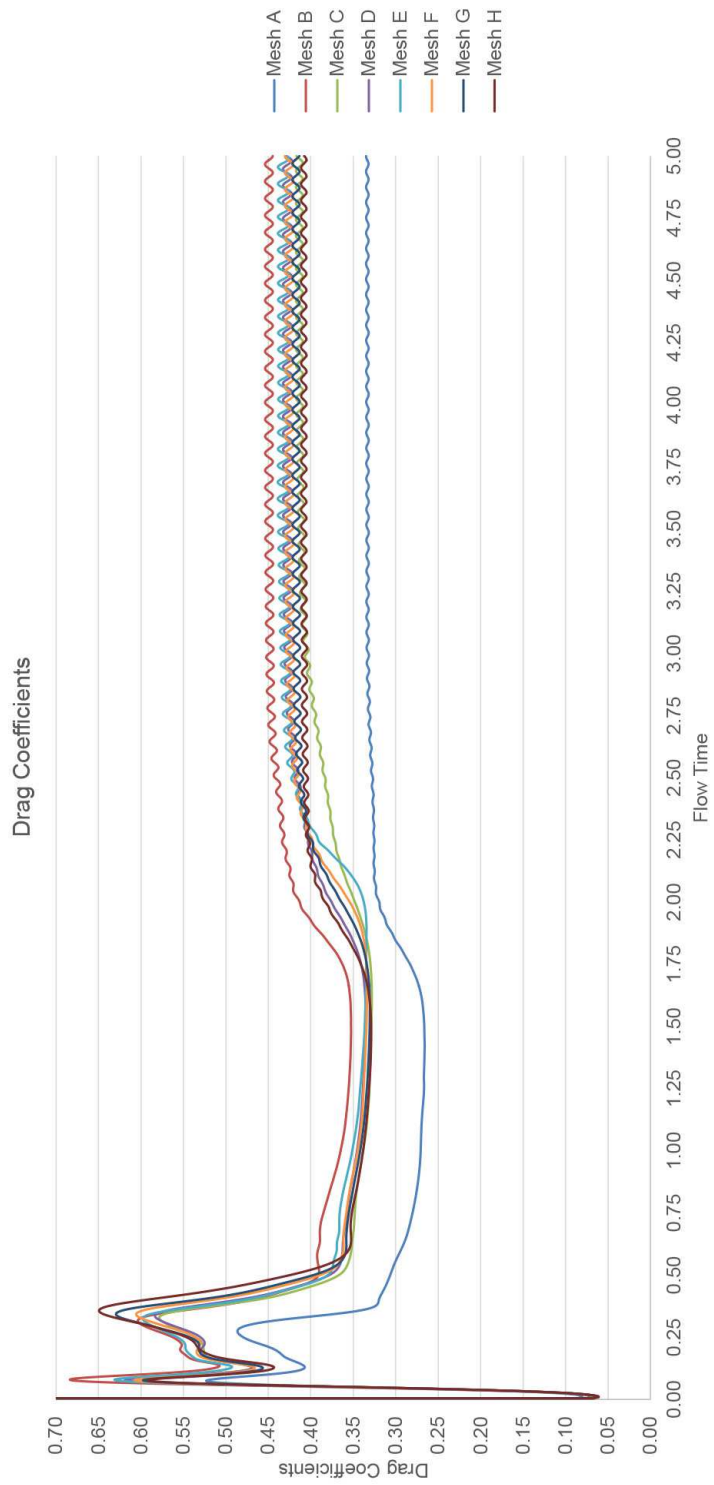


Figure 3.14: Drag coefficients over flow time for wall to wall cylinder mesh study

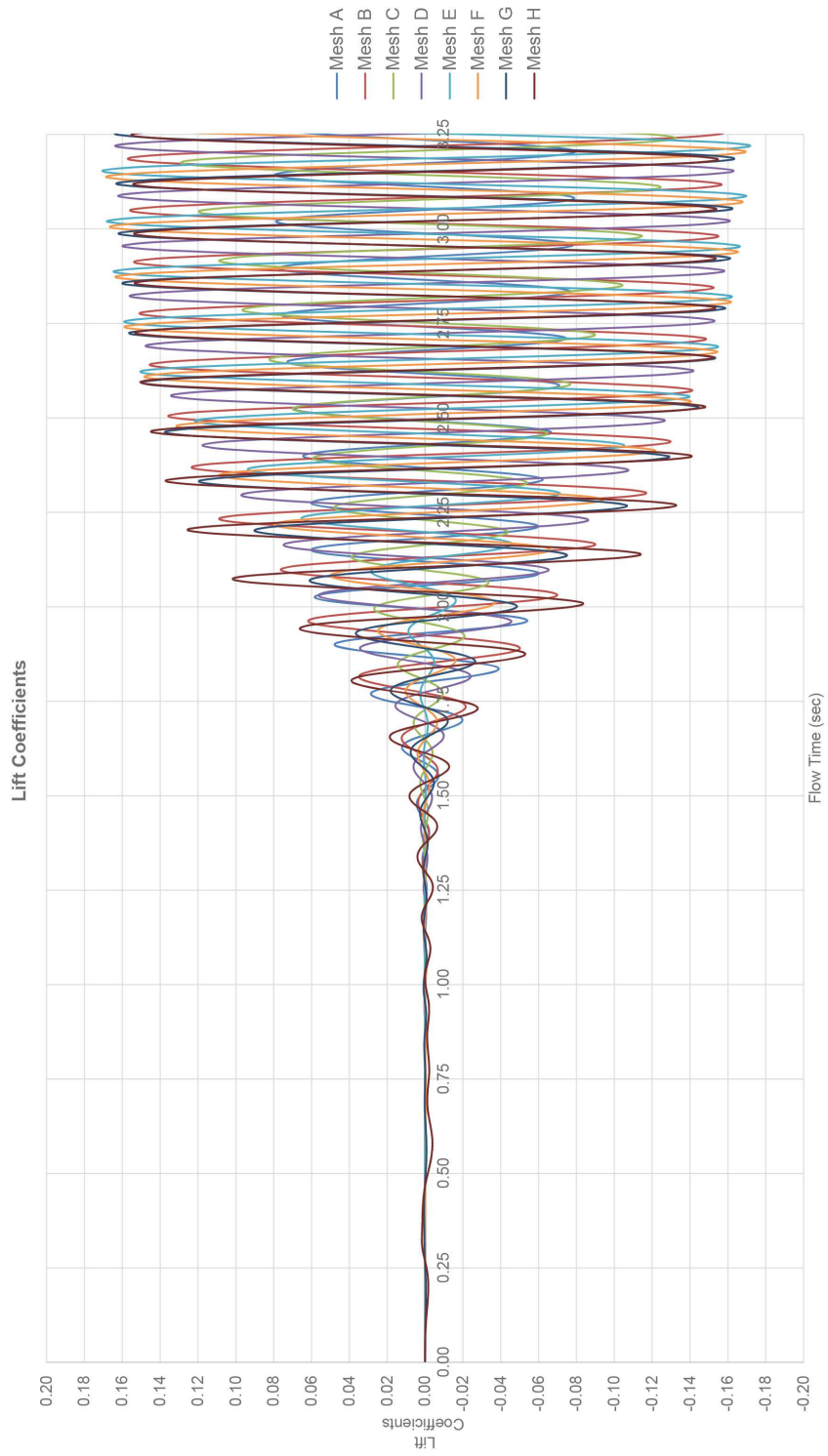


Figure 3.15: Lift coefficients over 3.25 sec of flow time for wall to wall cylinder mesh study

It can be clearly seen from Figure 3.15 that Mesh E predicts the highest oscillations.

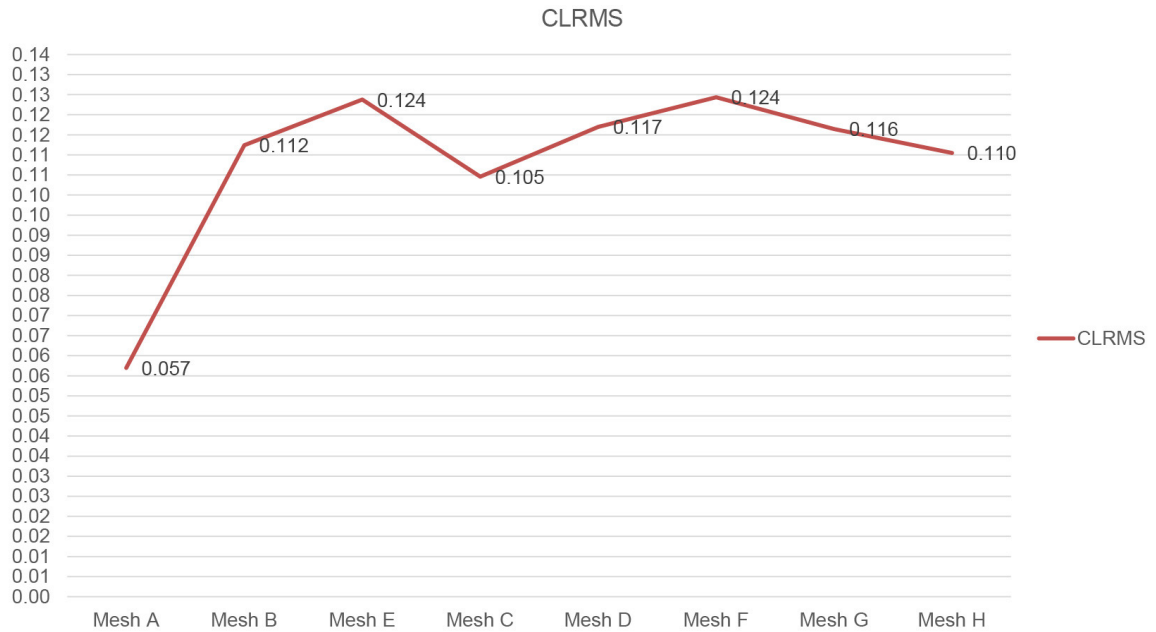


Figure 3.16:  $C_L$  RMS values for wall to wall cylinder mesh study

Figure 3.16 demonstrates the  $C_L$  RMS values for different meshes. It can be seen that highest values are calculated by Mesh E and Mesh F.

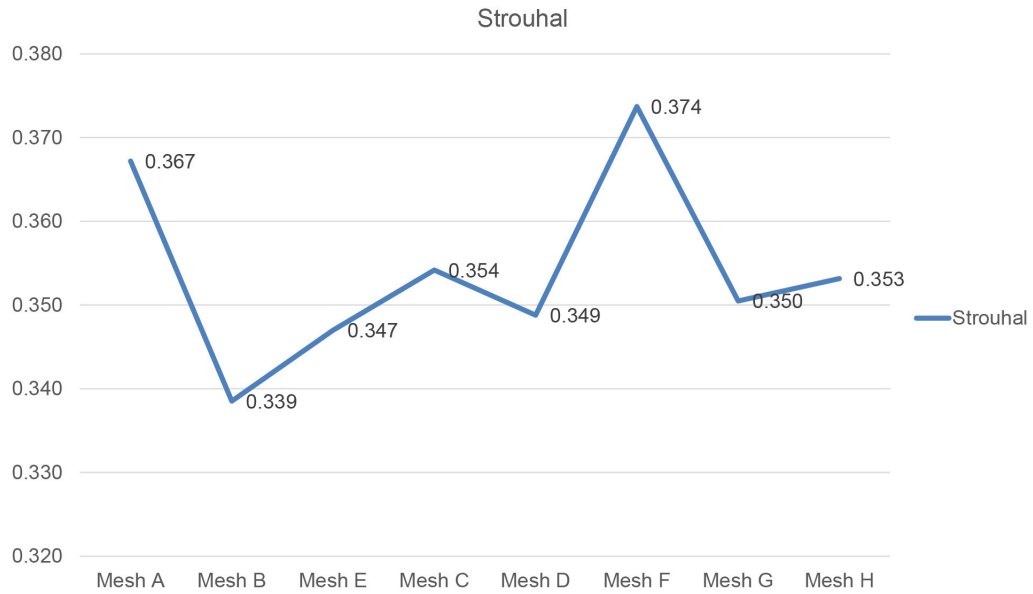


Figure 3.17: Strouhal number for wall to wall cylinder mesh study

Figure 3.17 indicates the highest shtrouhal number as 0.374 which was predicted by Mesh F. Mesh E predicts this parameter as 0.347.

The results of drag coefficient  $C_D$ , RMS of lift coefficient  $C'_L$ , Strouhal and  $Y+$  are shown in Table 3.7.

Table 3.7: Mesh convergence study for wall to wall cylinder

| Mesh   | Number of Elements | $C_D$ | $C'_L$ | Strouhal | Distance (mm) | Y+ |
|--------|--------------------|-------|--------|----------|---------------|----|
| Mesh A | 1101750            | 0.333 | 0.057  | 0.367    | 1.17          | 88 |
| Mesh B | 1326750            | 0.449 | 0.112  | 0.339    | 0.59          | 45 |
| Mesh E | 1434750            | 0.432 | 0.124  | 0.347    | 0.48          | 36 |
| Mesh C | 1551750            | 0.412 | 0.105  | 0.354    | 0.39          | 30 |
| Mesh D | 1776750            | 0.427 | 0.117  | 0.349    | 0.29          | 22 |
| Mesh F | 2001750            | 0.425 | 0.124  | 0.374    | 0.24          | 18 |
| Mesh G | 2226750            | 0.417 | 0.116  | 0.350    | 0.20          | 15 |
| Mesh H | 2676750            | 0.408 | 0.110  | 0.353    | 0.15          | 12 |

Considering the literature data ([29],[13], [7], [17], [52] cited in [6], [53], [54],[55], [56]) and the results shown in Table 3.7, Mesh E seemed to be the best choice for simulating the flow around an infinite cylinder.

### 3.4.2.2 Mesh Dependence Study for Truncated Cylinder

Following the conclusion of the mesh study for an infinite cylinder, another mesh study was conducted for a finite, truncated cylinder in order to achieve an optimized, mesh independent model for the CFD model. Considering the existence of the free end and that turbulence is a three dimensional physical phenomenon, mesh concentration and quality are significant in three dimensions. After finishing the initial mesh dependence study with the understanding of the circumferential mesh requirements

on the horizontal plane, another mesh study was conducted in order to obtain a mesh independent result regarding the requirements along the Z axis. Similarly, a time step size of 2.5 milliseconds was chosen for the mesh study.

Initially nine meshes were created based on the parameters shown in Table 3.8.

Table 3.8: Meshing parameters for truncated cylinder mesh study

| Run Matrix   | Ny=50  | Ny=100 | Ny=150 |
|--------------|--------|--------|--------|
| Nz=75,Bz=10  | Mesh 1 | Mesh 2 | Mesh 3 |
| Nz=150,Bz=15 | Mesh 4 | Mesh 5 | Mesh 6 |
| Nz=200,Bz=20 | Mesh 7 | Mesh 8 | Mesh 9 |

In table above, the index Nz represents the number of elements along the height of the cylinder (0.6 meters), where Ny represents the number of elements in the normal direction to circumference of the cylinder. In addition, Bz shows the number of elements within 0.1 m above the cylinder in the Z direction. A biasing factor of 10 was used with this element sizing. The mesh within this area was taken into account carefully considering the mesh refinements for capturing the flow separations. After finishing the initial runs, three more meshes were added to the study in order to investigate the effect of circumferential element number. While creating these meshes, the number of elements above the cylinder, within the separation area, were kept as 20 for all the additional meshes. The meshing parameters for the additional meshes are shown in Table 3.9.

Table 3.9: Meshing parameters for additional meshes

| Run Matrix        | $N_y=100$ | $N_c$ |
|-------------------|-----------|-------|
| $N_z=75, B_z=20$  | Mesh 10   | 120   |
| $N_z=100, B_z=20$ | Mesh 11   | 160   |
| $N_z=125, B_z=20$ | Mesh 12   | 200   |

In Table 3.9,  $N_c$  represents the number of circumferential elements around the cylinder. Furthermore, Figure 3.18 demonstrates the meshing parameters in a vertically sliced mesh.

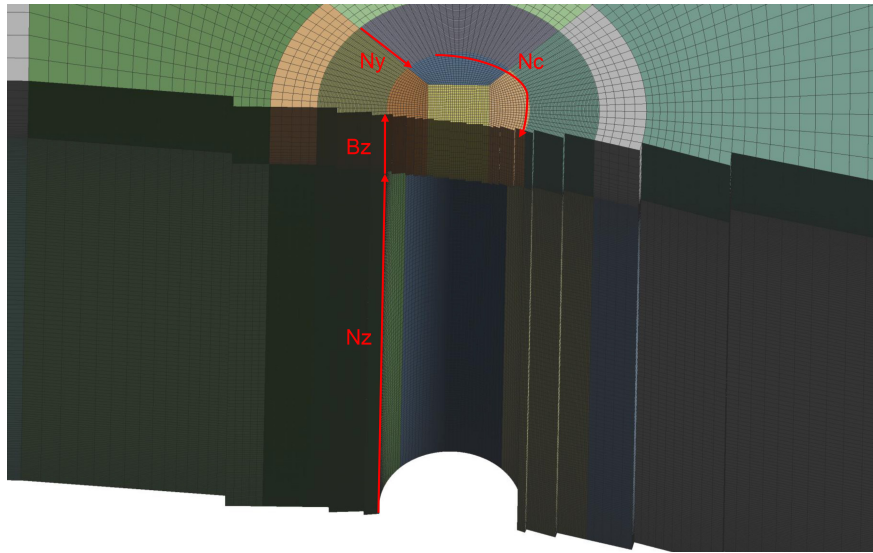


Figure 3.18: Meshing parameters for the truncated cylinder

Table 3.10 shows the number of elements, the aspect ratio of the cell surrounding

the cylinder and Y+ values on X-Y and Z axes.

Table 3.10: Meshing parameters for mesh convergence study for truncated cylinder

| Mesh Specs | Number of Elements | AR Around Cylinder | Y+ (X-Y axis) | Y+ (Z axis) |
|------------|--------------------|--------------------|---------------|-------------|
| Mesh 1     | 1652990            | 5.63               | 111           | 184         |
| Mesh 2     | 2198990            | 6.00               | 56            | 184         |
| Mesh 3     | 2744990            | 8.50               | 37            | 184         |
| Mesh 4     | 3081690            | 3.81               | 111           | 125         |
| Mesh 5     | 4107690            | 6.63               | 56            | 125         |
| Mesh 6     | 5133690            | 9.46               | 37            | 125         |
| Mesh 7     | 4068140            | 4.09               | 111           | 95          |
| Mesh 8     | 5424140            | 6.63               | 56            | 95          |
| Mesh 9     | 6780140            | 8.53               | 37            | 95          |
| Mesh 10    | 2462890            | 6.63               | 58            | 103         |
| Mesh 11    | 4658160            | 6.61               | 56            | 93          |
| Mesh 12    | 5674130            | 6.63               | 56            | 95          |

The aspect ratio is calculated as the distance from the edge of the cell to the cell centroid over the distance from the face centroid to the cell centroid. More detailed information about the mesh requirements, mesh economy and mesh quality can be found in ANSYS Fluent User's Guide [3].

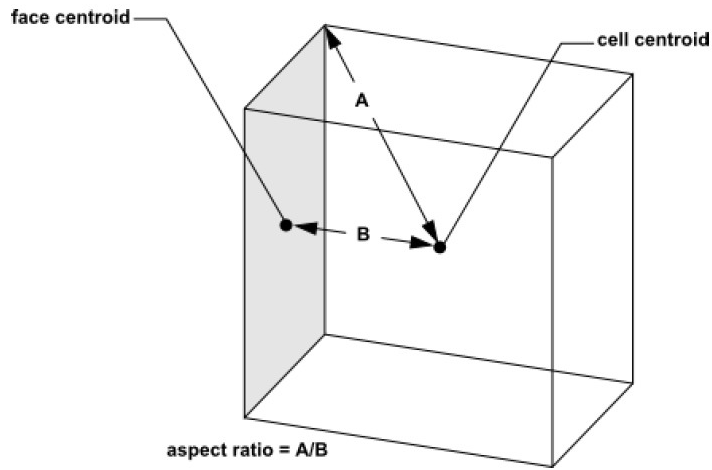


Figure 3.19: Aspect ratio calculation, from [3]

Figure 3.19 demonstrates the calculation of the aspect ratio of the cells used in the mesh. As seen in Figure 3.20 and Figure 3.21, this value affects the performance of the mesh when calculating the flow forces. For instance, Mesh 12 with an aspect ratio of 6.63 shows irregular oscillations in the lift force even though it has the highest number of elements, reaching up to 5674130 elements.

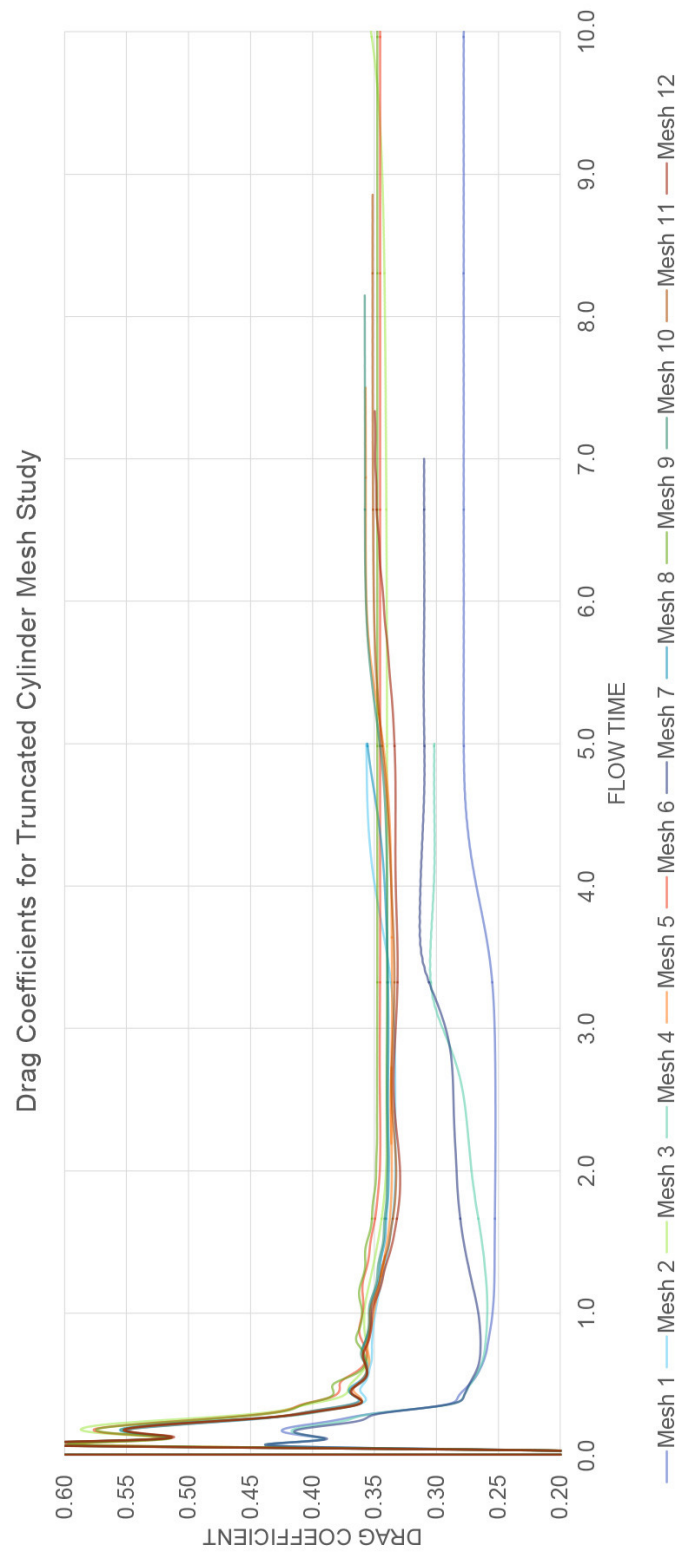


Figure 3.20: Drag coefficients over flow time for truncated cylinder mesh study

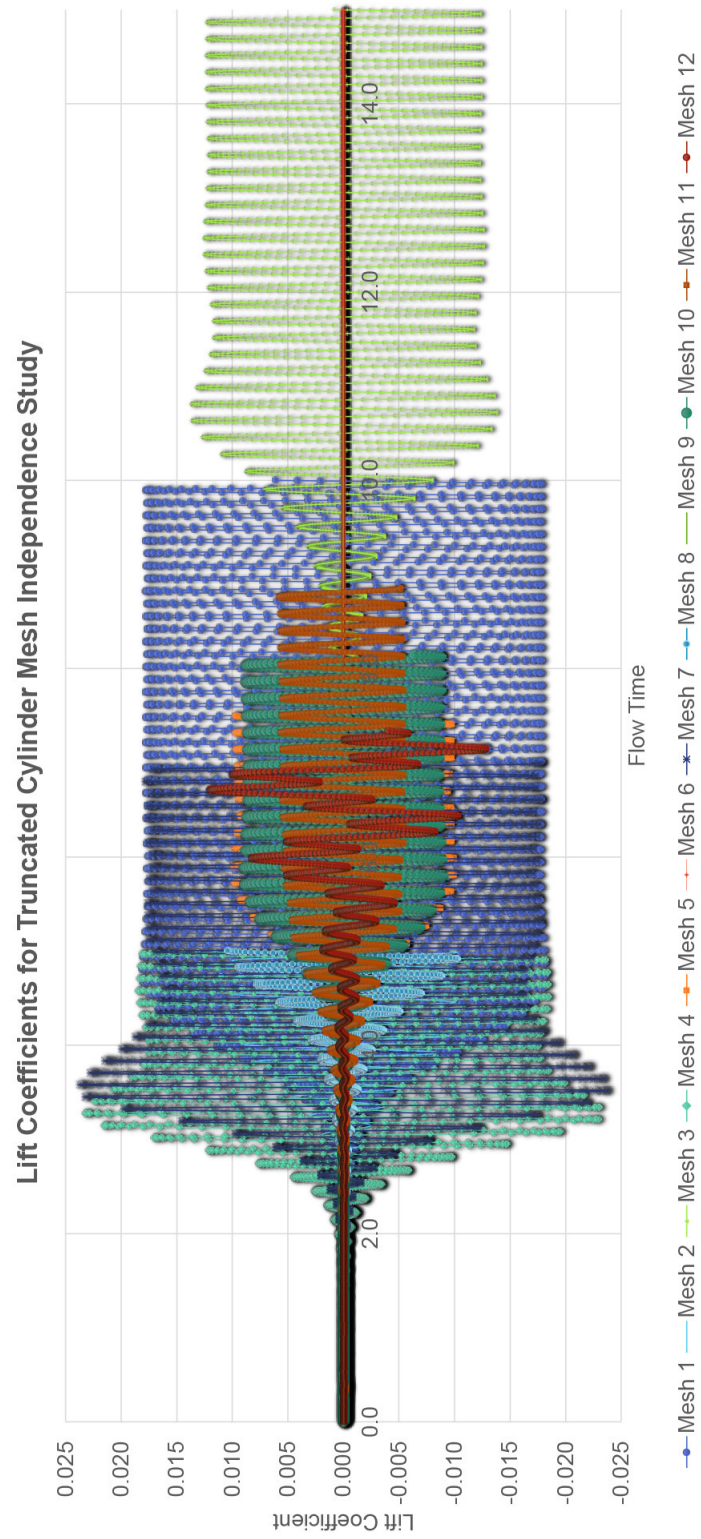


Figure 3.21: Lift coefficients over flow time for truncated cylinder mesh study

Drag values calculated by the created meshes are shown below in Figure 3.22.

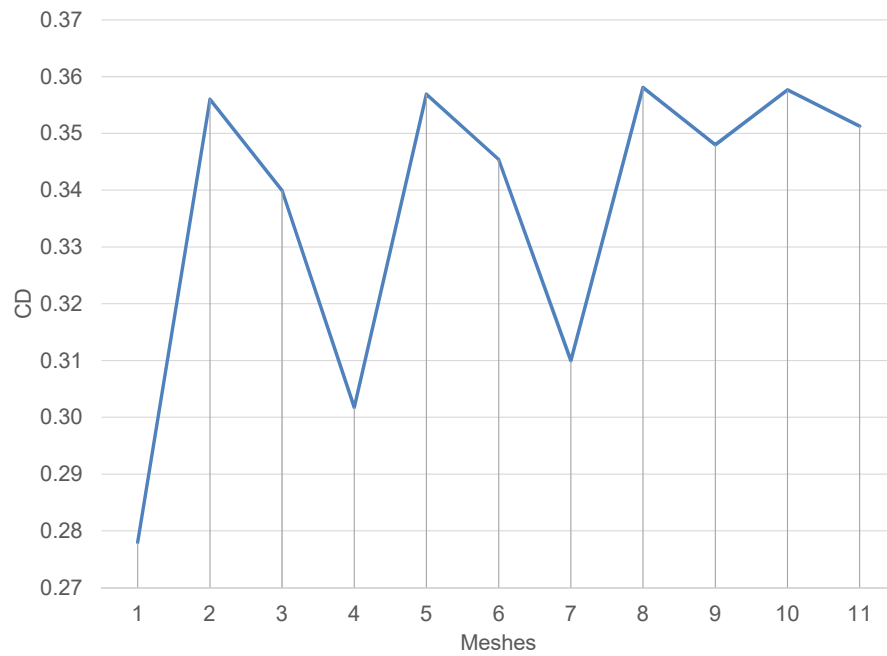


Figure 3.22: Drag Coefficient convergence

Figure 3.23 shows the calculated lift coefficient values among the meshes created. It can be clearly seen that the Mesh 4 shows the highest  $C_{LRMS}$  value among the other meshes.

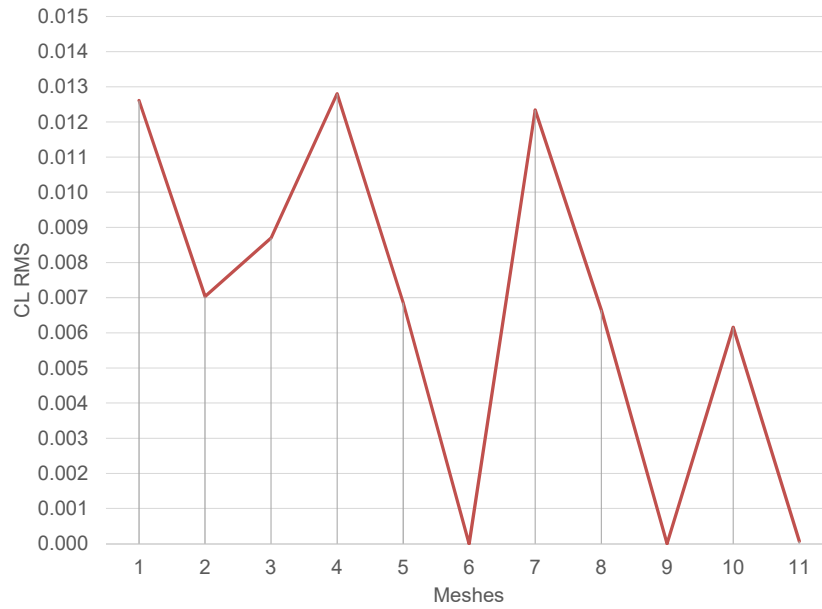


Figure 3.23: Lift Coefficient RMS convergence

Figure 3.24 shows the relation between the mesh cell aspect ratio and the  $C_L RMS$  prediction of the CFD model that was created with this mesh.

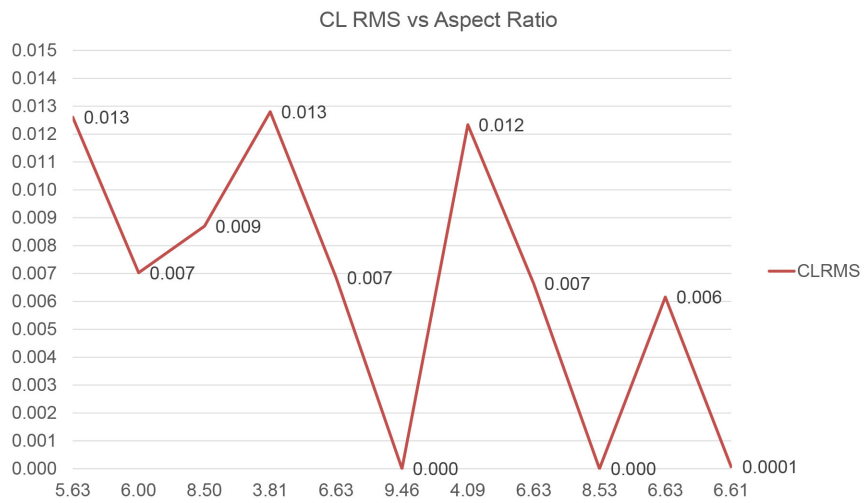


Figure 3.24:  $C_L RMS$  vs. element aspect ratio

Figure 3.25 shows the dimensionless Strouhal number for different meshes

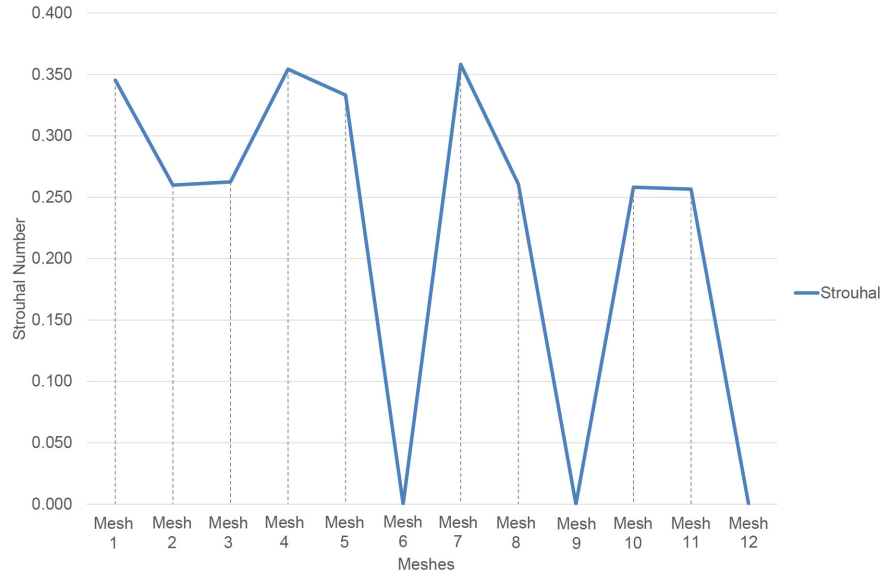


Figure 3.25: Strouhal vs. element aspect ratio

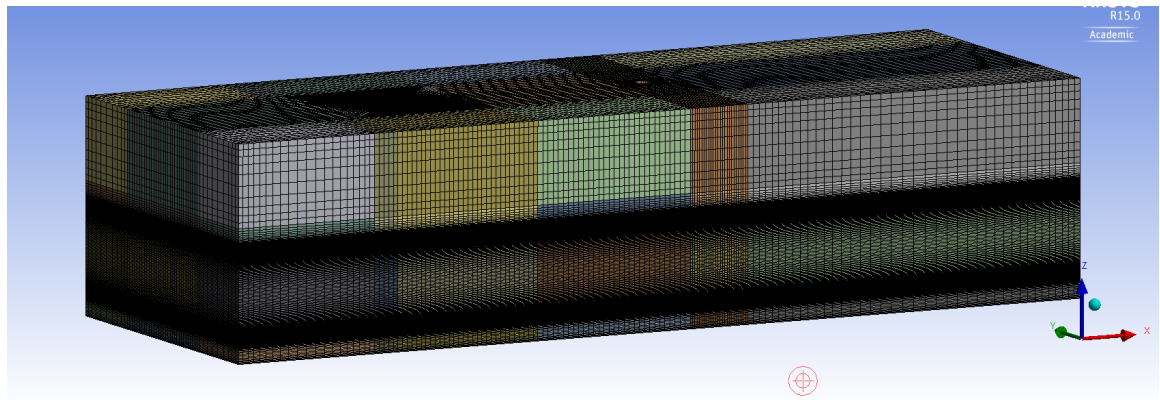
Considering the results of oscillating forces and the frequency of the oscillations, Mesh 4 with an aspect ratio of 3.81 predicted the best values for  $C_{L,RMS}$  and Strouhal number. Thus, for the development of the FSI model this mesh was chosen for the fluid flow modeling.

### 3.4.2.3 Mesh Optimization for Experimental Rig in Flow

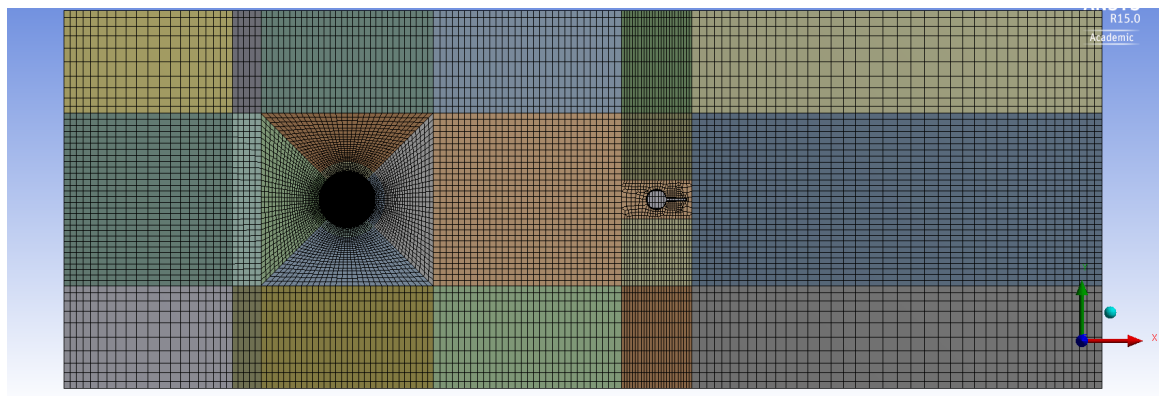
After conducting the mesh dependence studies for finite and infinite cylinders, the CFD mesh was refined within the limits of computational resources. The meshing parameters that was used for Mesh 4 were applied to the last mesh. Further mesh refinements were made around the walls of the main cylindrical support and plate. The horizontal region of the plate thickness was divided into 5 pieces throughout the

CFD domain in order to capture the flow around the plate. An inflation layer mesh control with 4 layers was applied around the cylindrical support with 0.01 m first layer thickness and 1.2 growth rate. The distance from the plate to the bottom of the domain was divided into 15 divisions with a biasing factor of 2.

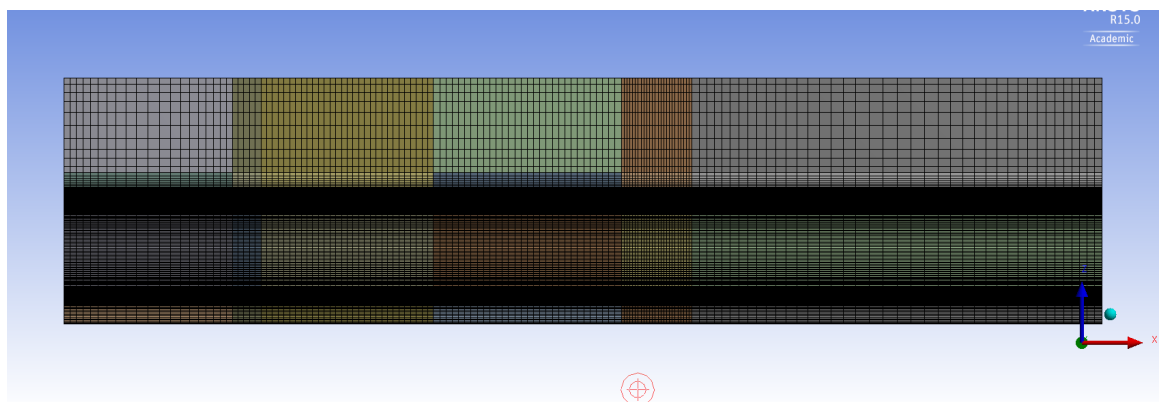
As a result, the mesh shown in Figure 3.26 was created involving 3027800 elements.



(a) CFD mesh perspective view



(b) CFD mesh top view



(c) CFD mesh side view

Figure 3.26: CFD mesh views

### 3.4.3 Turbulence Model

One of the most difficult challenges when designing engineering solutions for offshore operations is turbulence. For small Reynolds numbers, the equations of motion for a viscous fluid would demonstrate a steady solution due to the domination of the viscous stresses. However, at larger Reynolds numbers, the fluid's inertia overcomes the viscous stresses and causes random disorders in flow [57]. At high Reynolds numbers reaching 500 000, the flow speed around the cylinder falls into the supercritical turbulent regime. In this flow regime, vortices rapidly shed. Furthermore, the oscillations of the drag and lift forces significantly affect the FSI problem resulting in the need for accurate solution. Turbulence is three dimensional and time dependent which requires a great deal of information for its full description. For this reason, while investigating the turbulent flows, the significant properties of the flow and the fidelity of the solution should be determined in advance. Unfortunately, there is no turbulent model that can be used universally. Today's computer technologies are not able to solve Navier-Stokes equations with the deterministic method. This method is also known as Direct Numerical Simulation (DNS). However, since this method aims to solve the components of the flow in every scale, it is not applicable for the practical engineering flows with the current computational resources. This requires a statistical approach to the solution. Reynolds introduced time average, the spatial average and the ensemble average in 1895 [58]. These methods introduce a loss of accuracy in the solution; however, they also make the investigation of the significant flow features possible.

Reynolds Averaged Navier-Stokes equations are the derived versions of the Navier-

Stokes equations. They are derived from the substitution of the disintegrated mean and fluctuating scalar quantities of the flow into the continuity and momentum equations [4]. This process resolves the requirement of fine mesh by modeling the turbulence in all grades. However, the approximation introduces unknown variables to the system. As a result, additional equations are needed to be solved in order to close the system. This method, also acknowledged as Reynolds averaged navier-Stokes (RANS) method, is considered as the best compromise in numerical turbulence modeling[57].

The Reynolds Averaged Navier-Stokes Equations (RANS) can be shown as below [4]:

$$\frac{\partial \rho}{\partial t} + \frac{\partial}{\partial x_i}(\rho u_i) = 0 \quad (3.10)$$

$$\frac{\partial}{\partial t}(\rho u_i) + \frac{\partial}{\partial x_j}(\rho u_i u_j) = -\frac{\partial p}{\partial x_i} + \frac{\partial}{\partial x_j} \left[ \mu \left( \frac{\partial u_i}{\partial x_j} + \frac{\partial u_j}{\partial x_i} - \frac{2}{3} \delta_{ij} \frac{\partial u_l}{\partial x_l} \right) \right] + \frac{\partial}{\partial x_j} (-\rho \bar{u}'_i \bar{u}'_j) \quad (3.11)$$

As mentioned earlier, there is no conventional turbulence model that can be used for all flow scenarios while numerically simulating a turbulent flow. Thus, the preference of turbulence model depends on the physics of the flow along with the factors of desired detail scale and accuracy level. Moreover, the dimensions of the computational domain as well as available time and computational resources also carry significance in model selection. Several turbulence models were developed for numerical turbulence modeling such as: zero equation (Prantls Mixing Length, Cebeci-Smith Model), one-equation model (Spart-Allmaras), two-equation models (k- $\epsilon$ , k- $\omega$ ), second order closure (Reynolds stress) and algebraic stress models. It can be seen that Large Eddy Simulation (LES) gained popularity in the recent years. Even though LES requires less refined mesh than DNS, it still requires significantly more refined mesh

than RANS due to the necessity of calculating large eddies in the turbulent flow [57]. RANS models are computationally the most economical and also widely used for simulating industrial flows due to their ability to capture significant flow features within an acceptable accuracy range. These models solve the problem by the help of two additional transport equations and Eddy-Viscosity to estimate Reynolds Stresses.

Considering the computational cost and coupling requirements of the FSI problem, a realizable k- $\varepsilon$  RANS model with non-equilibrium wall functions was used in this study. A Non-equilibrium wall function was chosen due to its performance in calculating the lift and drag forces more accurately than the standard wall functions [4].

Moreover, one of the reasons of choosing the Realizable k- $\varepsilon$  model lies under the term "realizable". As shown below, in the Realizable k- $\varepsilon$  model the eddy viscosity coefficient,  $C_\mu$ , is calculated rather than being used as a constant as in Standard k- $\varepsilon$  model. The turbulent viscosity equations that are used by Realizable k- $\varepsilon$  model are shown below [4]:

$$\mu_t = \rho C_\mu \frac{k^2}{\varepsilon} \quad (3.12)$$

where

$$C_\mu = \frac{1}{A_0 + A_s \frac{kU^*}{\varepsilon}} \quad (3.13)$$

and

$$U^* \equiv \sqrt{S_{ij}S_{ij} + \tilde{\Omega}_{ij}\tilde{\Omega}_{ij}} \quad (3.14)$$

also

$$\tilde{\Omega}_{ij} = \Omega_{ij} - 2\varepsilon_{ijk}\omega_k \quad (3.15)$$

$$\Omega_{ij} = \overline{\Omega_{ij}} - \varepsilon_{ijk}\omega_k \quad (3.16)$$

$\overline{\Omega_{ij}}$  represents the mean rate-of-rotation tensor with angular velocity  $\omega_k$ . The model constants  $A_0$  and  $A_s$  are determined as [4];

$$A_0 = 4.04, A_s = \sqrt{6} \cos \phi \quad (3.17)$$

where  $\phi$  is defined as below [4];

$$\phi = \frac{1}{3} \arccos(\sqrt{6}W), W = \frac{S_{ij}S_{jk}S_{ki}}{\tilde{S}^3}, \tilde{S} = \sqrt{S_{ij}S_{ij}}, S_{ij} = \frac{1}{2} \left( \frac{\partial u_j}{\partial x_i} + \frac{\partial u_i}{\partial x_j} \right) \quad (3.18)$$

Although it is computationally the most expensive k- $\varepsilon$  model, Realizable k- $\varepsilon$  outperforms the traditional k- $\varepsilon$  models thanks to the modifications were made over the years. Transport equations that are solved by the model are shown below [4];

$$\frac{\partial}{\partial t}(\rho k) + \frac{\partial}{\partial x_j}(\rho k u_j) = \frac{\partial}{\partial x_j} \left[ \left( \mu + \frac{\mu_t}{\sigma_k} + \frac{\partial k}{\partial x_j} \right) \right] + G_k + G_b - \rho \varepsilon - Y_M + S_k \quad (3.19)$$

and

$$\frac{\partial}{\partial t}(\rho \varepsilon) + \frac{\partial}{\partial x_j}(\rho \varepsilon u_j) = \frac{\partial}{\partial x_j} \left[ \left( \mu + \frac{\mu_t}{\sigma_\varepsilon} + \frac{\partial \varepsilon}{\partial x_j} \right) \right] + \rho C_1 S \varepsilon - \rho C_2 + \frac{\varepsilon^2}{k + \sqrt{\nu \varepsilon}} + C_{1\varepsilon} + \frac{\varepsilon}{k} C_{3\varepsilon} G_b + S_\varepsilon \quad (3.20)$$

where

$$C_1 = \max \left[ 0.43, \frac{\eta}{\eta + 5} \right], \eta = S \frac{k}{\varepsilon}, S = \sqrt{2 S_{ij} S_{ij}} \quad (3.21)$$

Lastly, model constants that are used in FLUENT by default are shown below [4];

$$C_{1\varepsilon} = 1.44, C_2 = 1.9, \sigma_k = 1.0, \sigma_\varepsilon = 1.2 \quad (3.22)$$

More detailed information about the model can be found in ANSYS Fluent Theory Guide [4].

### 3.4.3.1 Near Wall Treatment

In turbulence modelling, near wall modelling carries a significant role. This is due to the fact that the flow properties extend to very high gradients in the near wall region. This region can be split into three sections: viscous sub layer, buffer layer and fully turbulent layer also known as log-law region. Figure 3.27 below demonstrates these layers in the near wall region[4].

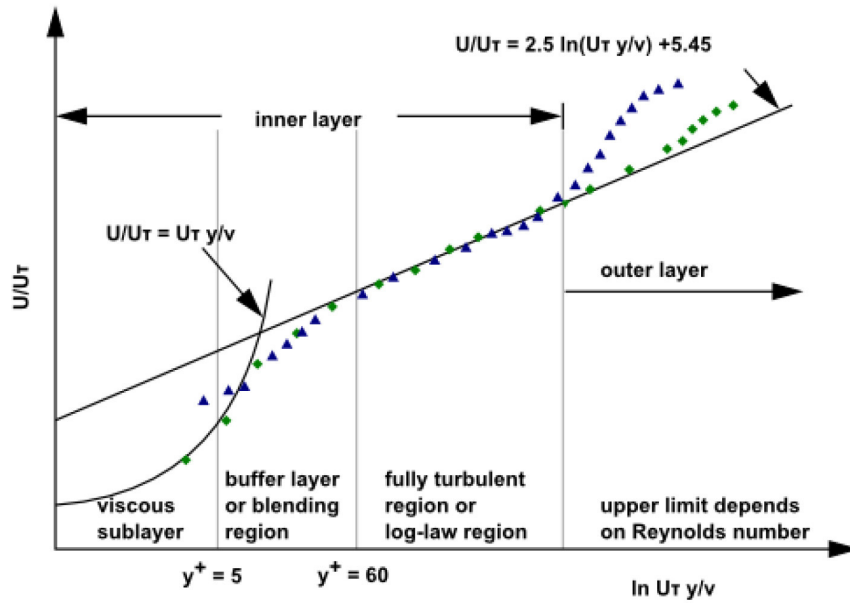


Figure 3.27: Near wall region divisions, from [4]

In the figure above the non-dimensional distance to the wall in the normal direction is represented with  $y^+$ . It is calculated using the following formula[4];

$$y^+ \equiv \rho u_\tau \frac{y}{\mu} \quad (3.23)$$

where  $u_\tau$  is defined as  $\sqrt{\frac{\tau_w}{\rho}}$ . Near wall region can either be resolved or calculated.

It can be calculated with a model that is enabled and capable of resolving the inner, viscosity-affected regions by the aid of a mesh throughout the wall. Secondly, it can be calculated with semi-empirical formulas and linked to the outer boundary layer region. This second strategy is also known as wall functions. Figure 3.28 illustrates these two strategies.

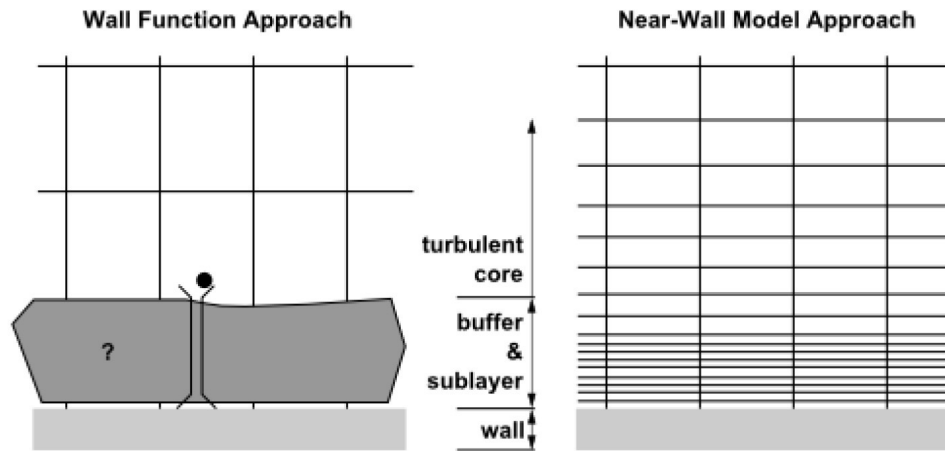


Figure 3.28: Wall functions, from [4]

The use of wall functions helps to decrease computational costs significantly. However, they should be used carefully. For instance, excessive refinements of the mesh in the normal direction to the wall, in other words small  $y^+$  values, can create errors in the solution. This deterioration was observed in certain meshes during the mesh dependence studies that were conducted during this research. Contrary to expectations, certain meshes with  $Y^+$  values lower than 30 showed lower force predictions than the mesh with  $Y^+$  value around 30. The results can be seen in Chapter 3.4.2.1. Owing to its ability to predict the wall shear more accurately, this model was preferred over standard wall functions which is the default wall function option for the Realizable

k- $\varepsilon$  model. ANSYS FLUENT offers several near wall treatment methods with other turbulent models such as Scalable Wall Functions and Enhanced Wall Treatment. Detailed information about available near wall treatments and their characteristics can be found in ANSYS Fluent Theory Guide [4].

### 3.4.4 Simulation Setup

A single phase fluid flow model with Realizable k- $\varepsilon$  turbulence viscous model was used to set up the simulation. Furthermore, for the fluid, liquid water was used from the Fluent material library with a density of  $998.2 \text{ kg/m}^3$  and viscosity of  $1.003 \times 10^{-3} \text{ kg/ms}^{-1}$ . For the flow domain the default operating pressure of 101325 Pa was used.

#### 3.4.4.1 Boundary Conditions

For the solution of Navier-Stokes and momentum equations, appropriate boundary conditions along with initial conditions have to be applied to the flow. ANSYS Fluent offers several boundary conditions for flow inlet and outlets such as: velocity-inlet, mass-flow-inlet and pressure inlet for inlets, and outflow and pressure-outlet for flow exits. Additionally, slip, no-slip and symmetry boundary conditions for wall boundaries are offered. Brief descriptions of these boundary conditions can be found below[3].

#### Velocity Inlet

Assigns the velocity profile at the inlet. For the uniform flow profile, velocity vector along with the scalar velocity can be defined.

### **Mass Flow Inlet**

Can be used when the mass flow rate of the flow is known at the inlet.

### **Pressure Inlet**

Suitable to use with both compressible and incompressible flows. Used to define the total pressure at inlet boundaries.

### **Outflow Outlet**

This outlet boundary condition can be used when the flow velocity and the pressure is not known before the solution of the flow. All other gradients except pressure are assumed zero. Required information is extrapolated from the interior.

### **Pressure Outlet**

Requires the specification of the static pressure at the outlet.

In addition, slip, no-slip along with stationary and moving wall boundary conditions are also available for wall boundary conditions.

### **Wall**

Wall boundary condition is the most basic boundary condition. The fluid cannot pass the flow thus, relative normal velocity is defined as zero.

### **No Slip Wall**

No slip wall boundary condition is a version of the wall where the tangential component of velocity is also set to zero.

## Symmetry Wall

Generally used to decrease computational costs of the model. With this boundary condition the flow factors across a symmetry plane are mirrored [59].

As shown in Table 3.11, velocity-inlet and pressure-outlet type boundary condition was used for inlet and outlet of the fluid domain. The distance between the inlet boundary and cylinder was  $1.5m$  where it is  $4m$  to the outlet. Flow specifications were defined as a velocity of  $3.294m/s$  on X direction. Furthermore, default values 5% and 10 were used for turbulence intensity and viscosity ratio respectively. No slip wall boundary conditions were used for the bottom wall of the domain. In addition, the side and the top walls were assigned as zero shear slip wall.

Lastly, a gravitational acceleration of  $9.80665m/s^2$  was introduced in the model on negative Z axis in order to include its effect on the flow.

Table 3.11: CFD Boundary Conditions

| Parts of the domain | Type of boundary condition |
|---------------------|----------------------------|
| Inlet               | Velocity inlet             |
| Outlet              | Pressure outlet            |
| Cylinder wall       | No slip wall               |
| Plate wall          | No slip wall               |
| Support wall        | No slip wall               |
| Top wall            | Slip wall                  |
| Bottom wall         | No slip wall               |
| Side walls          | No slip wall               |

### 3.4.4.2 Solver Settings

In order to calculate the flow around the experimental rig as well as the rigid and flexible cylinder, a pressure-based transient solver was used. For the purpose of including the gravitational effects on the hydrodynamics, a gravitational acceleration of  $-9.80665m/s^2$  was activated on the Z axis. Table 3.12 lists the type of solution methods that were used in Fluent model. Stated solution methods and schemes were chosen based on examples in the literature and technical support from the ANSYS customer service department.

Table 3.12: FLUENT Solver Settings

| Solution Methods           |                          |
|----------------------------|--------------------------|
| Scheme                     | PISO                     |
| Gradient                   | Least Squares Cell Based |
| Pressure                   | Second Order             |
| Momentum                   | Second Order Upwind      |
| Turbulent Kinetic Energy   | QUICK                    |
| Turbulent Dissipation Rate | Second Order Upwind      |
| Transient Formulation      | Second Order Upwind      |

Under relaxation factors (URF) were left at the default settings. By default, URF for pressure is 0.3, where it is 1 for density, body forces and turbulent viscosity, 0.8 for turbulent kinetic energy and turbulent dissipation rate. Lastly, URF for momentum is 0.7. The solution was initialized with standard initialization where it was computed

from the inlet with a velocity of  $3.294m/s$  on X direction. Residual monitoring was set to an absolute criteria of 0.00001 for continuity, X-velocity, Y-velocity, Z-velocity, k and  $\varepsilon$ . The calculation was run with a time step of  $2.5ms$  with maximum 50 iterations per time step. The solution was completed for 2000 time steps and thus 5 seconds of flow time.

#### **3.4.4.3 Time Step Dependence Study for CFD Model**

In transient simulations, the accuracy of the solution is affected by the time step size in addition to mesh. Considering this, a time step dependence study was conducted in order to obtain the most accurate solution for the numerical model. As can be seen in Table 3.13, six different time steps were used ranging from 0.01 s to 0.625 ms. The most accurate time step size was obtained as 1.25 ms. Considering the computational costs for the FSI simulations, a bigger time step size of 2.5 ms was initially chosen. The CFD solution with a 2.5 ms time-step size showed an insignificant difference in calculation of the Strouhal number from the time-step independent solution with an error of 0.56%. However, as mentioned in the System Coupling section, this time step size was too big for two-way coupled analysis due to the dynamic meshing requirements. Thus, the global time-step size of a 2.5 milliseconds were used for one-way coupling and one millisecond was used for two-way coupled FSI simulations. The comparison for the time step size and corresponding the Strouhal numbers can be seen in Table 3.13 and Figure 3.29.

Table 3.13: Parameters

| Mesh            | Mesh 4d | Mesh 4c | Mesh 4 | Mesh 4e | Mesh 4a | Mesh 4b  |
|-----------------|---------|---------|--------|---------|---------|----------|
| Time Step       | 0.01    | 0.005   | 0.0025 | 0.002   | 0.00125 | 0.000625 |
| Strouhal Number | 0.330   | 0.350   | 0.354  | 0.355   | 0.356   | 0.355    |
| $C_L$ RMS       | 0.0117  | 0.0126  | 0.0128 | 0.0129  | 0.0130  | 0.0127   |
| $C_D$           | 0.299   | 0.301   | 0.302  | 0.282   | 0.302   | 0.302    |
| % St            | 92.70   | 98.31   | 99.44  | 99.85   | 100.00  | 99.72    |

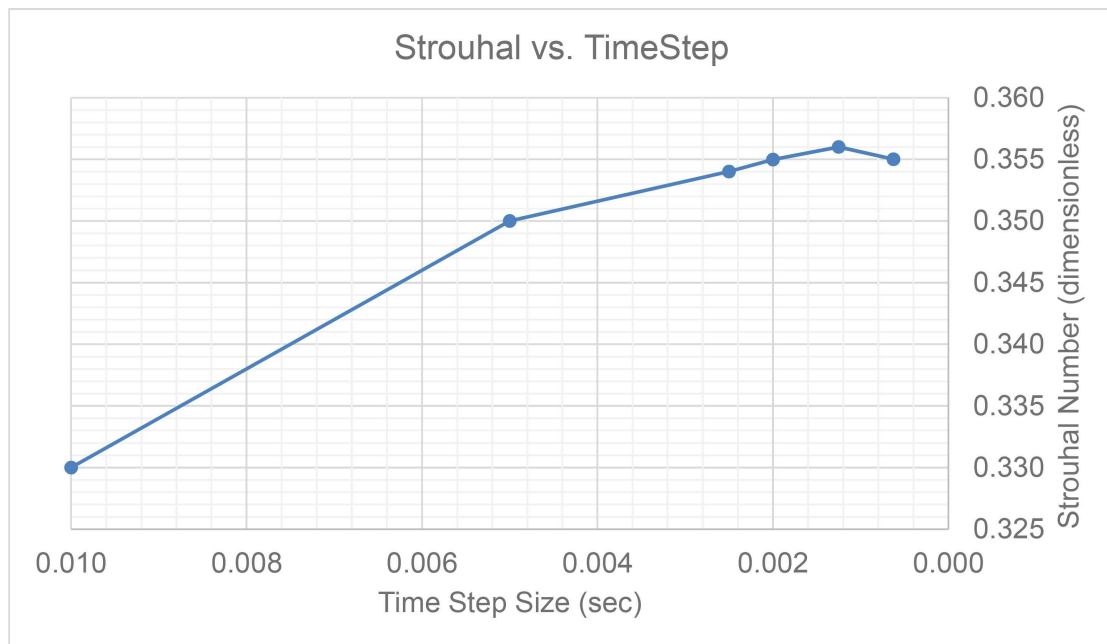


Figure 3.29: Strouhal convergence

### 3.5 System Coupling

The last step of a Multi-Physics simulation is the coupling of the particular modules/solvers. For this purpose System Coupling module was used. Figure 3.30 illustrates the workbench work flow for a coupled analysis between ANSYS Mechanical and ANSYS FLUENT solvers within ANSYS Workbench environment.

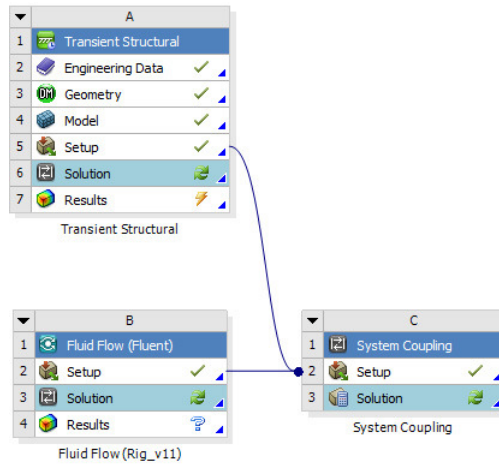


Figure 3.30: Workbench coupling work scheme

During the coupling process, transferring data between solvers occurs in every time step and is repeated with additional coupling iterations until it either achieves the convergence criteria or reaches the maximum number of iterations. For both one-way and two-way coupled analyses, a minimum 2 and maximum of 5 iterations were set. In addition, the convergence criteria between the solvers was fixed to 0.001. As previously mentioned, a global time-step size of 1 millisecond was chosen for the coupled analyses.

For the purpose of being able to restart the FSI simulation in case of crashes, Interme-

diated Restart Data Outputs were set to 250 under System Coupling Execution Control settings. In addition to System Coupling, several settings for restarting purposes were set in the Mechanical module. Under Analysis Settings, "Generate Restart Points" were set to Yes and under Analysis Data Management, "Delete Unneeded Files" setting was set to No. These additional steps were crucial in order to start the transient mechanical simulation from the desired load step and sub-steps. Similarly, FLUENT module was set properly to save every 100 time step data of the fluid flow solution.

### **3.5.1 One-Way Coupling**

Initially, one-way coupling model was created. For this purpose, three data transfers were established between the Mechanical and CFD FSI interfaces. A data transfer only sends one type of variable from the source to the target region and the sequence of this data transfer happens from FLUENT to ANSYS Mechanical. Each data transfer was created for the cylinder, plate and support regions individually to send force variables. Between the FSI regions of Mechanical and CFD, 100% mapping was established within ANSYS System Coupling. While running FSI simulations on the cluster environment, this information can be accessed within the System Coupling log file.

Figure 3.31 demonstrates the one-way coupling procedure[42].

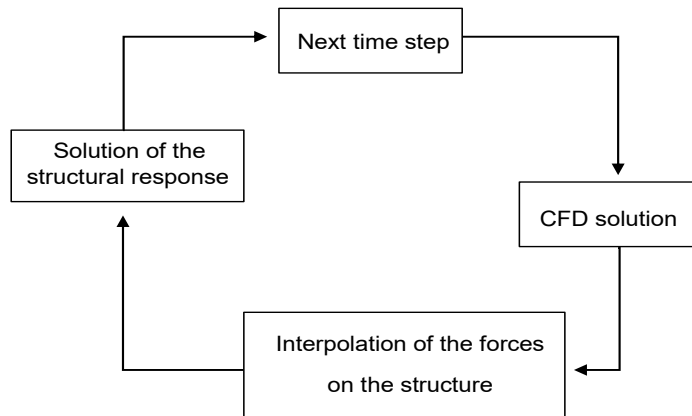


Figure 3.31: One-way coupling scheme

### 3.5.2 Two-Way Coupling

In addition to one-way coupled analysis, two data transfers were created for the cylinder in the process of developing the two-way coupled analysis. For one-way coupled analysis, Fluent solves the RANS equations for the whole fluid domain and sends the results on the cylinder, plate and support. However, for a two-way coupled analysis, deformations caused by hydrodynamic forces are also transferred back to fluid domain with the help of dynamic mesh algorithms. This concludes one time step of the calculation in case of convergence of both solutions. As distinct from the one-way coupled FSI simulation, another data transfer was created within System Coupling. Thus, the two-way coupled analysis setup includes 3 data transfers for the force variables and one data transfer for the nodal displacements.

Outlines of the system coupling schematics of one-way and two-way coupling can be seen in Figure 3.32

| Outline of Schematic C1: System Coupling |                                  | Outline of Schematic C1: System Coupling |                                  |
|--|----------------------------------|--|----------------------------------|
| A  |                                  | A  |                                  |
| 1  | System Coupling                  | 1  | System Coupling                  |
| 2  | Setup                            | 2  | Setup                            |
| 3  | Analysis Settings                | 3  | Analysis Settings                |
| 4  | Participants                     | 4  | Participants                     |
| 5  | Fluid Flow (Rig_v11)             | 5  | Fluid Flow (Rig_v11)             |
| 14                                       | Transient Structural Mesh 3      | 14                                       | Transient Structural             |
| 15                                       | Regions                          | 15                                       | Regions                          |
| 16                                       | FSI Cylinder                     | 16                                       | FSI Cylinder                     |
| 17                                       | FSI Plate                        | 17                                       | FSI Plate                        |
| 18                                       | FSI Support                      | 18                                       | FSI Support                      |
| 19                                       | Data Transfers                   | 19                                       | Data Transfers                   |
| 20                                       | Force Transfer Cylinder          | 20                                       | Data Transfer Plate              |
| 21                                       | Force Transfer Plate             | 21                                       | Data Transfer Support            |
| 22                                       | Force Transfer Support           | 22                                       | Cylinder Force                   |
| 23                                       | Execution Control                | 23                                       | Cylinder Deformation             |
| 24                                       | Co-Sim. Sequence                 | 24                                       | Execution Control                |
| 25                                       | Debug Output                     | 25                                       | Co-Sim. Sequence                 |
| 26                                       | Expert Settings                  | 26                                       | Debug Output                     |
| 27                                       | Intermediate Restart Data Output | 27                                       | Expert Settings                  |
| 28                                       | Solution                         | 28                                       | Intermediate Restart Data Output |
| 29                                       | Solution Information             | 29                                       | Solution                         |
| 30                                       | System Coupling                  | 30                                       | Solution Information             |
| 31                                       | Fluid Flow (Rig_v11)             | 31                                       | System Coupling                  |
| 32                                       | Transient Structural             | 32                                       | Fluid Flow (Rig_v11)             |
| 33                                       | Chart Monitors                   | 33                                       | Transient Structural             |
| 34                                       | Chart                            | 34                                       | Chart Monitors                   |

Figure 3.32: Coupling setup, one-way (left) and two-way (right)

The process scheme for a single time-step of two-way coupled analysis can be seen in Figure 3.33[42].

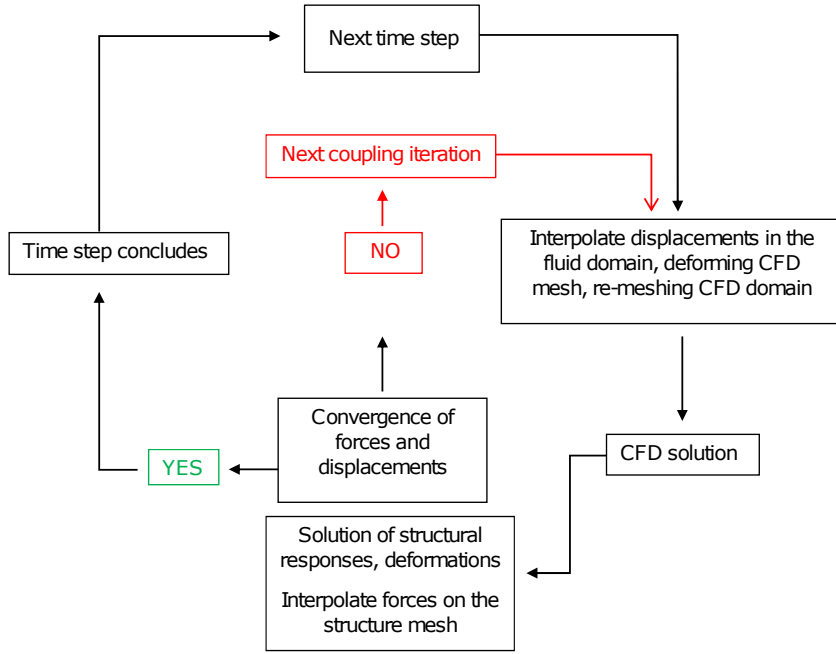


Figure 3.33: Two-way coupling scheme

For the purpose of mesh updating, diffusion based smoothing along with local cell and local face re-meshing methods were applied. In the smoothing method, the number of nodes and their connections do not change. However, the interior nodes of the mesh moves. The mesh motion is governed by the diffusion equation shown as follows [4]:

$$\nabla \cdot (\Psi \nabla \vec{u}) = 0 \quad (3.24)$$

where  $\vec{u}$  represents the mesh displacement velocity and  $\Psi$  represents the diffusion coefficient. The local cell re-meshing only affects triangular and tetrahedral mesh cells that exceed the skewness or size criteria due to large displacements. By doing so, it prevents convergence problems in the solution that can be caused by negative cell volumes.

### 3.6 Different Simulation Cases

In order to investigate the behaviour of the submerged flexible cylinder, 5 different cases were run. For these runs, the same CFD model was used except for the ones with dynamic meshing. Base case included a cylinder with rigid material as explained on Page 52. Since large displacements were not expected, this case was solved with one-way coupled FSI simulation.

Case 1 included a flexible cylinder; however, it was solved with one-way coupled analysis initially.

Case 2 included a more flexible cylinder and was solved with one-way coupled analysis in order to compare the effects of flexibility with one-way coupled method.

Lastly, in Case 3 and Case 4, a cylinder with same material properties in Case 1 and Case 2 was solved with two-way coupling. The thickness of the cylinder was designed as 0.02 m for all the investigated cases. Material properties along with FSI solution methods of the cylinder for each case is shown in Table 3.14 below.

Table 3.14: Different simulation cases

| Cases     | Cylinder Material | Young's Modulus (Pa) | Simulation Type     |
|-----------|-------------------|----------------------|---------------------|
| Base case | Rigid             | 2e+11                | One-way coupled FSI |
| Case 1    | Flexible          | 2e+09                | One-way coupled FSI |
| Case 2    | Flexible          | 2e+08                | One-way coupled FSI |
| Case 3    | Flexible          | 2e+09                | Two-way coupled FSI |
| Case 4    | Flexible          | 2e+08                | Two-way coupled FSI |

# Chapter 4

## Results and Discussion

In order to provide insight about the fluid-structure interaction of the test cylinder and the endurance of the experimental rig, the results of five different cases with varying material properties and coupling methods for the cylinder are presented. The flow behavior is analyzed with the aid of streamlines and contour plots of mean-velocity and fluctuation components. Additionally, the dynamic responses of the cylinder and the experimental rig are analyzed with deformations and von-Mises stresses.

### 4.1 Validation of the CFD Model

A numerical investigation of the flow around a finite cylinder at a critical Reynolds number using the Realizable RANS model has been carried out as part of the FSI model development. The following section compares the results of the CFD model with literature data in order to validate the numerical fluid flow model. All cited data from the literature was digitized by the open source software, Engauge 7.2.

## Pressure Coefficient

Circumferential pressure distributions are presented from available experimental and numerical studies. The pressure coefficient curve obtained from the numerical fluid flow model from the current study shows a less negative pressure around the separation point when compared to other studies. This can be attributed to the effect of the free end; Fox and West [18] observed a notable effect on the mean pressure distributions in the presence of a free end. They reported an increase in the wake pressure due to down-wash flow, which generally means reduced pressure for a finite cylinder. The reduction in pressure can be attributed to the separation of the fully turbulent boundary in other studies with a higher Reynolds number. In the present study, which utilizes a lower Reynolds number of 500000, the transition may still be in progress. As seen in Figure 4.1, the trend of the pressure coefficient over the circumference of the cylinder shows similar behavior from the stagnation point to separation. As mentioned by Okamoto and Yagita [10] an inflexion point in the pressure curve after the minimum pressure indicates separation. Furthermore, from the comparison of the inflexion points in the curves it can be seen that separation occurs in a similar vicinity, compared to the other studies.

Summing up the results, it can be concluded that the calculated pressure coefficient distribution shows a good agreement with the other studies ([29],[13], [7]) considering the finite length of the cylinder.

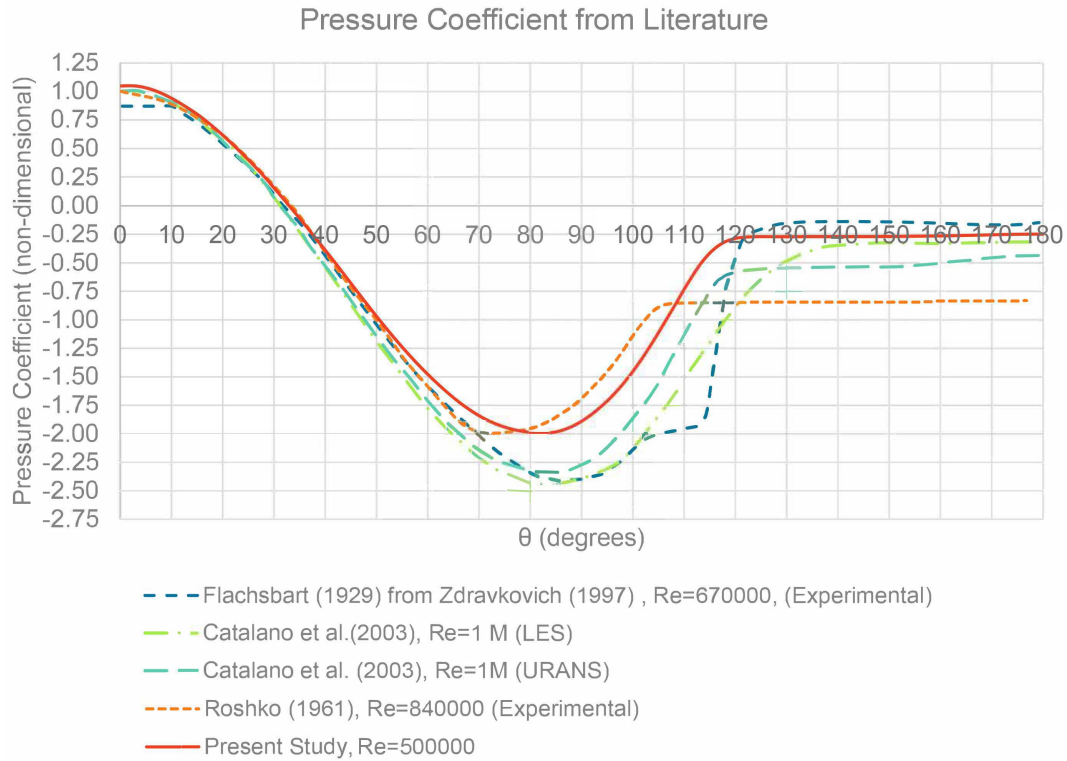


Figure 4.1: Pressure coefficients for a circular cylinder from literature

## Drag Coefficient

Results from several experimental and numerical investigations of the flow around a circular cylinder are shown in Figure 4.2. Fox and West [18] reported a notable relation between the drag pressure and aspect ratio of the cylinder when the aspect ratio is less than 13. They reported an increase in the wake pressure and reduced drag pressure for the finite cylinder compared to an infinite cylinder.

However, Achenbach [19] investigated the flow around a smooth cylinder with a similar aspect ratio to the present study with a value of 3.33. He measured the local pressure and skin friction distribution and calculated the drag coefficient from these measurements. From the outcome of the present investigation, it is possible to

conclude that the fluid flow model calculates the drag coefficient with good agreement with other literature data from [29], [60], [17], [54], [16],[61] particularly with that of Achenbach[19].

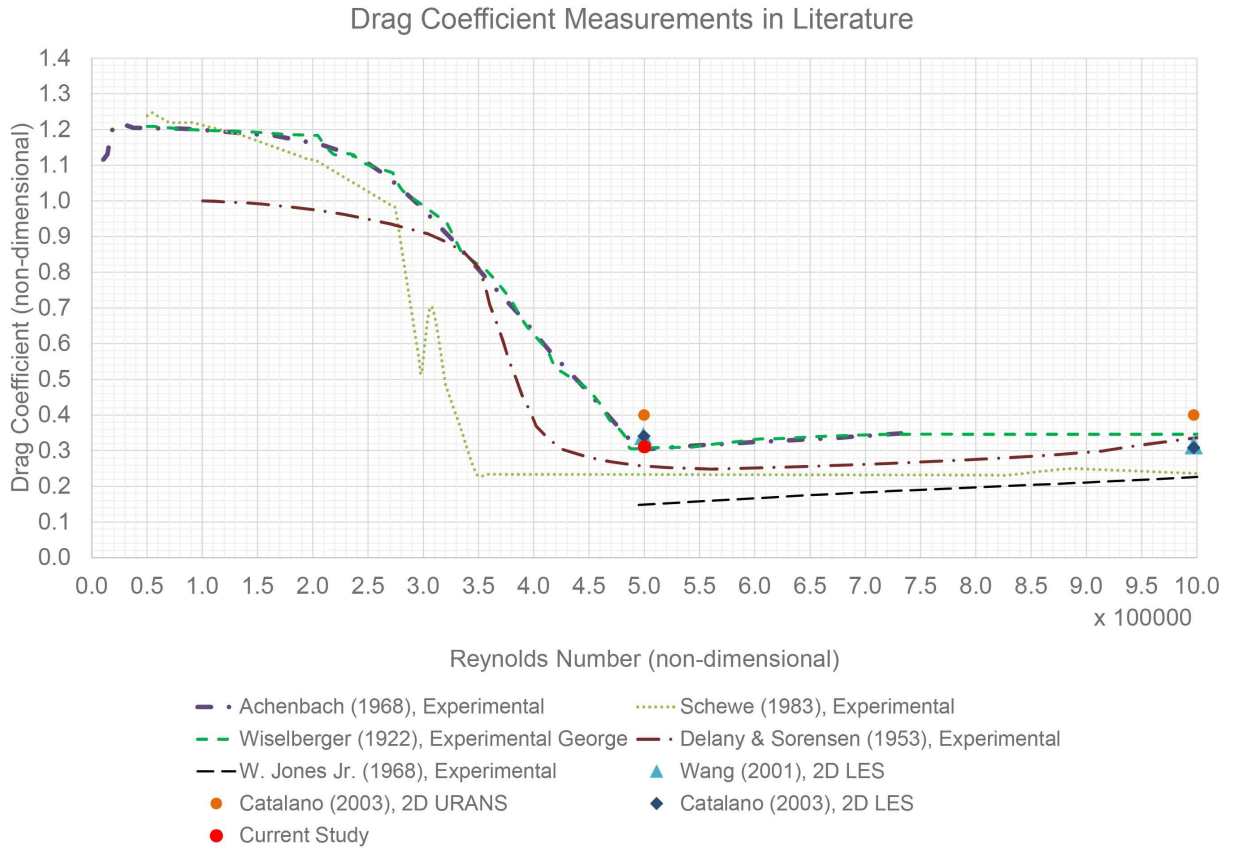


Figure 4.2: Drag coefficients for circular cylinder from literature

### Lift Coefficient

In most applications involving cylindrical structures, the lift force is significantly smaller than the drag force which results in a smaller structural response from the cylinder. This might be one of the reasons that the lift force around the cylinder is less commonly investigated than the drag force.

Moreover, the effect of the free end along with the aspect ratio of the cylinder and the influence of the Reynolds number on the flow around the tip of the cylinder are not fully understood [62]. Consequently, experimental results for a finite cylinder mounted on a similar experimental rig with an aspect ratio of 4 in a flow with a Reynolds number of 500000 could not be found for direct comparison. However, the validation of the model considering the lift force was studied with the aid of the root mean square value from several related studies. The results of the root mean square of the lift coefficient for circular cylinders are shown in Figure 4.3.

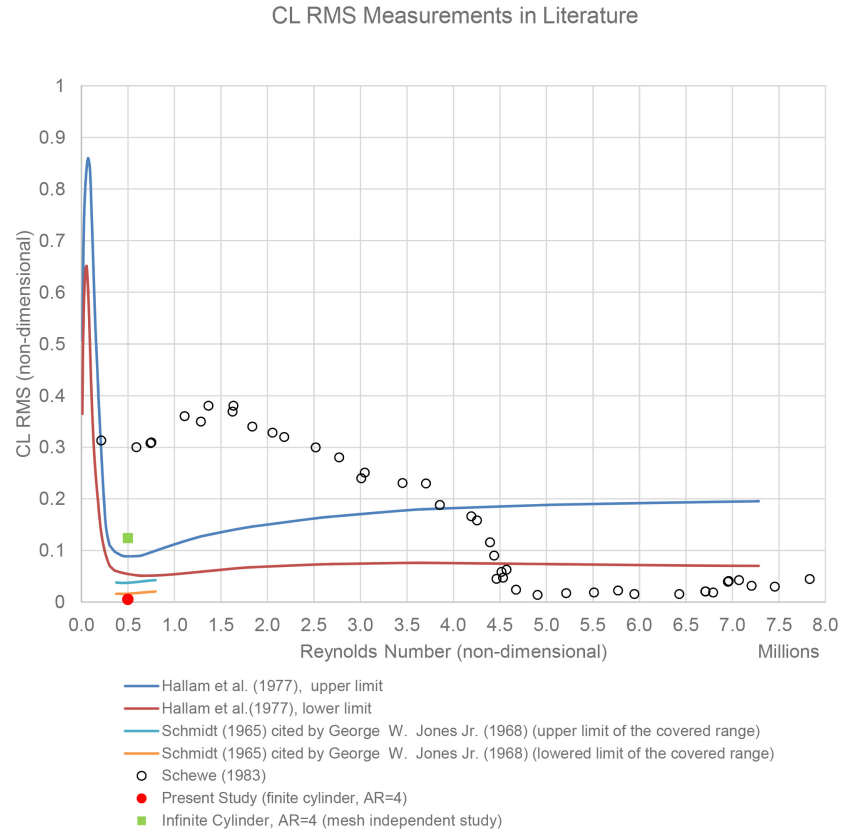


Figure 4.3: RMS lift coefficient for circular cylinder from literature

As seen in Figure 4.3, the lift RMS value for the finite cylinder mounted on the rig is significantly lower than the value of the infinite cylinder which was mentioned in the mesh dependence study section of Chapter 3 of this thesis. The infinite cylinder lift RMS value shows a good agreement with the literature data from [17], [52] cited in [6], [53].

However, the finite cylinder RMS value is significantly lower. According to Fox and West [63], this is expected. Furthermore, it can be seen from Figure 4.4 [64] cited in [65], that the ratio of the lift coefficient for the finite cylinder to that of an infinite cylinder is approximately 0.1 for the present study.

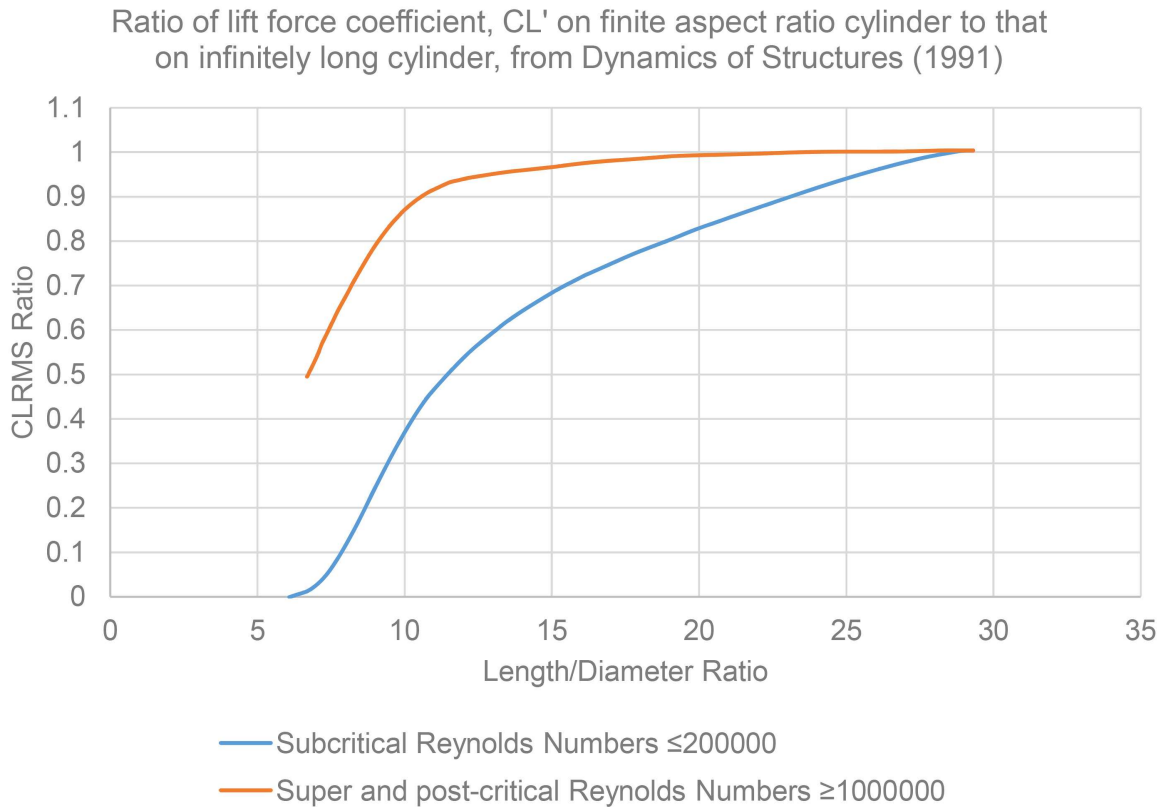


Figure 4.4: Ratio of lift force coefficient on finite cylinder to that on infinite cylinder

To sum up, the data obtained indicates a similar trend for the small RMS lift coefficient value of the finite cylinder with an aspect ratio of 4. Thus, it can be said that the results show acceptable agreement.

### **Strouhal Number**

Strouhal numbers from several studies are shown in Figure 4.5. It can be seen from this figure that for a Reynolds number of 500000, the value of the Strouhal is approximately 0.45 for cylinders with larger aspect ratios of 5 and 10 [56]. As mentioned in the literature review, Fox and West [18] reported a relation between the aspect ratio and the Strouhal number for cylinders with aspect ratios smaller than 13. They reported that the Strouhal number increased with the aspect ratio until it reached a value of 13. This relation can be seen from the comparison of Zan [56]'s result for aspect ratios of 5 and 10 and the current study with an aspect ratio of 4.

It is evident that in comparison to the results from the literature ([54],[55], [56]), the fluid flow model performed similarly when calculating the Strouhal number. Thus, the results of the current study are in good agreement with the results from the literature.

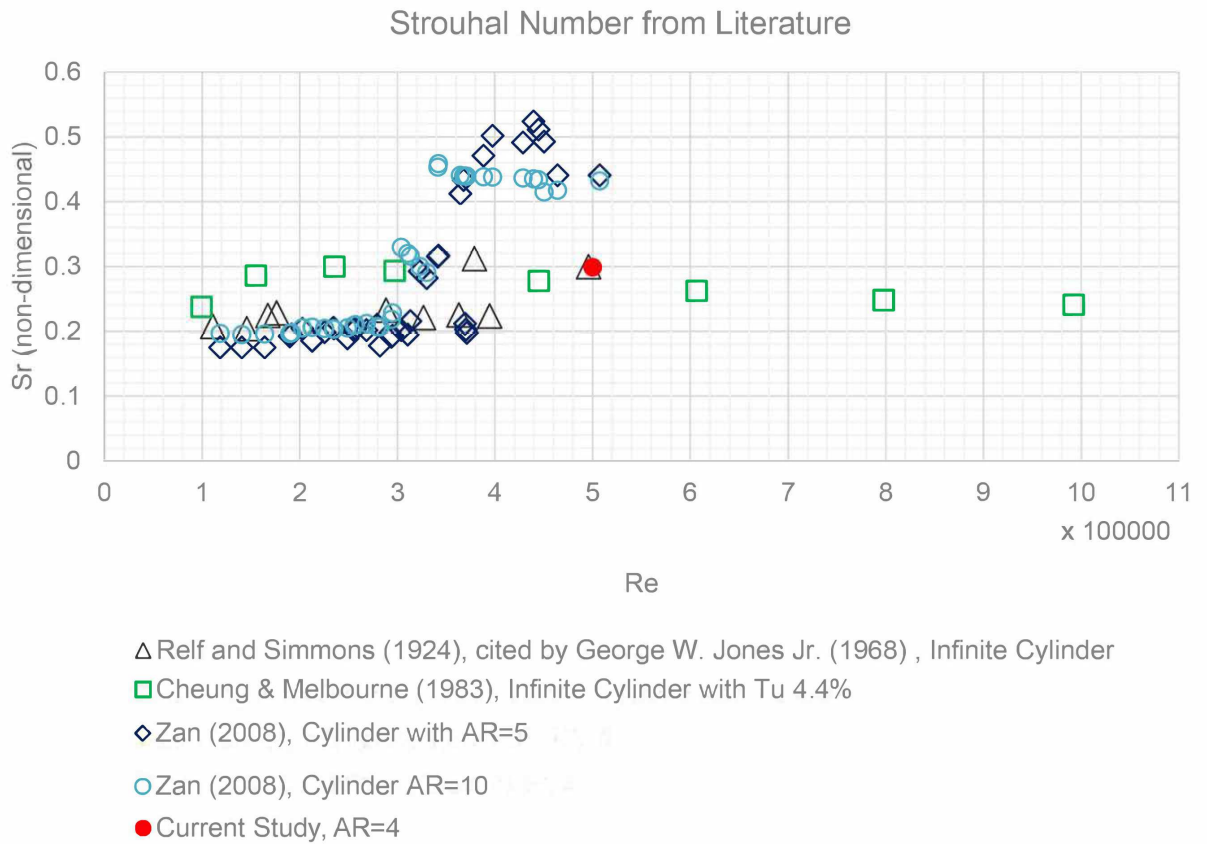


Figure 4.5: Strouhal number for circular cylinder from literature

In general, the data obtained for pressure, lift and drag coefficients along with Strouhal number are consistent with the major trends in literature compared to other experimental and numerical work. Therefore, the current numerical fluid flow model is judged to be sufficient for use in further FSI investigation of flexible submerged cylinders.

## 4.2 Investigated Cases

For all investigated cases, the cylinder thickness was chosen as 0.02 m. The flow was at Reynolds  $5 \times 10^5$ , with a flow speed of  $3.294 \text{ m/s}$ . FSI on the experimental rig was investigated with one-way coupling, whereas the coupling method for the FSI investigation on the cylinder varied between cases. All simulations were started by coupling the fluid flow simulations that were at a steady state after 3 seconds of initial time. One-way coupled simulations were completed for 1000 coupling steps (2.5 s) and two-way coupled simulations were completed for 500 coupling steps (0.5 s). 2500 coupling steps for one-way coupled simulations were completed in approximately 19 hours using 16 cores for Structural and 48 cores for CFD solver for each case. On the other hand, 500 coupling steps for each two-way coupled simulation were completed in approximately 116 hours using 16 cores for Structural and 32 cores for CFD solver. A cylinder can be considered rigid if its deformation remains at less than 1/200th of its diameter [65]. The base case investigated involves a cylinder with a default structural steel material property [50]. The Young's modulus of the material was left as it is,  $2 \times 10^{11}$ . Excluding the base case, all the cases investigated involve a cylinder with a modified structural steel material property. The Young's modulus of the material was decreased to  $2 \times 10^9$  for Case 1 and Case 3. For Case 2 and Case 4 it was reduced to  $2 \times 10^8$  which provided more flexibility. These cases were included for the comparison of one-way and two-way coupled FSI solution methods for solving the structural responses of different materials. The force transfers for the experimental rig were in one direction for all the cases which was from CFD solver to structural solver. However, for cases 3 and 4, the data transfers for the cylinder were completed

as two way transfers, making it a one-way coupling for the rig and two-way coupling for the cylinder. Summarized properties of all the investigated cases can be found in Table 4.1.

Table 4.1: FSI Cases

| Case      | Coupling Method | Cylinder Young's Modulus (Pa) | Coupling Steps | Time (s) |
|-----------|-----------------|-------------------------------|----------------|----------|
| Base Case | One-way         | $2 \times 10^{11}$            | 2500           | 2.5      |
| Case 1    | One-way         | $2 \times 10^9$               | 2500           | 2.5      |
| Case 2    | One-way         | $2 \times 10^8$               | 2500           | 2.5      |
| Case 3    | Two-way         | $2 \times 10^9$               | 500            | 0.5      |
| Case 4    | Two-way         | $2 \times 10^8$               | 500            | 0.5      |

### 4.2.1 Base case

For the one-way coupling cases, the base case and Case 1 and Case 2, the CFD domain remains intact, meaning the fluid forces acting on the cylinder are not affected by the deformations and are identical for all one-way coupled cases. Figure 4.6 shows the non-dimensional lift and drag coefficients of the hydrodynamic forces acting on the cylinder over time. The mean drag coefficient oscillates around 0.311 whereas the root mean square value for the lift coefficient is 0.005 and the Strouhal number is 0.299. These values are slightly different compared to the single finite cylinder model. The mesh parameters that represent the mesh converged solution for the fluid flow modelling of the finite cylinder were used for modelling the cylinder on the experimental rig.

However, there is a slight, expected difference in these hydrodynamic forces since the numerical models are not identical.

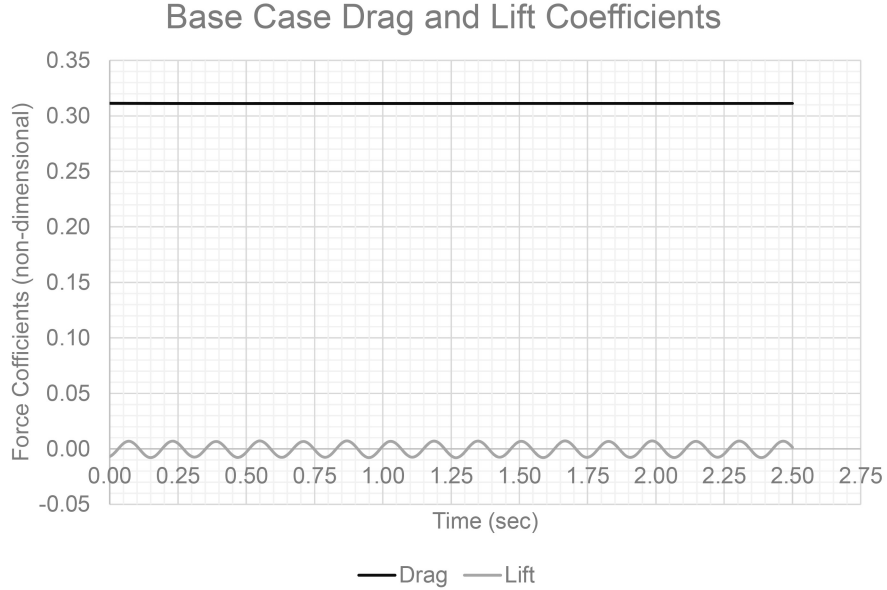


Figure 4.6: Lift and drag coefficients for base case over time

Velocity contours plotted on the vertical and horizontal planes of the fluid flow solution for the base case, Case 1 and Case 2 can be seen in Appendix A.

Figure 4.7 illustrates the directional deformations of the cylinder due to the hydrodynamic forces shown in Figure 4.6. A significant difference between the structural reactions to drag and lift forces can be seen. Figure 4.8 illustrates the maximum von-Mises stress values for the base case over time. The highest stress occurs at 0.0625 sec with a value of 68.78 MPa. The distribution of the von-Mises stress was demonstrated in Figure 4.9 and deformations were scaled up 150 times for visibility purposes. It can be seen that the highest stress occurs in the vicinity of the front support connections.

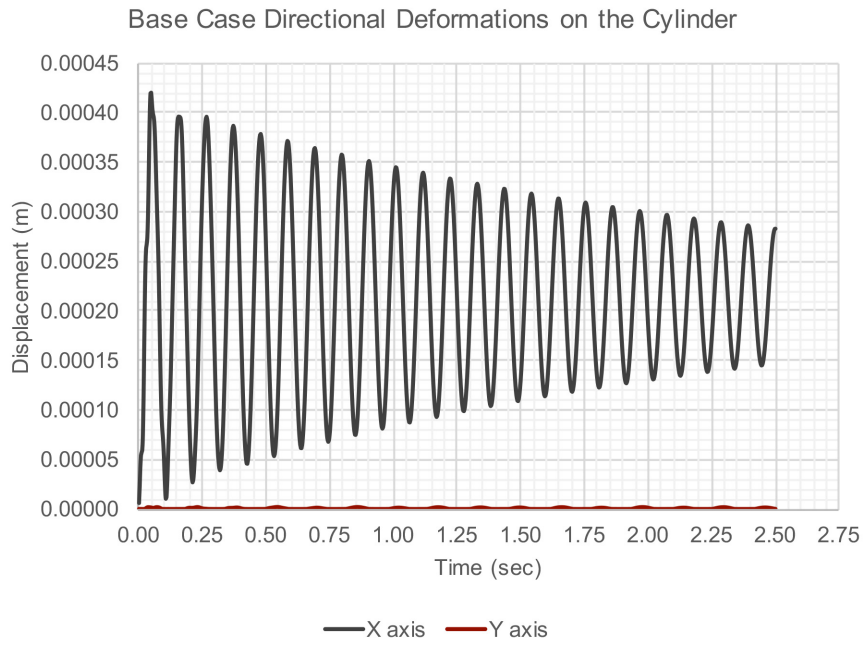


Figure 4.7: Cylinder directional deformations for base case

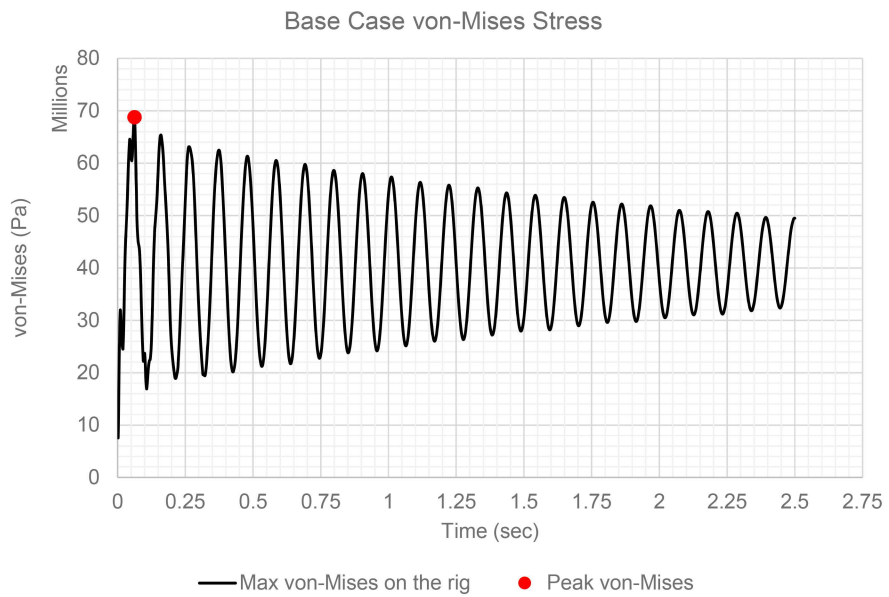


Figure 4.8: Base case maximum von-Mises stress over time

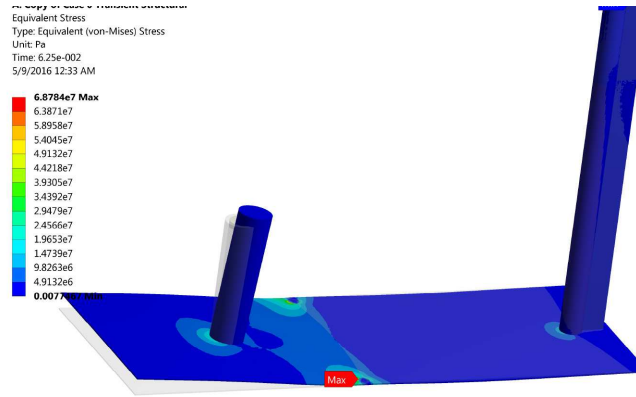


Figure 4.9: Base case peak von-Mises Stress

#### 4.2.2 Case 1

The first case includes a cylinder with modified material properties in order to provide flexibility. However it was solved with one-way coupling. Thus, the hydrodynamic forces are identical to the ones in the base case. In order to demonstrate the structural response of the cylinder, directional deformations were investigated. Figure 4.10 represents the directional deformations of cylinder in x and y axes along with the behaviour of the hydrodynamic force coefficients of the cylinder over time. The lift coefficient was magnified 10 times for providing a better comparison.

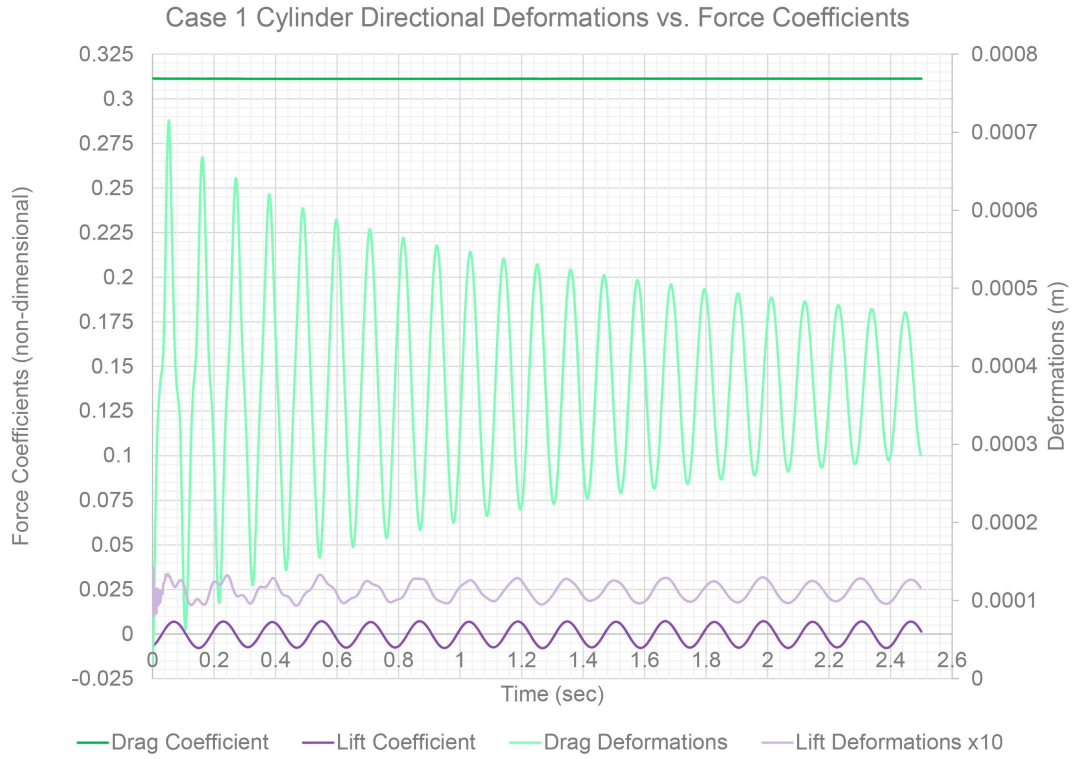
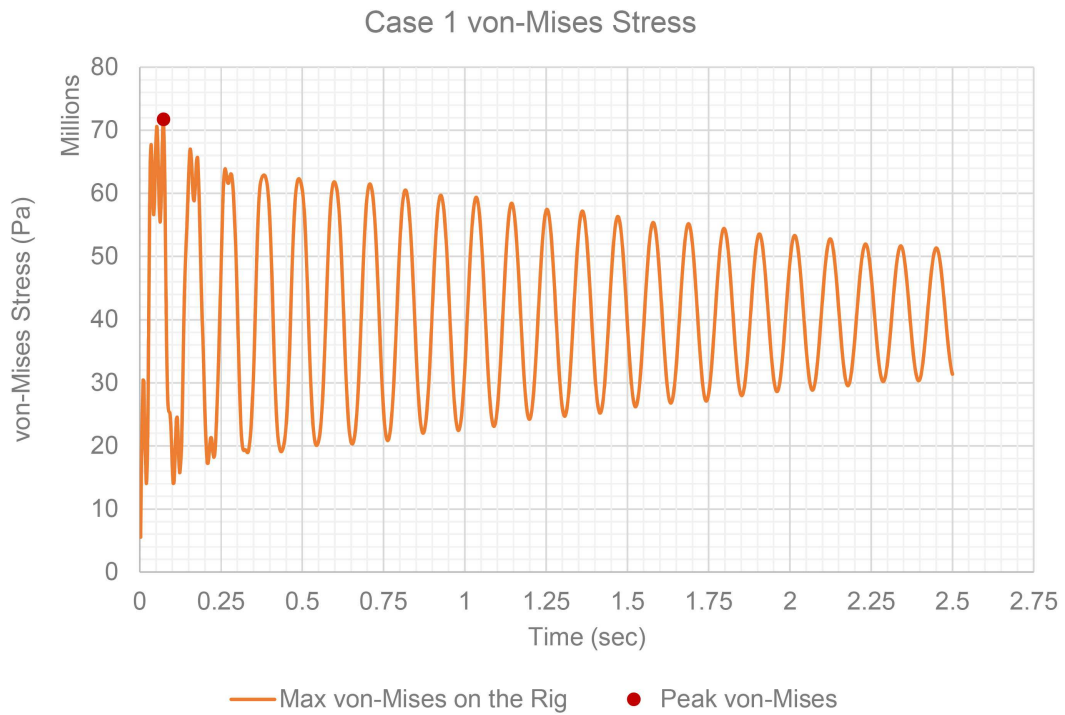
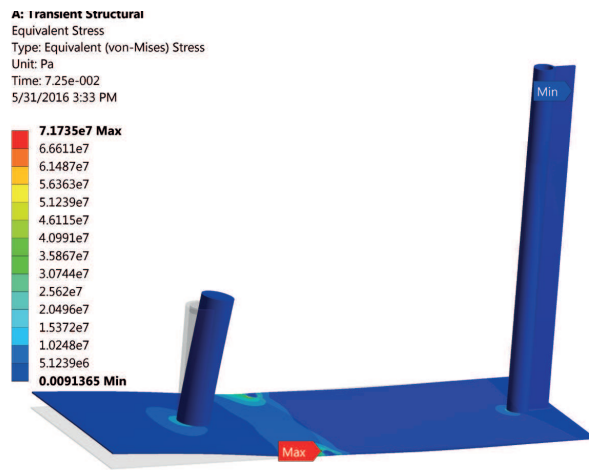


Figure 4.10: Case 1 cylinder directional deformations vs. force coefficients over time

The von-Mises stress occurring on the experimental rig due to the hydrodynamic forces and cylinder deformations can be seen in Figure 4.11a. The von-Mises stress reaches its peak value of 71.74 MPa at 0.0725 s. It can be seen in Figure 4.11 b that the minimum von-Mises stress occurs on the fixing portion of the main support with a value of 0 Pa. On the other hand, the maximum stress occurs in the vicinity of the front cylindrical support with a value of 71.74 MPa. These supports were introduced as a fixed support to the system. Deformations were scaled up 170 times for visibility purposes.



(a) Case 1 maximum von-Mises stress over time



(b) Case 1 peak von-Mises stress

Figure 4.11: Case 1 von-Mises stress on the rig

### 4.2.3 Case 2

Since Case 2 was also solved using one-way coupled FSI simulation for the cylinder, the non-dimensional force coefficients and the Strouhal number are identical to that of Case 1 and the base case. Figure 4.12 demonstrates the directional deformations on the x and y axes of the cylinder for Case 2 along with the drag and lift force coefficients over time.

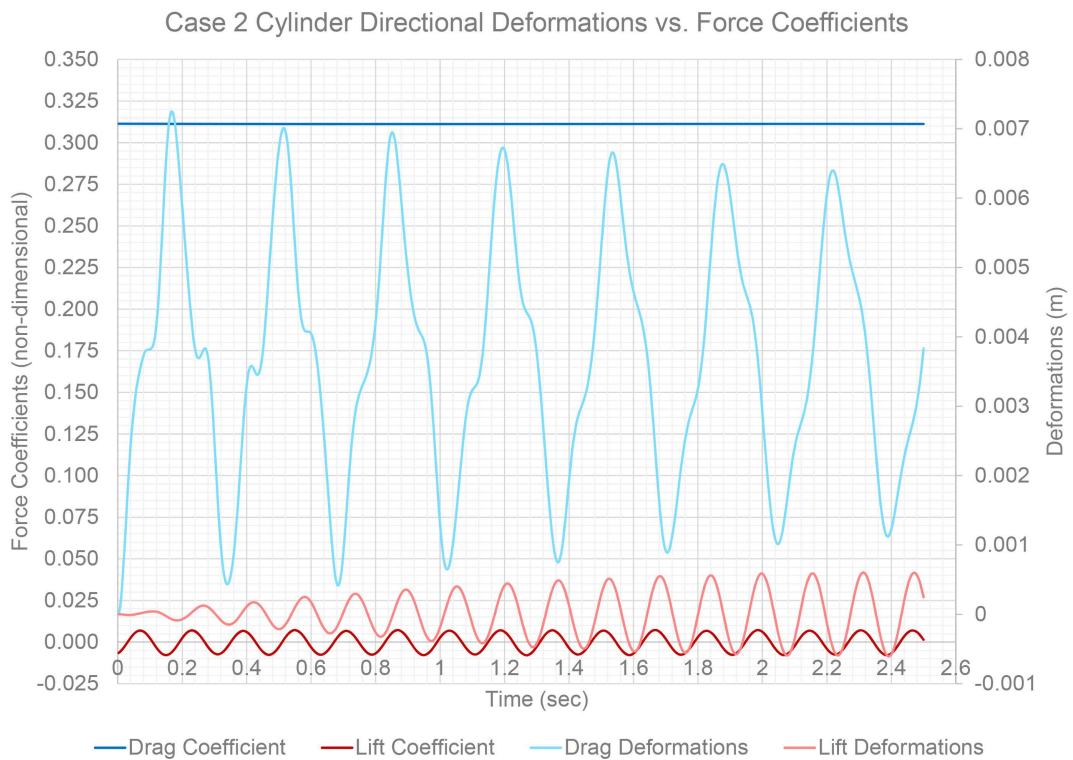
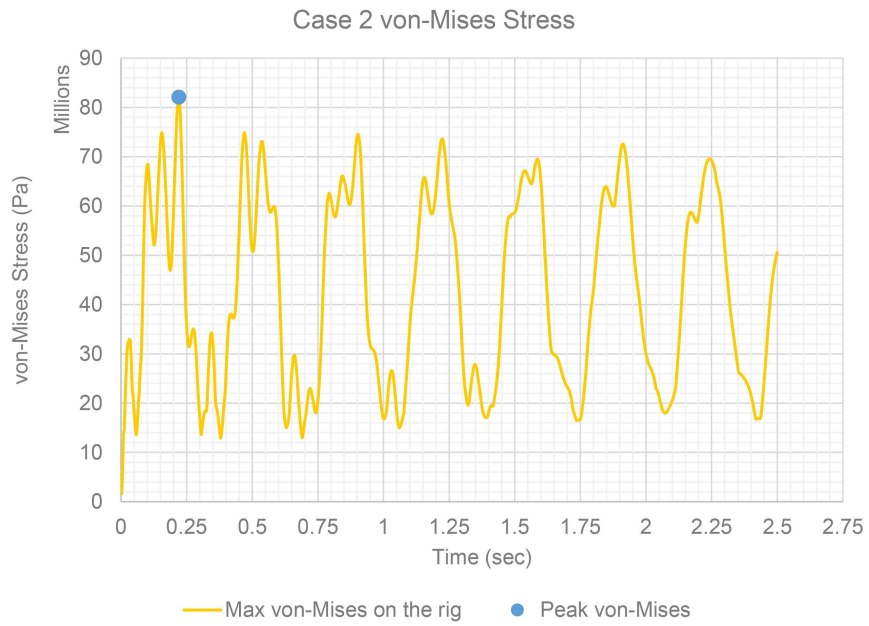
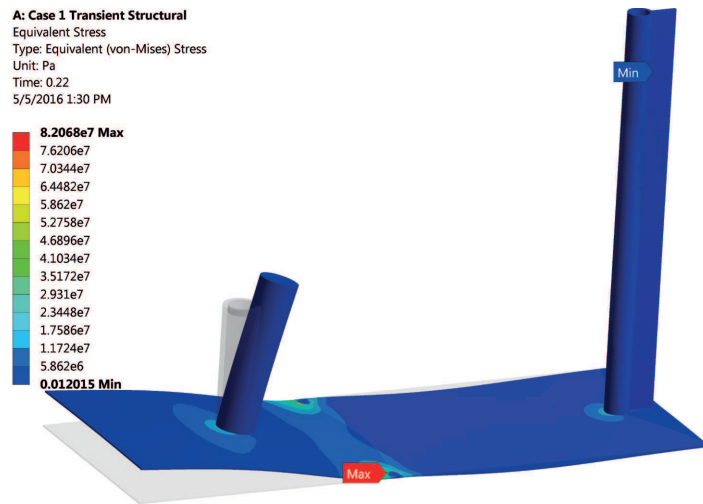


Figure 4.12: Case 2 cylinder directional deformations vs. force coefficients over time

Figure 4.13 a represents the behavior of the maximum von-Mises stress for Case 2. The highest stress occurs at 0.22 s with a value of 82 MPa. The deformations and the stress distributions on the rig were shown in Figure 4.13 b.



(a) Case 2 maximum von-Mises stress over time



(b) Case 2 peak von-Mises stress

Figure 4.13: Case 2 von-Mises stress on the rig

Deformations were scaled up 33 times for visibility purposes.

### 4.2.4 Case 3

The biggest difference between one-way and two-way coupling is the update of the fluid domain based on the structural deformations. In a different manner than the first three cases, Case 3 and Case 4 were solved by two-way coupling. Thus the hydrodynamic forces around the cylinder were affected by the cylinder deformations resulting in a different behaviour. Non-dimensional hydrodynamic forces for the flexible cylinder can be seen over time in Figure 4.14.

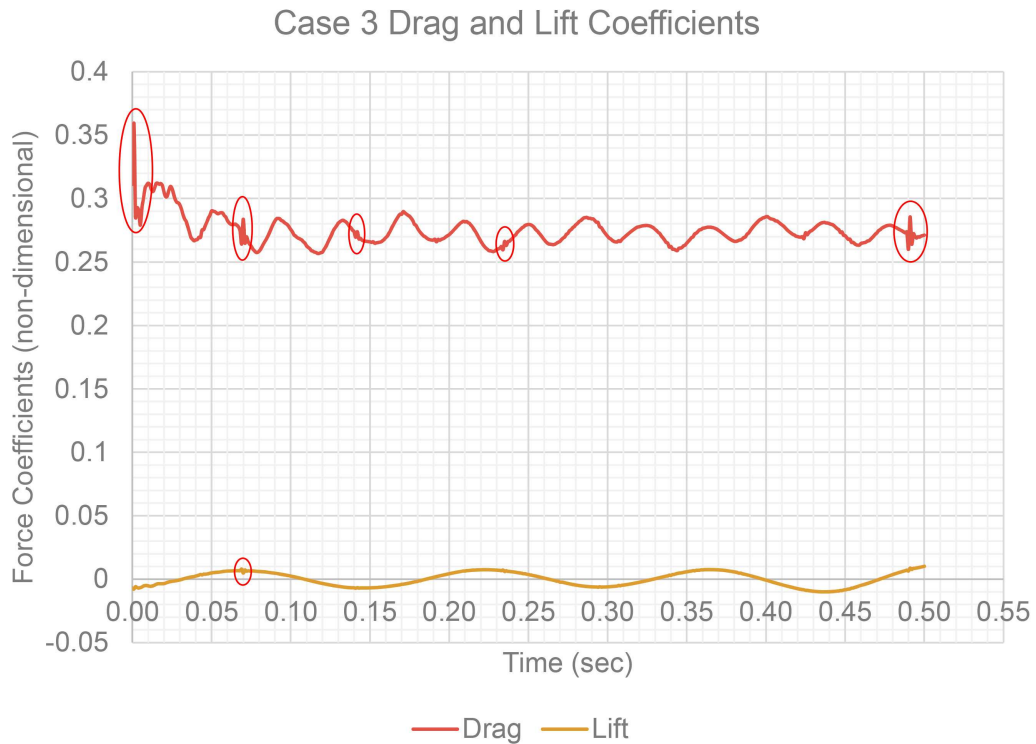


Figure 4.14: Case 3 lift and drag coefficients over time

Red circles in the figure mark the perturbations in the force coefficients. These perturbations are thought to be caused by the lack of force transfer convergence for

certain time steps. It was seen from the coupling log file that force monitoring showed that the force transfer was not converging to the RMS convergence target even though both of the solvers were reaching convergence individually. Regardless, the trend of the drag and lift coefficient can be clearly seen.

Figure 4.15 shows the directional deformations of the cylinder in x and y axes over time.

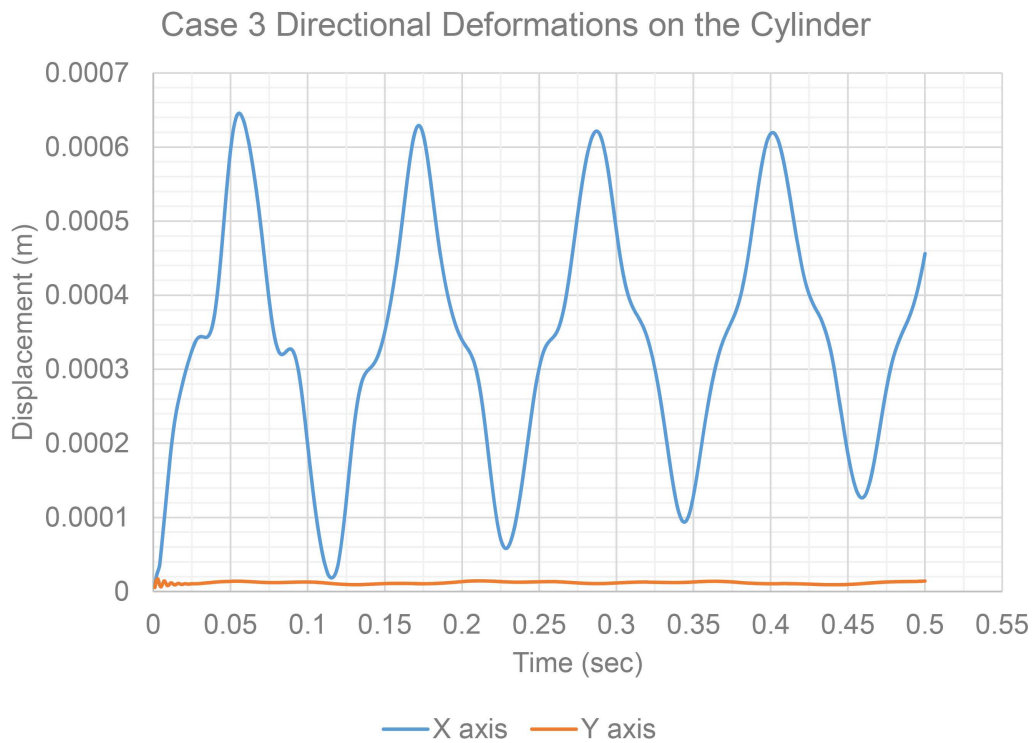


Figure 4.15: Case 3 directional deformations of cylinder on X and Y axes

Figure 4.16 illustrates the directional deformations on the cylinder for Case 3 along with the force coefficients over time. Lift deformations were magnified 10 times in order to emphasize the relation between the lift force and structural reactions.

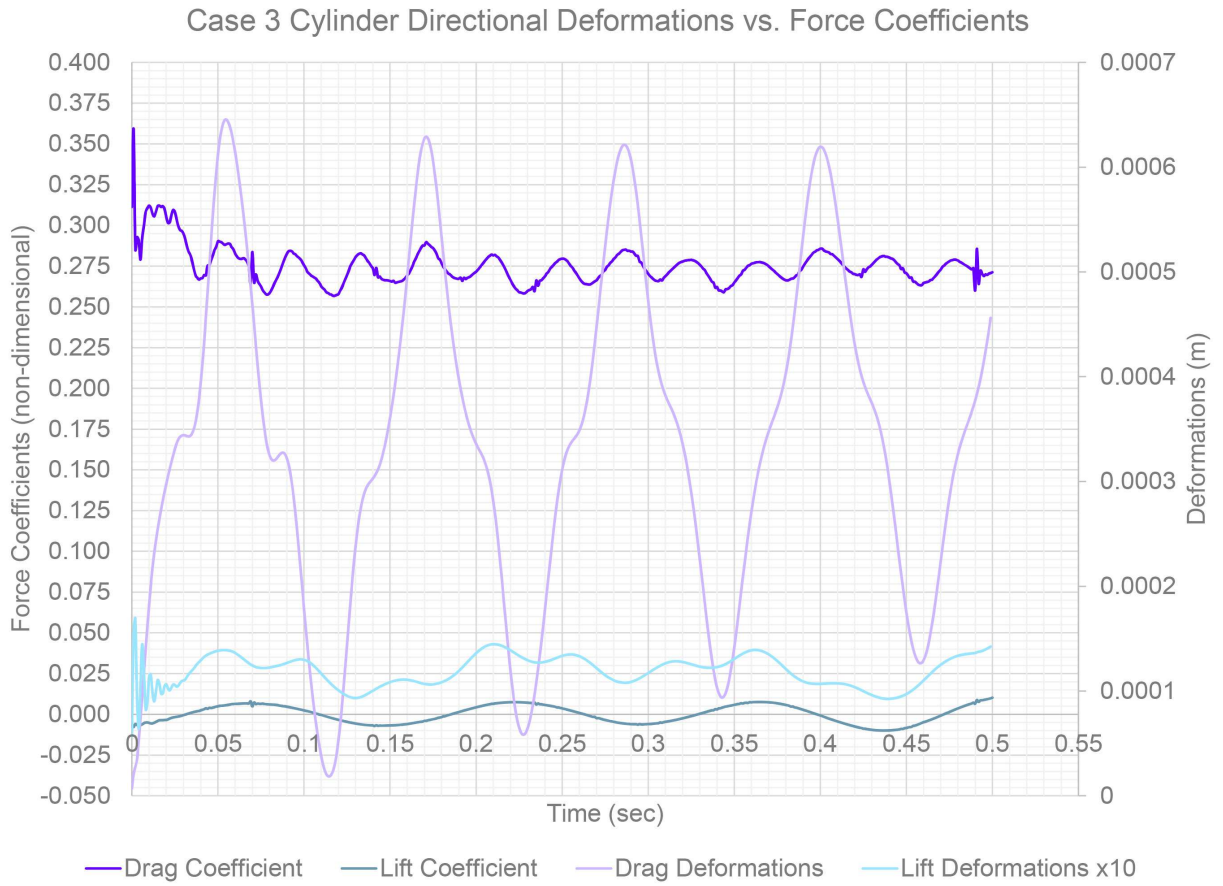
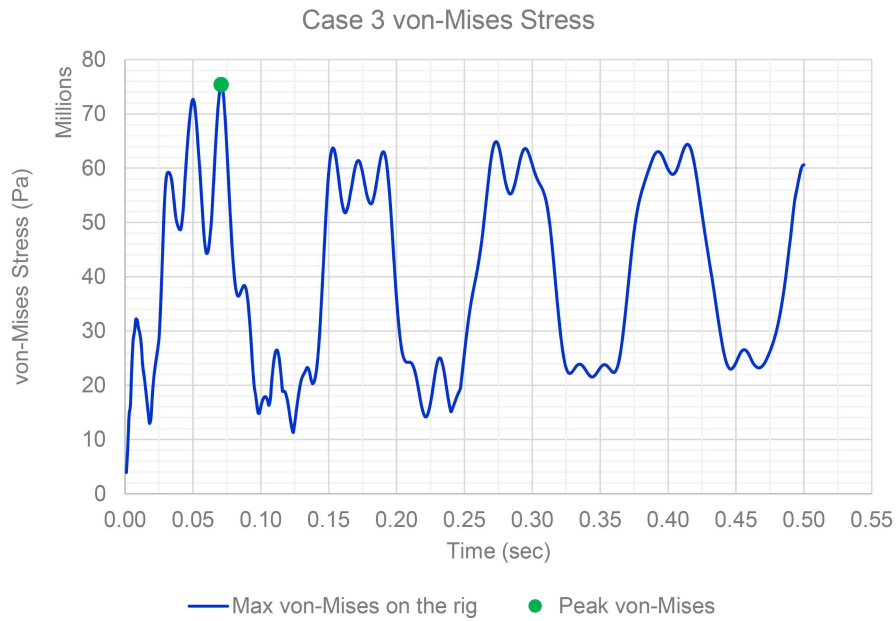
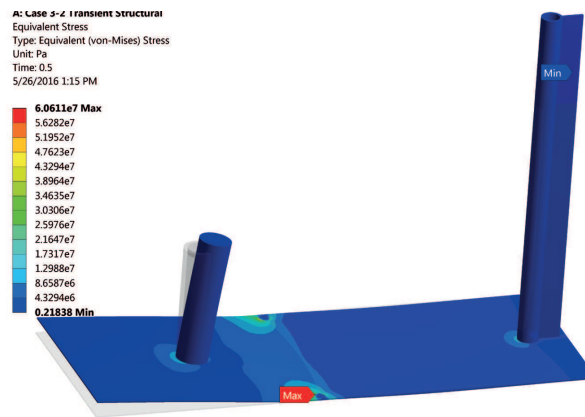


Figure 4.16: Case 3 cylinder directional deformations vs. force coefficients over time

Figure 4.17 a demonstrates the maximum von-Mises stress values for Case 3 at the highest point, which is at 0.071 s with a value of 75.39 MPa. Figure 4.17 b illustrates the stress distribution and deformations on the rig at the highest maximum von-Mises stress time.



(a) Case 3 maximum von-Mises stress over time



(b) Case 3 peak von-Mises Stress

Figure 4.17: Case 3 von-Mises stress on the rig

For visibility purposes deformations were magnified 160 times.

### 4.2.5 Case 4

The non-dimensional lift and drag coefficients of the hydrodynamic forces acting on the cylinder are illustrated in Figure 4.18.



Figure 4.18: Case 4 lift and drag coefficients over time

Similar to Case 3, red circles in the figure mark the perturbations in the force coefficients. These perturbations are thought to be due to the unconverged data transfer for force variables within certain coupling time steps. The RMS convergence target for these data transfers was set to 0.01. However, the trend of the drag and lift coefficients can clearly be seen.

Figure 4.19 demonstrates the directional deformations of the cylinder in the x and

y axes due to the lift and drag forces.

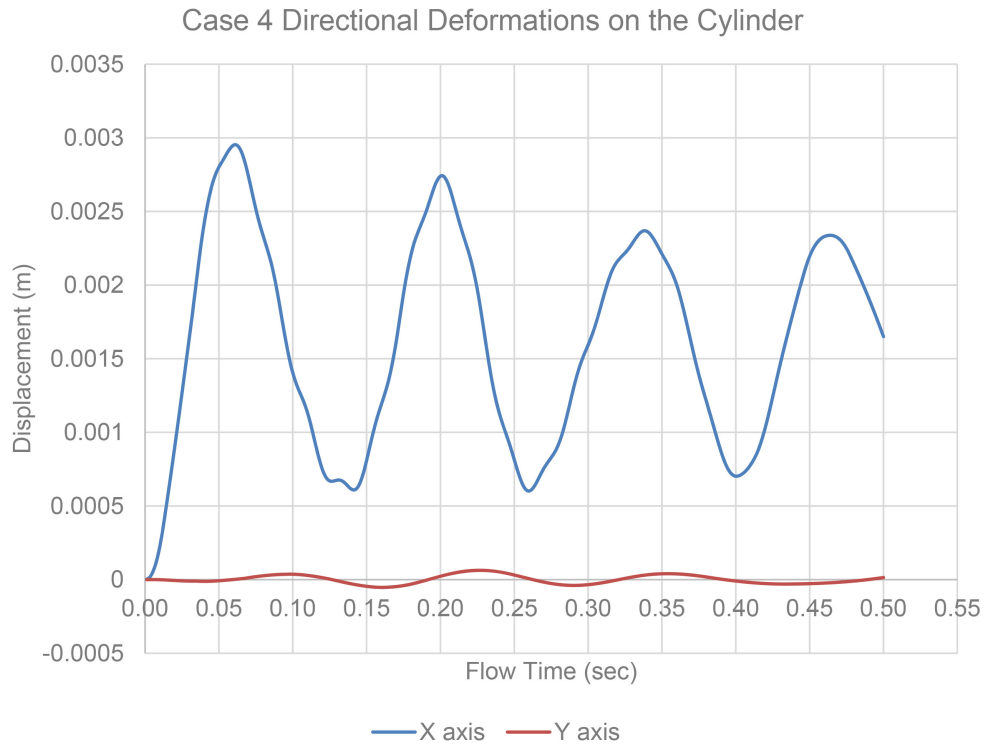


Figure 4.19: Case 4 directional deformations of cylinder on X and Y axes

Figure 4.20 demonstrates directional deformations on the cylinder for Case 4 along with the force coefficients over time.

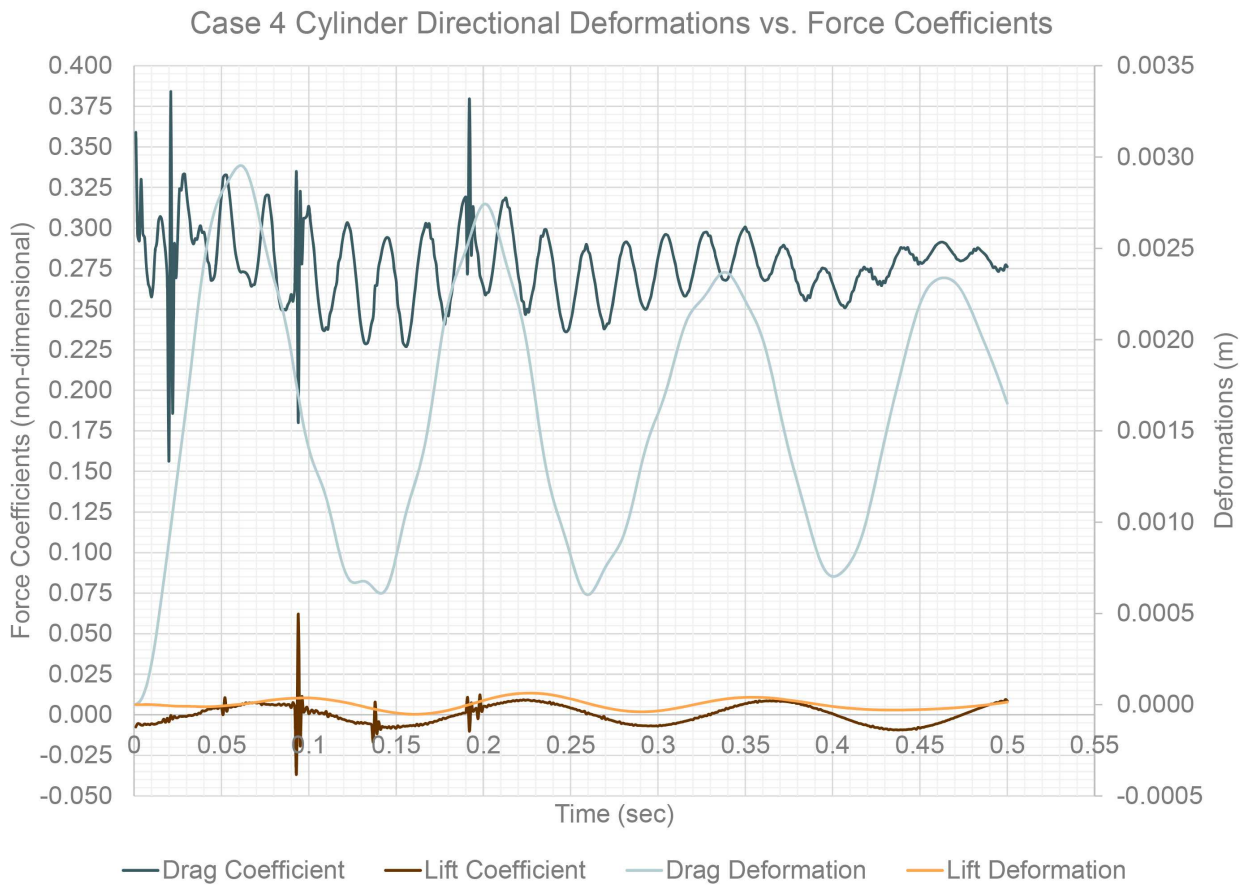
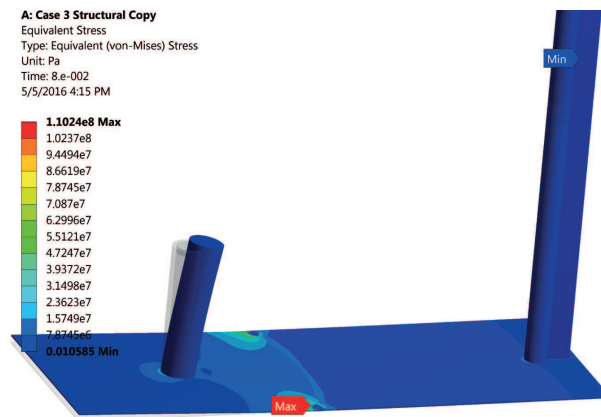


Figure 4.20: Case 4 cylinder directional deformations vs. force coefficients over time

Figure 4.21 a demonstrates the oscillation of the maximum von-Mises stress for Case 4 over time. The highest stress occurs at 0.08 s with a value of 110.24 MPa. Figure 4.21 b illustrates the stress concentrations and resulting deformations on the system. Similar to other cases, the highest stress occurs on the plate around the front support connections.



(a) Case 4 maximum von-Mises stress over time



(b) Case 4 peak von-Mises Stress

Figure 4.21: Case 4 von-Mises stress on the rig

In the Figure 4.21 b, deformations were scaled up 33 times for visibility purposes. It was seen that the highest von-Mises stress that occurs on the system was measured in Case 4 with a value of 110.24 MPa. This value does not exceed the tensile yield strength of 250 MPa for the structural steel material [48] thus it can be concluded that the experimental rig is nowhere close to yield.

### **4.3 Comparison of the Cases**

In order to determine the differences between one-way and two-way coupling methodologies, hydrodynamic forces and the structural responses of the cylinder were investigated by comparing the directional deformations with one-way and two-way coupling. Furthermore, to examine the endurance of the experimental rig for the proposed experimental conditions, the highest deformations and von-Mises stress distributions on the experimental rig were investigated.

#### **4.3.1 Comparison of Hydrodynamic Cylinder Forces and Structural Responses**

Figure 4.22 illustrates the calculated oscillation of the drag coefficients for one-way cases and the two-way coupled Case 3. It can be seen that larger oscillations of the drag force are observed with the update of the fluid domain with the structural deformations. Figure 4.23 depicts the calculation of directional deformations caused by the drag coefficients for one-way and two-way coupled FSI simulations. Two-way coupling appears to calculate a smaller oscillation magnitude compared to one-way coupling. However, both calculations follow a similar trend.

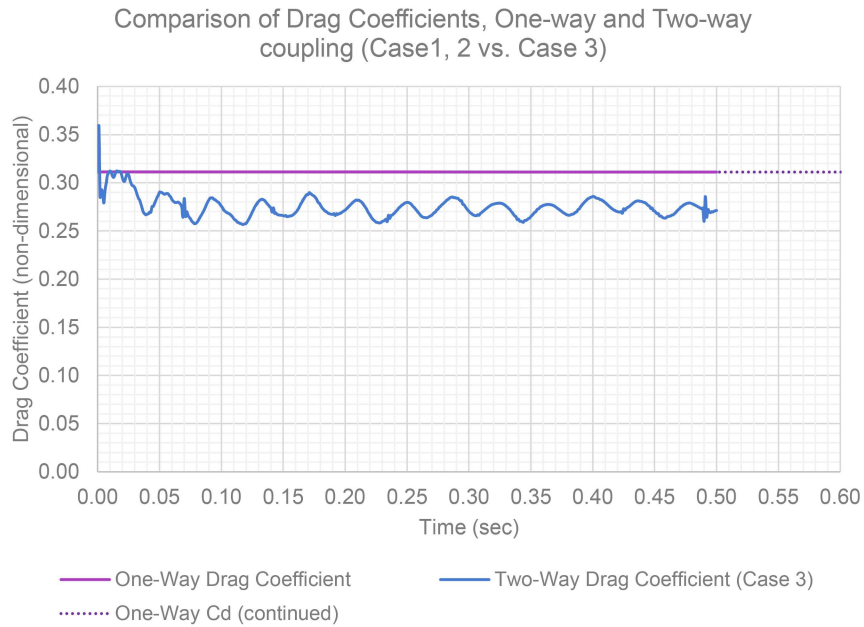


Figure 4.22: Comparison of drag coefficients for one-way (Case 1, 2) and two-way (Case 3) cases

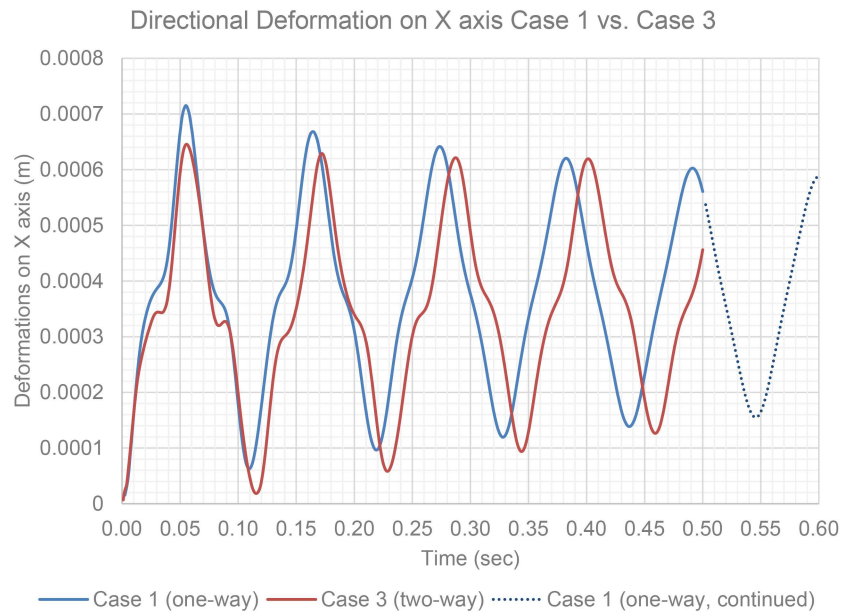


Figure 4.23: Comparison of one-way and two-way directional deformations along x axis

Figure 4.24 presents the drag coefficient calculation with one-way coupling for Case 1 and Case 2 and two-way coupling for Case 4. Similar to that of Case 3, it can be seen that when the fluid domain is updated with the cylinder deformations, bigger oscillations of the drag force are observed.

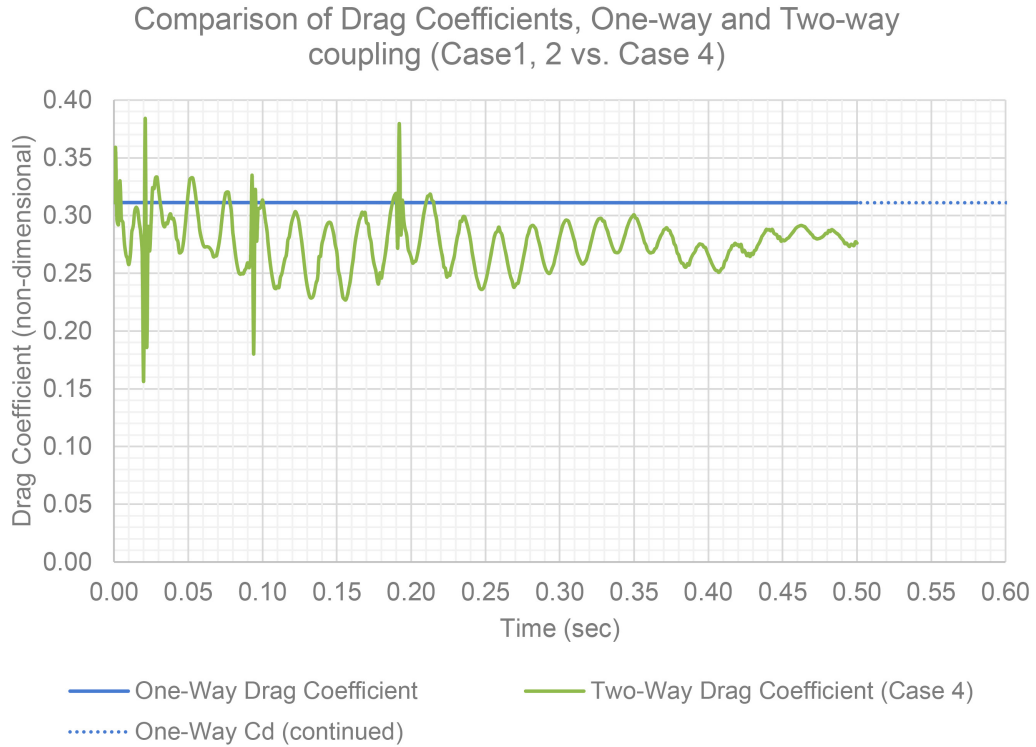


Figure 4.24: Comparison of drag coefficients for one-way (Case 1, 2) and two-way (Case 4) cases

Figure 4.25 demonstrates the directional deformations along x axis for one-way coupled Case 2 and two-way coupled Case 4.

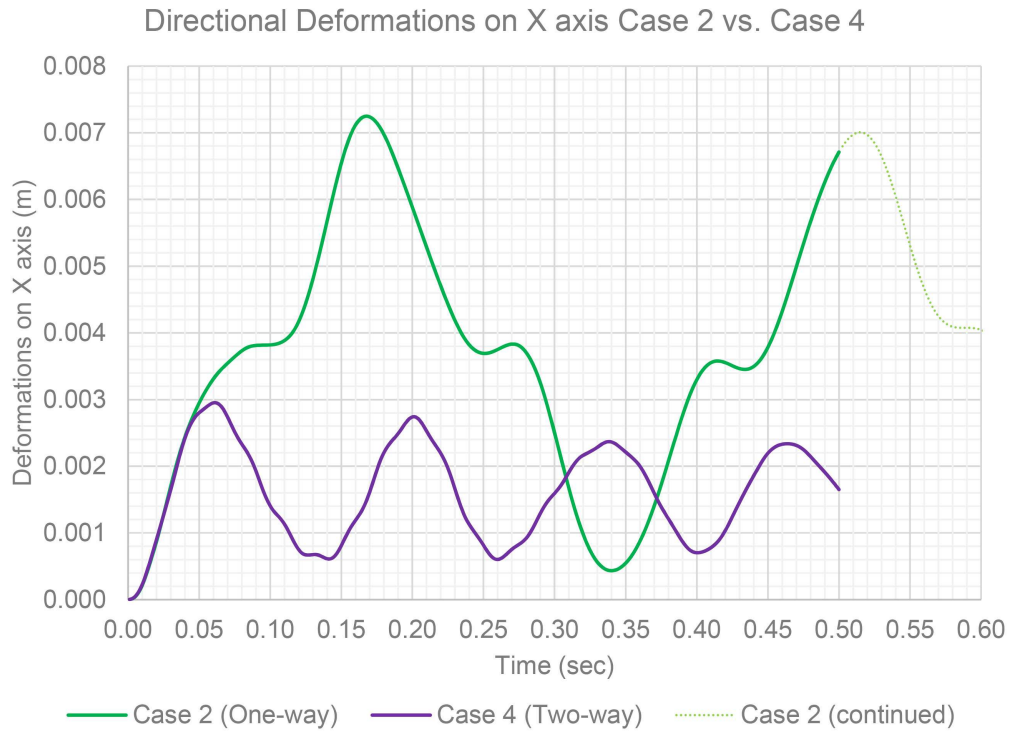


Figure 4.25: Comparison of one-way and two-way directional deformations along x axis

Figure 4.26 depicts the calculation of the drag coefficient over time for all FSI cases. It can be seen that the oscillations for drag coefficient are bigger in the two-way coupled FSI solutions. Moreover, it seems that a more flexible material causes bigger oscillations in the drag force as seen in Case 4. For further analysis, perturbations were removed from the drag and lift coefficient by omitting the values from the coupling steps with unconverged data transfers between the solvers. The further analysis of the drag coefficient signal on Figure 4.26 reveals that even though the linear trend line of the drag calculation for all cases might seem similar, the standard deviation, mean and root mean square values show significant differences. For instance, when

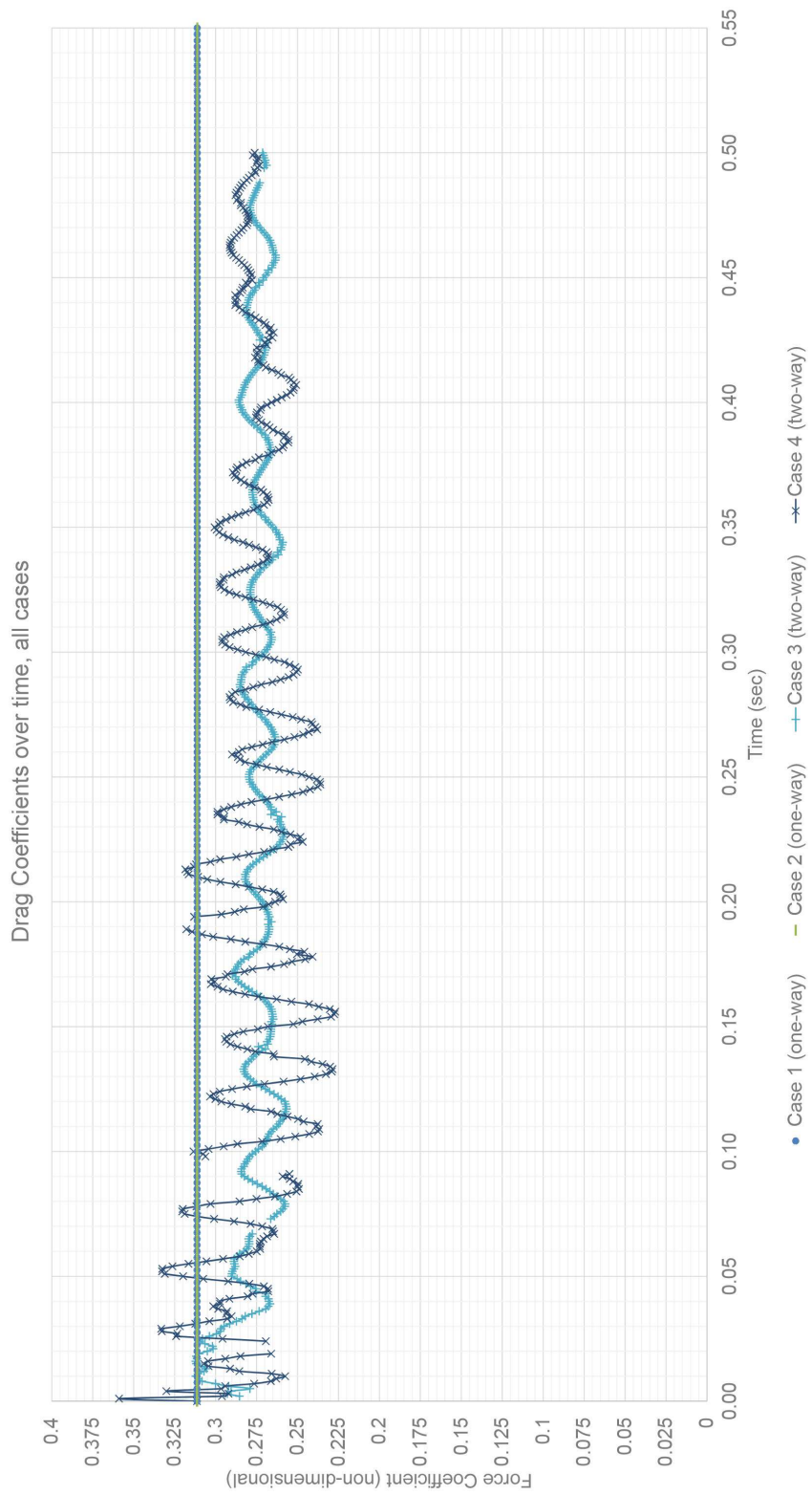


Figure 4.26: Comparison of drag coefficients for all cases

the mean value for calculated drag data for Case 1 and 2 are approximately 0.311, the value is close to 0.275 for Case 3 and 4. In addition, standard deviation is 0 for Case 1 and 2, however, it is 0.0106 and 0.0207 for Case 3 and 4 respectively. These results show that two-way coupled FSI analysis predicts the effect of structural responses and their effects on the hydrodynamic forces more successfully than the one-way coupled approach.

Figure 4.27 demonstrates the calculation of lift coefficients for flexible cylinder with one-way and two-way coupled FSI simulations.

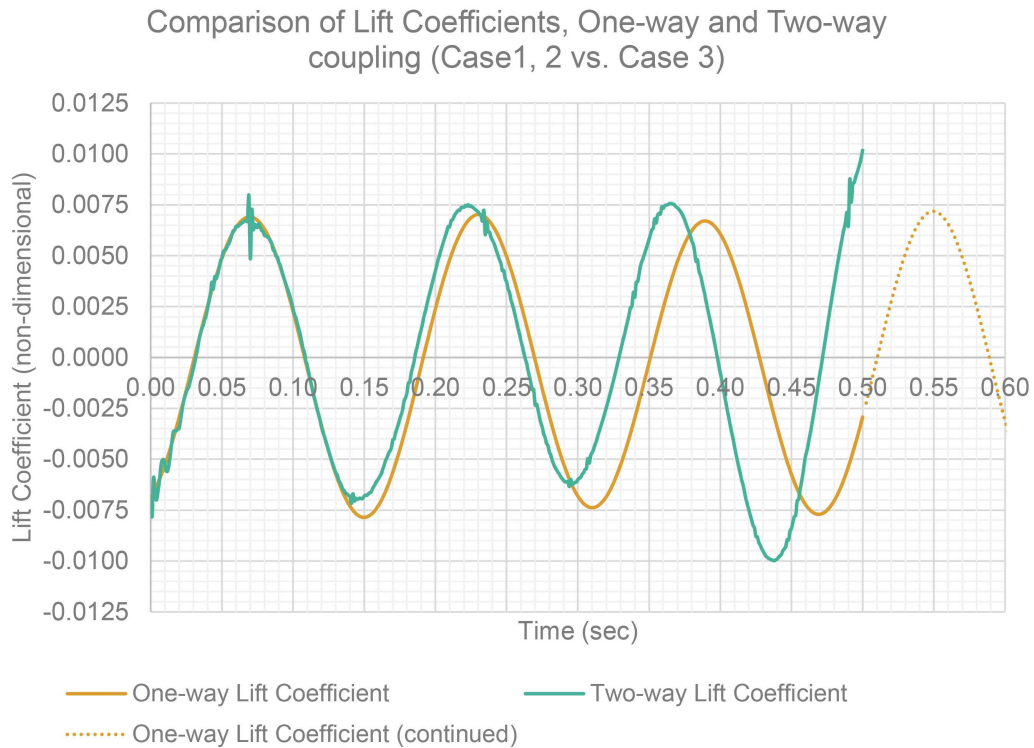


Figure 4.27: Comparison of lift coefficients for one-way (Case 1, 2) and two-way coupling (Case 3) cases

Figure 4.28 demonstrates the solution of directional deformations on the flexible

cylinder along y axis with one-way and two-way coupling.

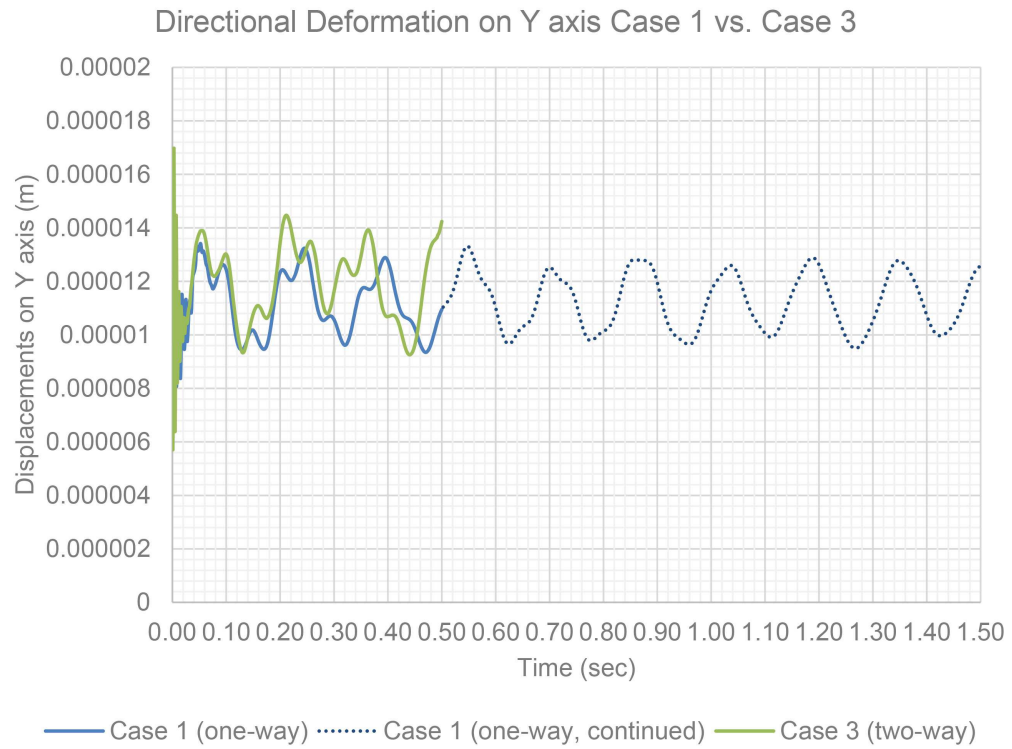


Figure 4.28: Comparison of one-way and two-way directional deformations along y axis

Figure 4.29 demonstrates the calculation of lift coefficients for more flexible cylinder with one-way and two-way coupled FSI simulations.

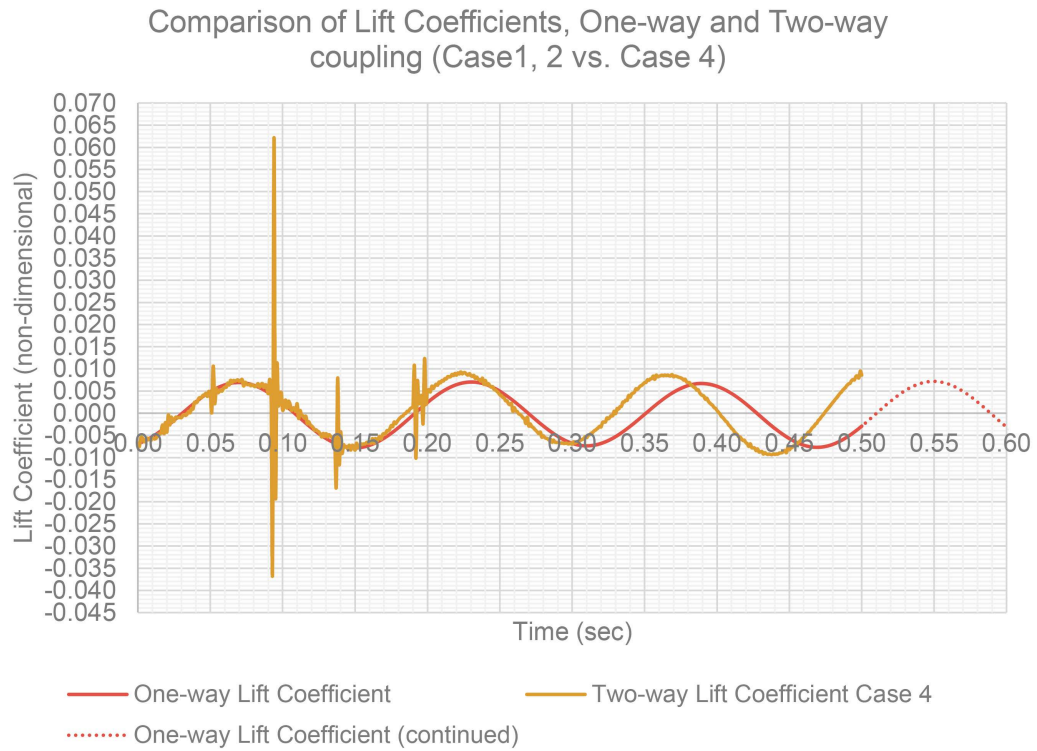


Figure 4.29: Comparison of lift coefficients for one-way (Case 1, 2) and two-way (Case 4) cases

Figure 4.30 demonstrates the solution of directional deformations on the more flexible cylinder on the y axis for one-way and two-way coupling.

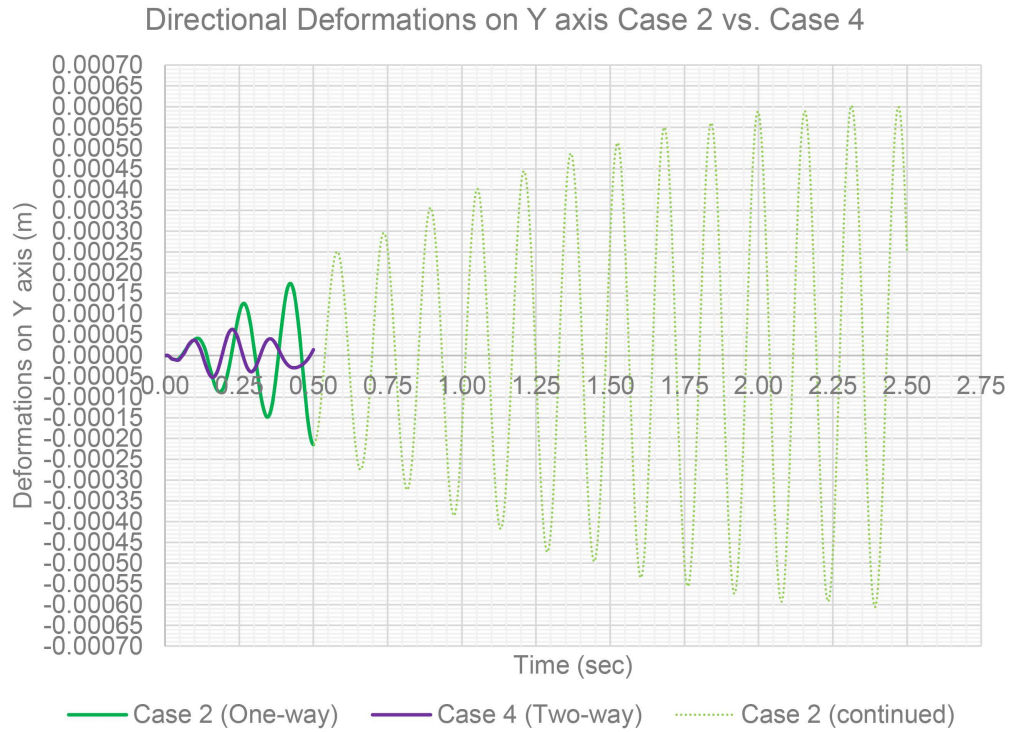


Figure 4.30: Comparison of one-way and two-way directional deformations along y axis

Furthermore, Figure 4.31 illustrates the calculation of the lift coefficient over time for all FSI cases. Perturbations were removed from the lift coefficient by omitting the values from the coupling steps with unconverged data transfers between the solvers. Perturbation filtered data for all cases was shown in Figure 4.31. It can be seen that bigger oscillations for the lift coefficient were calculated with two-way coupled FSI solutions. Thus, the effect of flexibility on the lift force seems to be calculated more successfully with two-way coupled FSI analysis. It is evident that the structural responses of a more flexible cylinder cause bigger oscillations in the lift force as seen

in Cases 3 and 4. The mean values of the oscillating lift forces are similar, however, with further investigation it can be seen that the standard deviation varies between coupling methods. For one-way coupled FSI cases the standard deviation is 0.0052, whereas it is 0.0053 for Case 3 and 0.0057 for Case 4. Similarly, when the RMS value for the lift coefficient is calculated as 0.0052 for one-way coupled cases, it was calculated as 0.0072 for two-way coupled cases. The results clearly show that the structural behavior of flexible structures and the resultant effect of their structural response on hydrodynamic forces is more successfully analyzed with two-way coupled FSI analysis.

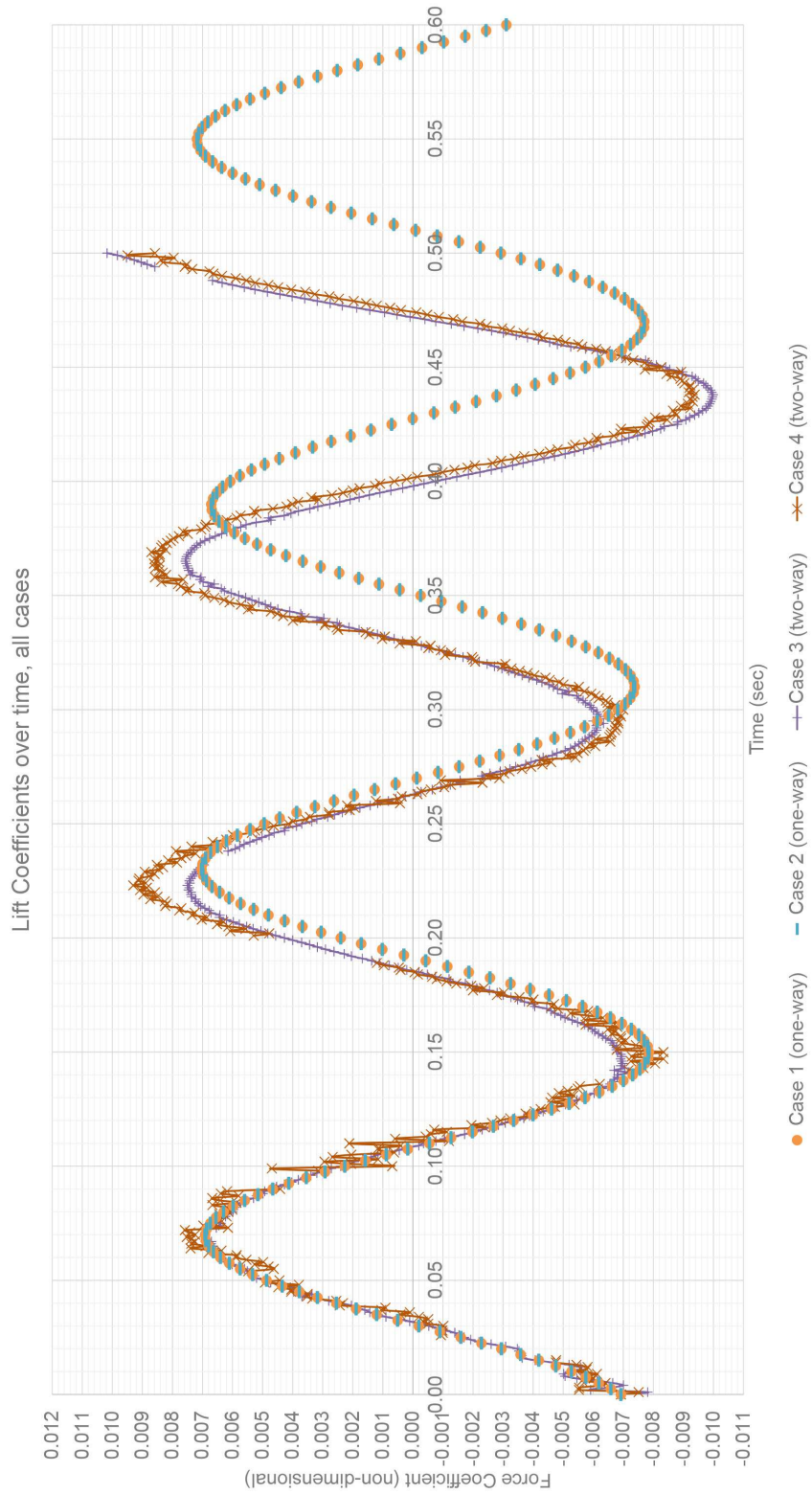


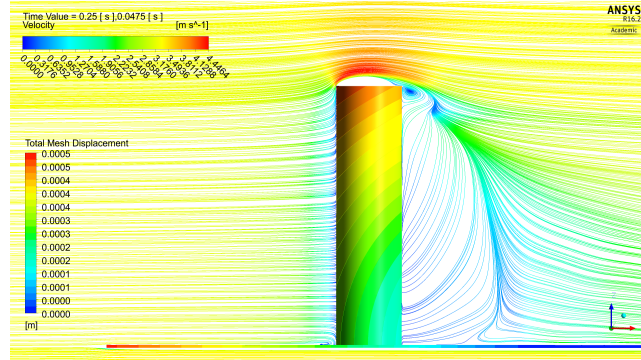
Figure 4.31: Comparison of lift coefficients for all cases

## Total Cylinder Deformations

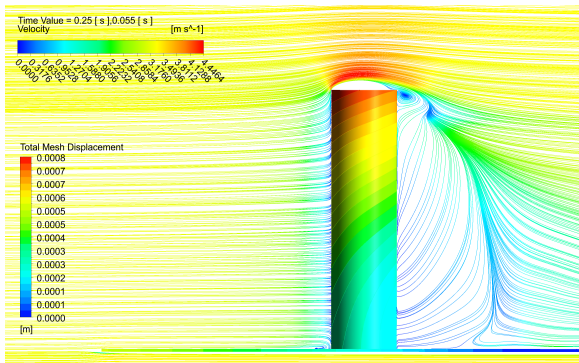
Figures 4.32 and 4.33 below demonstrate the close-up figures of true scale deformations of cylinders mounted on the experimental rig. The flow velocity is visualized with the aid of streamlines and presented at the nearest available solution time for the highest structural deformation time. Deformations along the x axis are represented with a colored scheme on the cylinder body. The highest deformations along with response/diameter ratio of the cylinders are summarized in Table 4.2. From this table it can be seen that a one-way coupled FSI solution overestimates the deformations of the flexible cylinder compared two-way coupling.

Table 4.2: Highest deformations of the cylinder

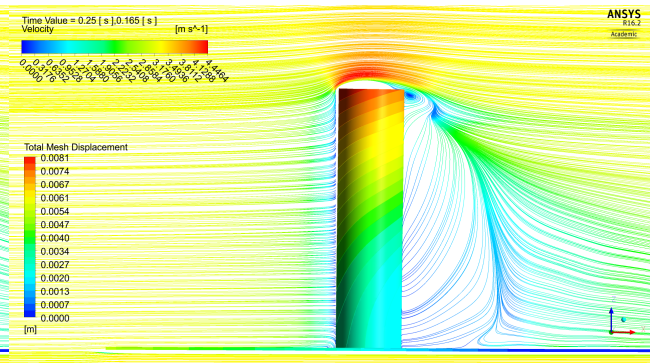
| Case      | Deformation (m) | Diameter/Response (non-dimensional) | Time (s) |
|-----------|-----------------|-------------------------------------|----------|
| Base case | 0.0005          | 297.05                              | 0.0475   |
| Case 1    | 0.0008          | 190.30                              | 0.055    |
| Case 2    | 0.0081          | 18.84                               | 0.165    |
| Case 3    | 0.0007          | 212.16                              | 0.054    |
| Case 4    | 0.0031          | 49.71                               | 0.0610   |



(a) Case 0

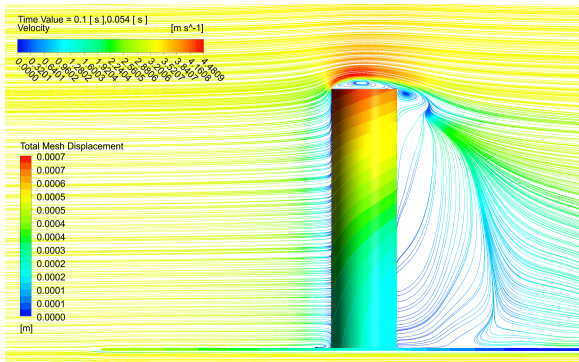


(b) Case 1

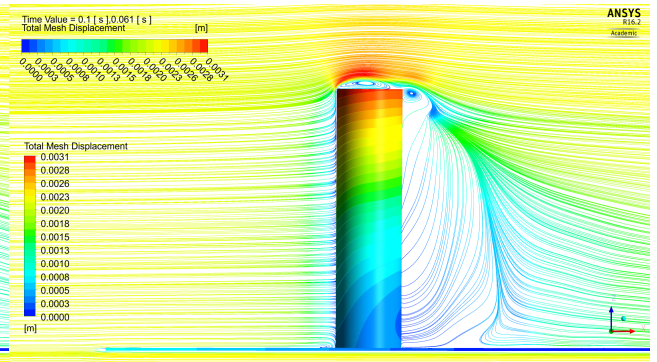


(c) Case 2

Figure 4.32: Deformations of the cylinder solved with one-way coupling



(a) Case 3



(b) Case 4

Figure 4.33: Deformations of the cylinder solved with two-way coupling

### 4.3.1.1 Comparison of the Rig Endurance Calculation

In order to investigate the endurance of the experimental rig for the given operating conditions of the proposed experiments, the total deformations and von-Mises stress distributions were examined. Figure 4.34 illustrates the behavior of the maximum total deformation for each case over the rig over time. The results were summarized in Table 4.3. It can also be seen from the following figures that the max total deformations occur in the leading front edge of the plate.

Table 4.3: Highest deformations on the rig (plate)

| Case      | Deformation (m) | Time   | Scale |
|-----------|-----------------|--------|-------|
| Base case | 0.00062         | 0.055  | 130   |
| Case 1    | 0.00064         | 0.0625 | 120   |
| Case 2    | 0.00678         | 0.1875 | 110   |
| Case 3    | 0.00061         | 0.061  | 130   |
| Case 4    | 0.00113         | 0.071  | 110   |

Figures 4.35 and 4.36 depict the magnified maximum deformations on the experimental rig at their highest deformation times with different FSI coupling approaches and varying material properties for the cylinder. For visibility purposes and to provide an easier comparison between cases, the deformations were magnified by a similar scaling as further explained in Table 4.3.

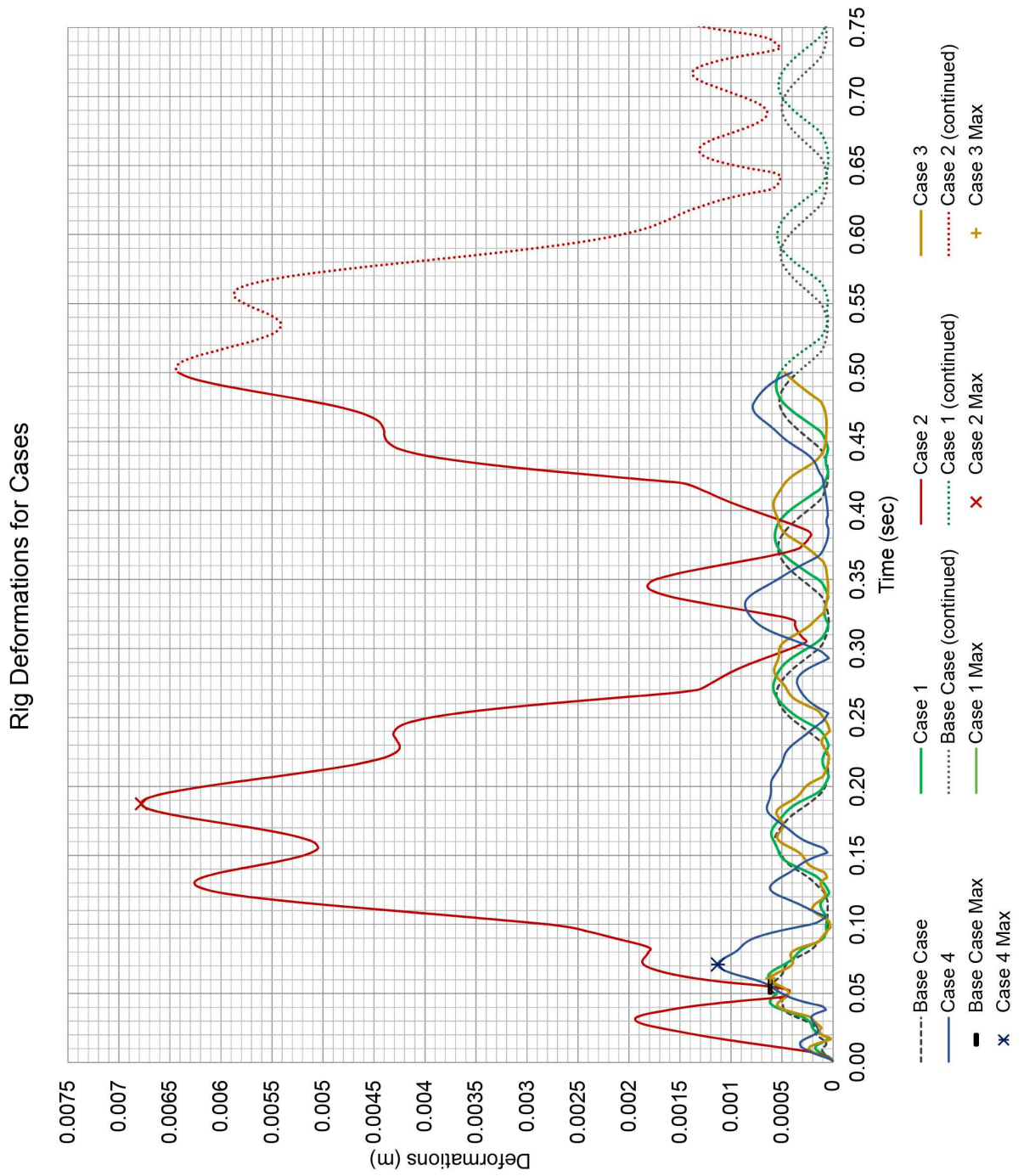
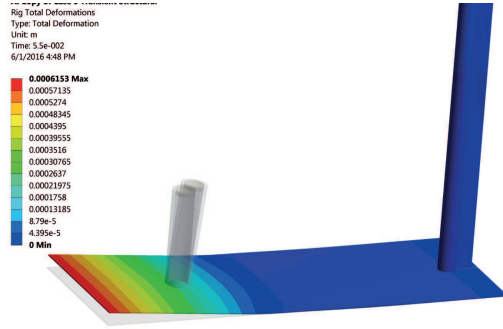
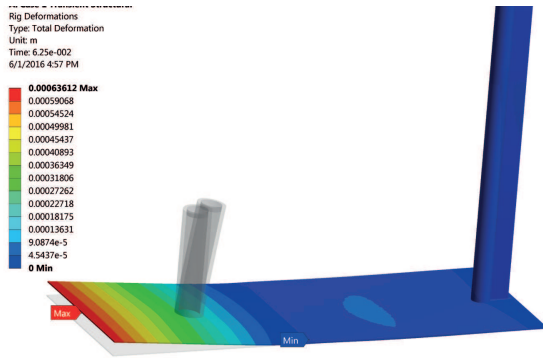


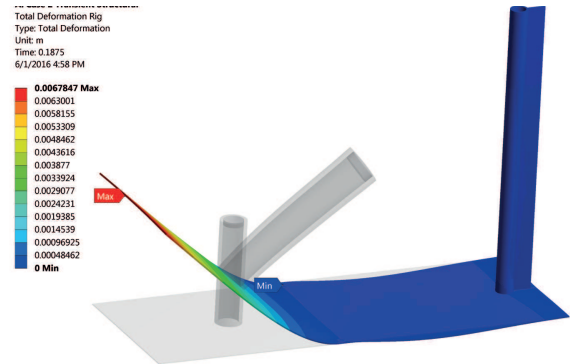
Figure 4.34: Deformations of rig for all cases



(a) Base case, Case 0

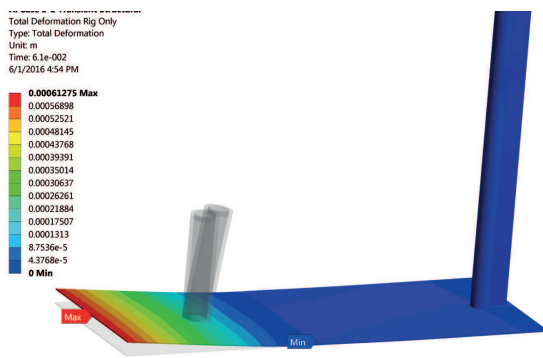


(b) Case 1

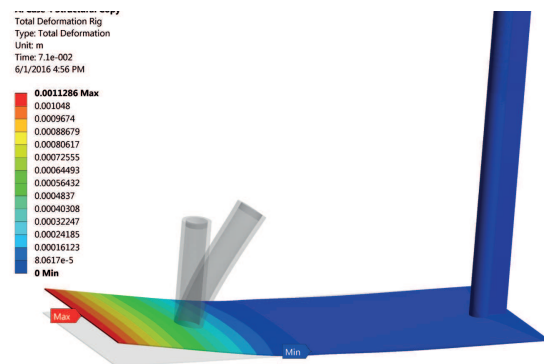


(c) Case 2

Figure 4.35: Maximum deformation on the rig for one-way coupling



(a) Case 3



(b) Case 4

Figure 4.36: Maximum deformation on the rig for two-way coupling

For the purpose of providing an overall insight of the flow around the experimental rig and the structural responses following figures are presented. In the figures below, structural responses along with the results of the nearest available solution time for fluid flow are shown together. All figures depict the von-Mises stresses on the rig when the highest deformations occur.

Figure 4.37 represents the structural results for case 1 at 0.55 s along with the flow velocity and streamlines in the vertical plane and flow pressure with the aid of vortex core visualization. For the fluid flow results, the nearest available data solution at 0.25 s was used. A horizontal plane separating the geometry into two symmetrical parts was used in order to demonstrate the local flow features.

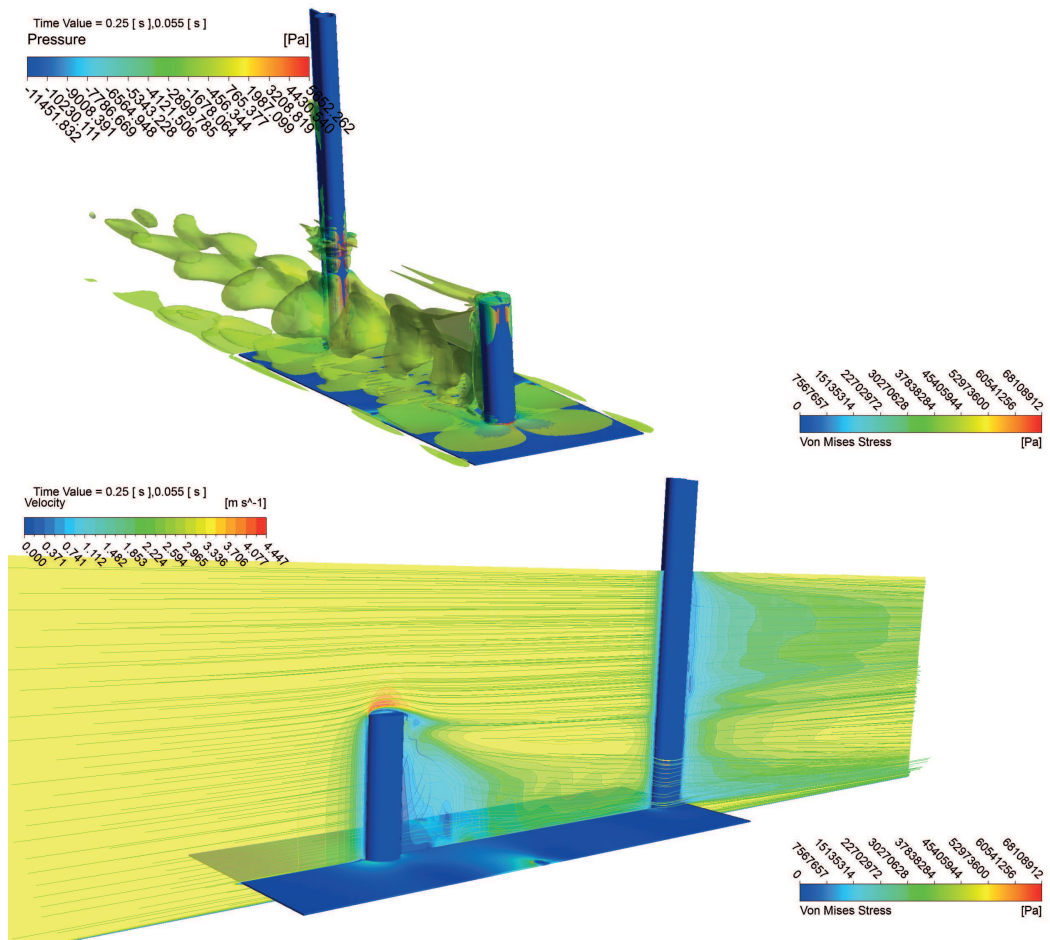


Figure 4.37: Case 1 FSI von-Mises vs. flow velocity and pressure at highest deformation

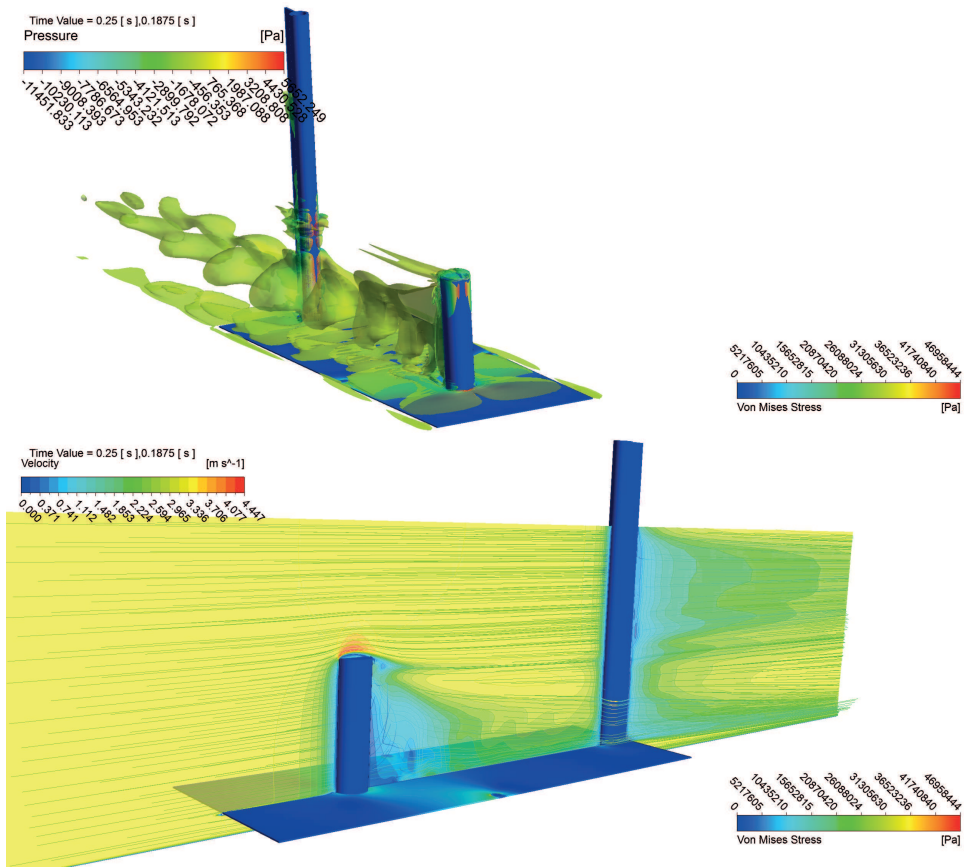


Figure 4.38: Case 2 FSI von-Mises vs flow velocity and pressure at highest deformation

Figure 4.38 represents the results from the highest deformation time, at 0.1875 s, and shows the similar variables in Case 2 with the only difference being the structural time.

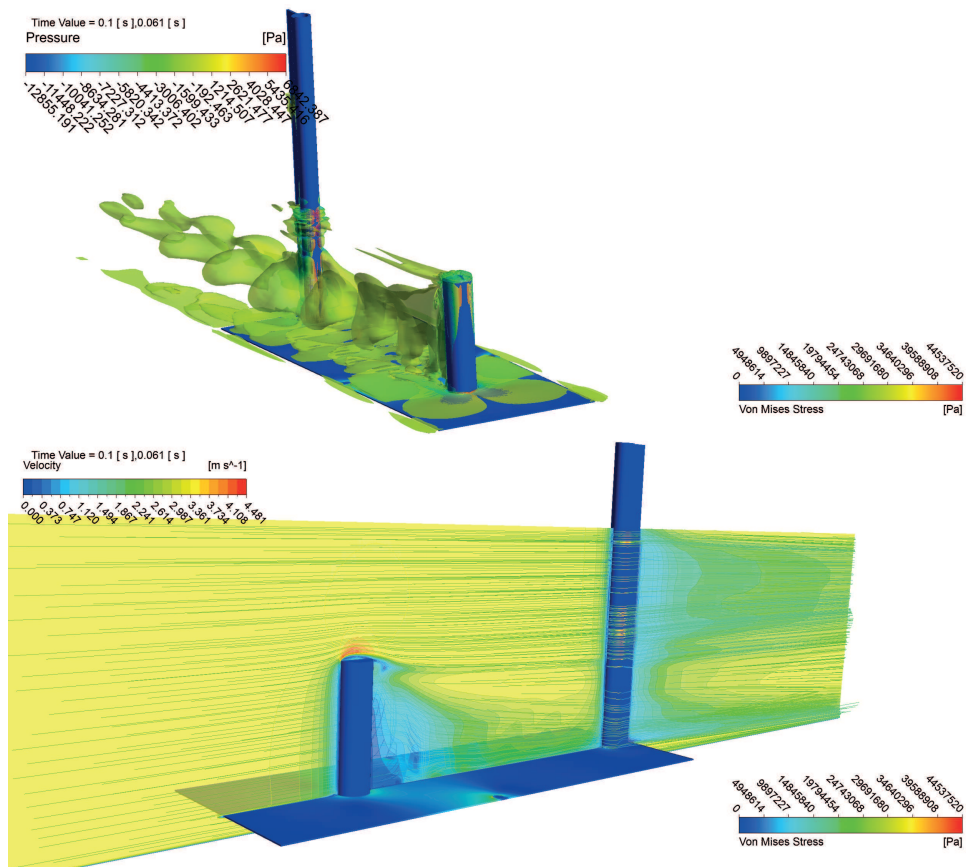


Figure 4.39: Case 3 FSI von-Mises vs. flow velocity and pressure at highest deformation

Figure 4.39 shows the results for Case 3 at 0.061 s structural solution and 0.1 s solution for fluid flow.

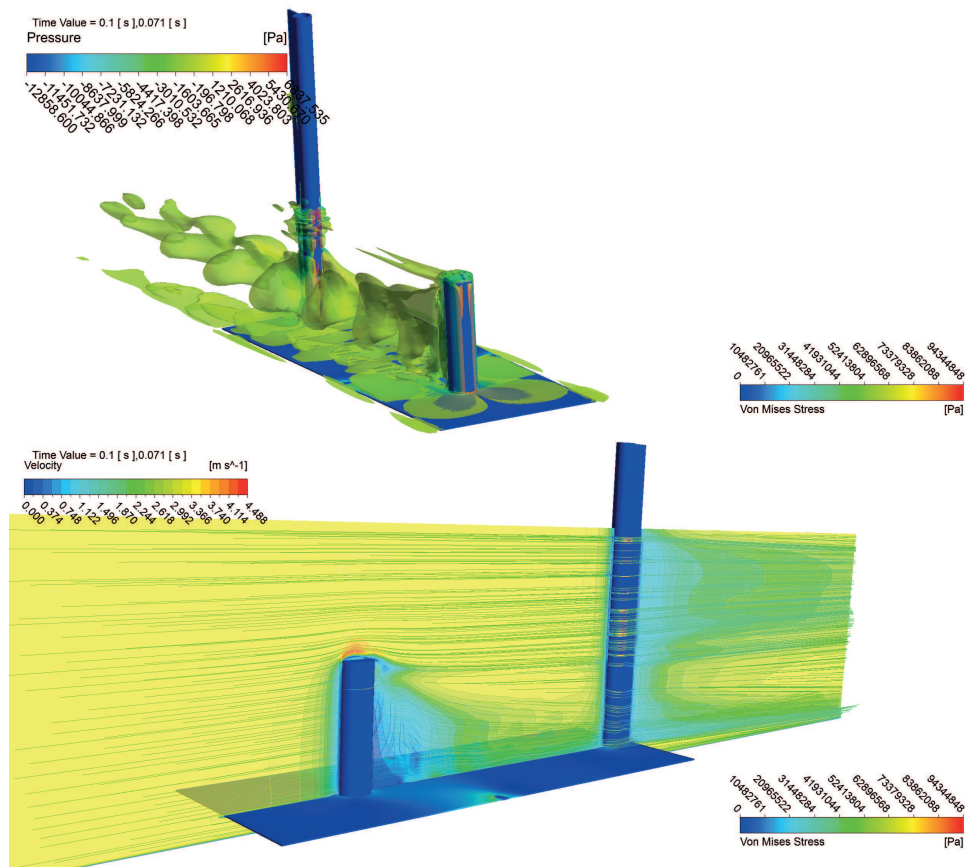
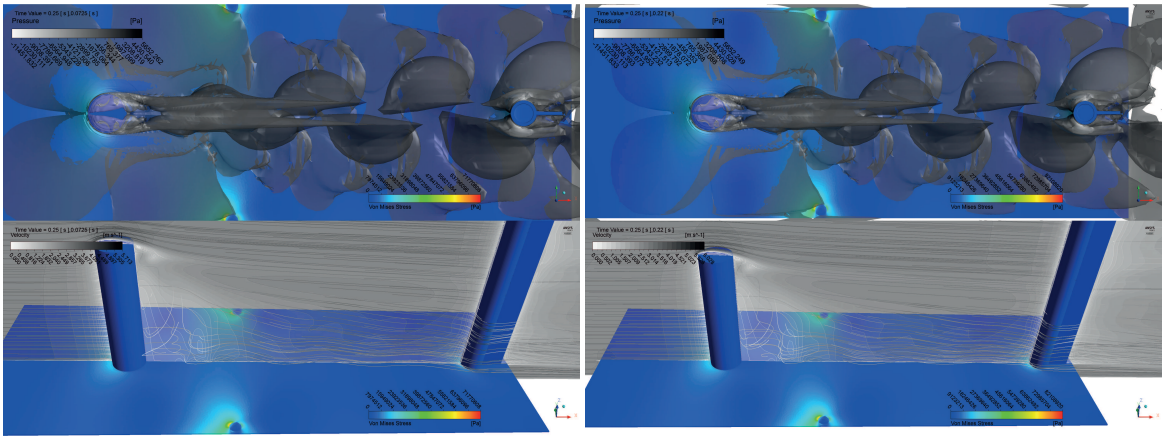


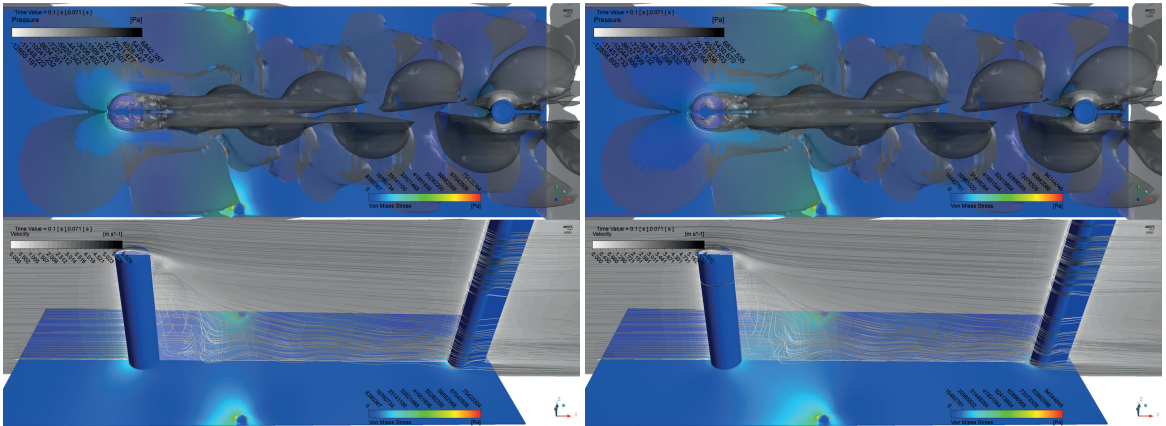
Figure 4.40: Case 4 FSI von-Mises vs. flow velocity and pressure at highest deformation

In Figure 4.40, the 0.071 s solution for structural and 0.1 s solution for fluid flow results are illustrated. Figure 4.41 illustrates the von-Mises stress concentrations on the experimental rig from a top view. The flow features are represented with the aid of a vortex core visualization and streamlines on the horizontal plane with a black and white color scheme. The stress distribution is presented with a color scheme for better visibility.



(a) Case 1

(b) Case 2



(c) Case 3

(d) Case 4

Figure 4.41: Maximum von-Mises stress on rig for all cases

## 4.4 Summary

As mentioned earlier, cylindrical structures are subject to flow-induced forces in offshore environments and the investigation of these forces is vital for their design. The hydrodynamic forces that affect the cylinder causes deformations on the structures that conversely affect the hydrodynamic forces and create a cyclic relation between the fluid and structure. This relation and its effect on structural responses and endurance can only be numerically solved with the aid of an FSI investigation. Considering this, the main objective of the presented work was to develop a numerical model and method that simulates the dynamic reactions of a scale model of a deeply submerged cylindrical flexible offshore structure mounted on a supporting measurement rig, which will be used for future experimental studies.

As a part of the developed FSI tool, the fluid flow model which solves the flow features and hydrodynamic forces around the cylinder is in good agreement with other studies. By investigating the rare combination of a cylinder with a height to diameter ratio of 4 and a flow in critical regime with a Reynolds number of approximately 500 000, this work makes a modest contribution to the ongoing discussion on the numerical modelling of flow past a three-dimensional finite cylinder.

Due to the necessity for dynamic meshing, significantly more effort was required for the set-up of the two-way coupled model. The differences between one-way and two-way coupling are the additional steps for modelling the CFD domain according to dynamic meshing, setting the re-meshing parameters as mentioned in Chapter 3 and creating the additional data transfer in system coupling module for deformations. It was also observed that the run times for two-way coupled simulations are significantly

longer than one-way coupled simulations due to the requirements for smaller time-step sizes and additional coupling iterations.

It has been found from the results that both FSI models (one-way and two-way coupled) are capable of solving the structural responses of flexible finite cylinders with varying material properties. However, despite the extra effort for modelling and significantly longer solution time, it was observed that for more realistic results and applications involving a flexible cylinder, a two-way coupled approach is required due to the non-negligible effects of structural deformations on the hydrodynamic forces and cyclic FSI effects.

In addition, it was shown by the numerical model that the designed experimental rig provides a reliable and stable system with relatively low stresses, minimum vibrations and adequate structural stiffness for future experiments which would include fluid force measurements around the submerged flexible cylinder.

Furthermore, the presented FSI model predicts the deformations and stress distributions on the experimental rig and provides a significant insight about stability and endurance. Thus, it can be used as a guide for possible structural improvements on the experimental rig against loads that might occur under experimental operating conditions.

# Chapter 5

## Conclusion and Recommendations

### 5.1 Conclusion

The focus of the study was to establish a numerical model and method for simulating the deformations and dynamic reactions of a scale model of a deeply submerged cylindrical flexible offshore structure mounted on a supporting measurement rig that will be used for future experimental studies. Moreover, the focus of the study also included the examination of the endurance of the experimental rig at a prescribed depth and speed along with the effects of the flexibility of the cylinder on hydrodynamic loading conditions.

For this purpose, a turbulent flow in critical regime past a circular cylinder attached to an experimental rig was investigated. Structural response and hydrodynamic loading results were presented with one-way and two-way coupled FSI analysis involving a single phase turbulent flow around the experimental rig and cylinder.

Based on the results, it is possible to conclude that the research has been very

successful. The findings of the research and the results generated in the numerical simulations are quite convincing, and thus the following conclusions can be drawn. It was seen from the numerical investigation and data from the literature that hydrodynamic loads show a difference for cylinders with small length to diameter ratios and free tips (finite cylinders) compared to infinite cylinders with no free tips. For instance, drag and lift forces are smaller than those of the infinite cylinders for finite cylinders with small aspect ratios. In addition, the Strouhal number for lift oscillations also seems to be smaller for finite cylinders. However, although the hydrodynamic loads are smaller for finite cylinders, the inherent mutual dependence between the structure and hydrodynamic loading of flexible cylinders still carries a significant relation which requires investigation. The numerical flow simulation was shown to be able to capture these three-dimensional effects and provide a model that better reflects the true flow around the cylinder as modeled. For the examination of this cyclic relation and its effect on both structural responses and hydrodynamic loads, both one-way and two-way coupled partitioned fluid-structure interaction methods were used. It was seen from the results that the one-way coupled partitioned approach overestimates the structural responses. However, the two-way coupled FSI approach solves the structural deformations more accurately and provides more realistic structural behaviour predictions by including the resulting effects on the hydrodynamic loads and vice versa. Thus, it is concluded that a fully coupled two-way simulation offers sufficient improvement in the prediction of flow induced vibrations and structural stresses to justify the extra effort in modeling and the extra time required to run the simulations.

Summing up the results, it can be concluded that from the presented comparison of the proposed partitioned one-way and two-way coupled FSI methods, the superiority

of the two-way coupled approach when investigating the FSI of a flexible cylinder was proven. Furthermore, the developed numerical tool can be used to evaluate the structural performance of the designed experimental rig for further validation experiments.

## 5.2 Recommendations

More research into the understanding of aspect ratio, free end and structural flexibility effects on the hydrodynamic loads of cylinders is necessary. In order to provide a solid insight about these factors, further research will clearly be required to validate with experiments. Considering this, the focus of the study was broadened to provide a reliable design for the experimental rig that can be used for future experiments. The proposed numerical model can be readily used in practice for the FSI of a fully submerged flexible circular cylinder and the endurance of the experimental rig. However, with minor modifications, the focus of interest can be expanded by including more experiments with different material properties for the cylinder.

Moreover, the effects of depth and free surface on the FSI of the flexible cylinder can be studied by changing the operational depth of the experimental rig. In this case, owing to the advantages of a partitioned coupled FSI approach, the developed FSI tool can be improved correspondingly with a multiphase fluid flow model using the volume of fraction (VOF) method which would provide a chance to examine free surface effects numerically.

In addition, the fluid flow model can be replaced with a LES, DES or another RANS turbulence model when a different approach is needed for turbulence modelling.

This type of modification requires minor changes on the developed model. Similarly, improvements can be made by using other structural modules within ANSYS for the structural part of the problem. To decrease the run times, computers with more processors and faster storage can be used. However, it is worthwhile to note that for the structural solver of this FSI problem, the use of 16 cores provides the most efficient solution performance.

Considering the advantages, the developed numerical tool has great potential for designing applications to be used in oil and gas industry such as oil spill containments. For this purpose, the experimental study may include the investigation of the structural behaviour of flexible cylinder when internally pressurized. Correspondingly, the FE model within the FSI model can be modified.

More tests and experiments will be needed to verify the limits of the developed tool such as including flow with higher Reynolds numbers and cylinders with more flexibility.

In conclusion, further research into the FSI of flexible cylinders with a wider variety of material properties and scenarios is desirable to extend our knowledge of their performance and potential use in harsh offshore environments within oil and gas industry.

# Bibliography

- [1] J. L. Heseltine. Flow Around a Circular Cylinder with a Free End. MS Thesis, University of Saskatchewan, Saskatoon, Saskatchewan, Canada, August 2003.
- [2] T. Kawamura, M. Hiwada, T. Hibino, I. Mabuchi, and M. Kumada. Flow around a finite circular cylinder on a flat plate (cylinder height greater than turbulent boundary layer thickness). *Bulletin of JSME*, 27:232–814, 1984.
- [3] ANSYS, Canonsburg. *Fluent User’s Guide*, release 15 edition, 2013. See also URL <http://www.ansys.com>.
- [4] ANSYS, Canonsburg. *Fluent Theory Guide*, release 15 edition, 2013. See also URL <http://www.ansys.com>.
- [5] Michael Schafer Hans-Joachim Bungartz, editor. *Fluid-Structure Interaction Modelling, Simulation, Optimisation*, page V. Springer-Verlag Berlin Cambridge University Press, Heidelberg, 2006.
- [6] B. Mutlu Sumer and Jorgen Fredsoe. *Hydrodynamics Around Cylindrical Structures (Revised Edition)*. World Scientific Publishing Co. Pte. Ltd., 2006.

- [7] M. M. Zdravkovich. *Flow Around Circular Cylinder, Volume 1: Fundamentals*. Oxford University Press, 1997.
- [8] O. Reynolds. An experimental investigation of the circumstances which determine whether the motion of water shall be direct or sinus, and of the law resistance in parallel channels. In *Proceedings of the Royal Society of London*, pages 84–99, January 1883.
- [9] M. S. Bloor. The transition to turbulence in the wake of a circular cylinder. *Journal of Fluid Mechanics*, 9:290–304, 1964.
- [10] T. Okamoto and M. Yagita. The experimental investigation on the flow past a circular cylinder of finite length placed normal to the plane surface in a uniform stream. *Bulletin of JSME*, 16(853560), 1973.
- [11] S.C. Luo. Flow past a finite length circular cylinder. *Proceedings of the Third International Offshore and Polar Engineering Conference*, III(853560), 1993.
- [12] C. Norberg. Fluctuating lift on a circular cylinder: review and new measurements. *Journal of Fluids and Structures*, 17:57–96, 2003.
- [13] A. Roshko. Experiments on the flow past a circular cylinder at very high reynolds number. *Journal of Fluid Mechanics*, 10:345–356, 1961.
- [14] P. W. Bearman. On vortex shedding from a circular cylinder in the critical reynolds number rgime. *Journal of Fluid Mechanics*, 37:577–585, 1969.
- [15] E. Achenbach and E. Heinecke. On vortex shedding from smooth and rough

- cylinders in the range of reynolds number  $6 \times 10^3$  to  $5 \times 10^6$ . *Journal of Fluid Mechanics*, 109:239–251, 1981.
- [16] N. K. Delany and N. E. Sorensen. Low-Speed Drag of Cylinders of Various Shapes. Technical Note 3038, National Advisory Committee for Aeronautics, 1953.
- [17] G. Schewe. On the force fluctuations acting on a circular cylinder in crossflow from subcritical up to transcritical reynolds numbers. *Journal of Fluids and Structures*, 133:265–285, 1983.
- [18] T.A. Fox and G. S. West. Fluid-induced loading of cantilevered circular cylinders in a low-turbulence uniform flow. part 1: Mean loading with aspect ratios in the range 4 to 30. *Journal of Fluids and Structures*, 7, 1993.
- [19] E. Achenbach. Distribution of local pressure and skin friction around a circular cylinder in cross-flow up to  $re = 5 \times 10^6$ . *Journal of Fluid Mechanics*, 34:625–639, 1968.
- [20] A. Ayoub and K. Karamcheti. An experiment on the flow past a finite circular cylinder at high subcritical and supercritical reynolds numbers. *Journal of Fluid Mechanics*, 118:1–26, 1982.
- [21] C-W. Park and S-J. Lee. Free end effects on the near wake flow structure behind a finite circular cylinder. *Journal of Wind Engineering and Industrial Aerodynamics*, 88:231–246, 2000.
- [22] R. Porteous, D. J. Moreau, and C. J. Doolan. A review of flow-induced noise

- from finite wall-mounted cylinders. *Journal of Fluids and Structures*, 51:240–254, 2014.
- [23] S. Majumdar and W. Rodi. Three-dimensional computation of flow past cylindrical structures and model cooling towers. *Building and Environment*, 24:3–22, 1989.
- [24] F. R. Menter. Performance of popular turbulence models for attached and separated adverse pressure gradient flows. *AIAA Journal*, 30:2066–2072, 1992.
- [25] F. R. Menter. Two-equation eddy-viscosity turbulence models for engineering applications. *AIAA Journal*, 32:1598–1605, 1994.
- [26] V. Kalro and T. Tezduyar. Parallel 3d computation of unsteady flows around circular cylinders. *Parallel Computing*, 23:1235–1248, 1997.
- [27] Md. M. Rahman, Md. M. Karim, and Md. A. Alim. Numerical investigation of unsteady flow past a circular cylinder using 2-d finite volume method. *Journal of Naval Architecture and Marine Engineering*, 4:27–42, 2007.
- [28] M. C. Ong, T. Utnes, L. E. Holmedal, D. Myrhaug, and B. Petterson. Numerical simulation of flow around a smooth circular cylinder at very high reynolds numbers. *Marine Structures*, 22:142–153, 2009.
- [29] P. Catalano, M. Wang, G. Iaccarino, and P. Moin. Numerical simulation of the flow around a circular cylinder at high reynolds numbers. *International Journal of Heat and Fluid Flow*, 24:463–469, 2003.

- [30] J. Frohlich and W. Rodi. Les of the flow around a circular cylinder of finite height. *International Journal of Heat and Fluid Flow*, 25:537–548, 2004.
- [31] G. Palau-Salvador, T. Stoesser, J. Frhlich, M. Kappler, and W. Rodi. Large eddy simulations and experiments of flow around finite-height cylinders. *Flow, Turbulence and Combustion*, 84:239–275, 2009.
- [32] M. Kappler. *Experimentelle Untersuchung der Umströmung von Kreiszyklindern mit ausgeprgt dreidimensionalen Effekten*. PhD Thesis, Karlsruhe Institute of Technology, Karlsruhe, Germany, February 2002.
- [33] S. P. Singh and S. Mittal. Flow past a cylinder: shear layer instability and drag crisis. *International Journal for Numerical Methods in Fluids*, 47:75–98, 2005.
- [34] S. A. Hambric A. H. Lee, R. L. Campbell. Coupled delayed-detached-eddy simulation and structural vibration of a self-oscillating cylinder due to vortex-shedding. *Journal of Fluids and Structures*, 48:216–234, 2014.
- [35] A. Feymark. *A Large Eddy Simulation Based Fluid-Structure Interaction Methodology with Application in Hydroelasticity*. PhD Thesis, Chalmers University of Technology, Gothenburg, Sweden, May 2013.
- [36] N. M. Sudharsan, K. Murali, and K. Kumar. Finite element analysis of non-linear fluid structure interaction in hydrodynamics using mixed lagrangian-eulerian method. *International Journal of Computational Engineering Science*, 5:425–444, 2004.

- [37] K. F. Cheung A. C. Phadke. Nonlinear response of fluid-filled membrane in gravity waves. *Journal of Engineering Mechanics*, 129:739–750, 2003.
- [38] A. Suleman A. Relvas. Fluidstructure interaction modelling of nonlinear aeroelastic structures using the finite element corotational theory. *Journal of Fluids and Structures*, 22:59–75, 2006.
- [39] A. Combescure F. Abed-Meraim. An improved assumed strain solidshell element formulation with physical stabilization for geometric non-linear applications and elasticplastic stability analysis. *International Journal for Numerical Methods in Engineering*, 80:1640–1686, 2009.
- [40] T. M. Wasfy and A. K. Noor. Modeling and sensitivity analysis of multibody systems using new solid, shell and beam elements. *Computer Methods in Applied Mechanics and Engineering*, 138:187–211, 1996.
- [41] W. Rust and K. Schweizerhof. Finite element limit load analysis of thin-walled structures by ansys (implicit), ls-dyna (explicit) and in combination. *Thin-walled Structures*, 41:227–244, 2003.
- [42] F. K. Benra, H. J. Dohmen, J. Pei, S. Schuster, and B. Wan. A comparison of one-way and two-way coupling methods for numerical analysis of fluid-structure interactions. *Journal of Applied Mathematics*, 2011, 2011.
- [43] U. Langer and H. Yang. Robust and efficient monolithic fluid-structure-interaction solvers. *International Journal for Numerical Methods in Engineering*, 2016.

- [44] L. T. Zhang and M. Gay. Immersed finite element method for fluid-structure interactions. *Journal of Fluids and Structures*, 23:839–857, 2007.
- [45] C. Michler, S. J. Hulshoff, E. H. van Brummelen, and R. de Borst. A monolithic approach to fluidstructure interaction. *Computers & Fluids*, 33:839–848, 2004.
- [46] R. Fithen R. E. Gordnier. Coupling of a nonlinear finite element structural method with a navierstokes solver. *Computers & Structures*, 81:75–89, 2003.
- [47] ANSYS, Canonsburg. *Mechanical APDL Structural Analysis Guide*, release 15 edition, 2013. See also URL <http://www.ansys.com>.
- [48] ANSYS, Canonsburg. *Element Reference Guide*, release 12.1 edition, 2009. See also URL <http://www.ansys.com>.
- [49] X. Gong and R. Moe. On Stress Analysis for a Hyperelastic Material. Technical report, Sulzer Carbomedics Inc., 2002. See also URL <http://www.ansys.net>.
- [50] ANSYS, Canonsburg. *Engineering Data User Guide*, release 15 edition, 2013. See also URL <http://www.ansys.com>.
- [51] ANSYS, Canonsburg. *Mechanical APDL Theory Guide*, release 15 edition, 2013. See also URL <http://www.ansys.com>.
- [52] M. G. Hallam and N. J. Heaf and L. R. Wootton. Dynamics of marine structures: methods of calculating the dynamic response of fixed structures subject to wave and current action. Report No. UR8 by Underwater Engineering Group, Construction Industry Research & Information Association, London, England, 1977.

- [53] L. V. Schmidt. Measurements of fluctuating air loads on a circular cylinder. *Journal of Aircraft*, 2:49–55, 1965.
- [54] G. W., Jr. Jones. Unsteady Lift Forces Generated by Vortex Shedding About A Large, Stationary, And Oscillating Cylinder at High Reynolds Numbers. NASA-TM-X-61214, NASA Langley Research Center; Hampton, VA, United States, 1968.
- [55] J. C. K. Cheung and W. H. Melbourne. Turbulence effects on some aerodynamic parameters of a circular cylinder at supercritical reynolds numbers. *Journal of Wind Engineering and Industrial Aerodynamics*, 14:399–410, 1983.
- [56] S. J. Zan. Experiments on circular cylinders in cross flow at reynolds numbers up to 7 million. *Journal of Wind Engineering and Industrial Aerodynamics*, 96:880–886, 2008.
- [57] T. J. Chung, editor. *Computational Fluid Dynamics*, chapter 21, page 679. Cambridge University Press, Cambridge, 2002. See also URL <http://cambridge.org>.
- [58] D. C. Wilcox. *Turbulence Modeling for CFD*. DCW Industries, Inc., 2006.
- [59] Yunus A. Cengel and John M. Cimbala. *Fluid Mechanics: Fundamentals and Applications*. McGraw-Hill, 2006.
- [60] C. Wieselberger. New Data on the Laws of Fluid Resistance. Technical Note 84, National Advisory Committee for Aeronautics, 1922.
- [61] M. Wang and P. Catalano and G. Iaccarino. Prediction of high Reynolds number

- flow over a circular cylinder using LES with wall modeling. Annual Research Briefs, Center for Turbulence Research, 2001.
- [62] D. Sumner. Flow above the free end of a surface-mounted finite-height circular cylinder: A review. *Journal of Fluids and Structures*, 43:41–63, 2013.
- [63] G. S. West T.A. Fox. Fluid-induced loading of cantilevered circular cylinders in a low-turbulence uniform flow. part 3: Fluctuating loads with aspect ratios 4 to 25. *Journal of Fluids and Structures*, 7:375–386, 1993.
- [64] ESDU. Circular-cylindrical structures: dynamic response to vortex shedding, Part I: calculation procedures and derivation. ESDU 85038, ESDU Int. Ltd., 1990. See also URL <https://www.esdu.com/>.
- [65] N. D. P. Barltrop and A. J. Adams. *Dynamics of Fixed Marine Structures, Third Edition*. Thomson Litho Ltd., East Kilbridge, Scotland, 1991.

# Appendix A

## Velocity Plots for CFD Solutions

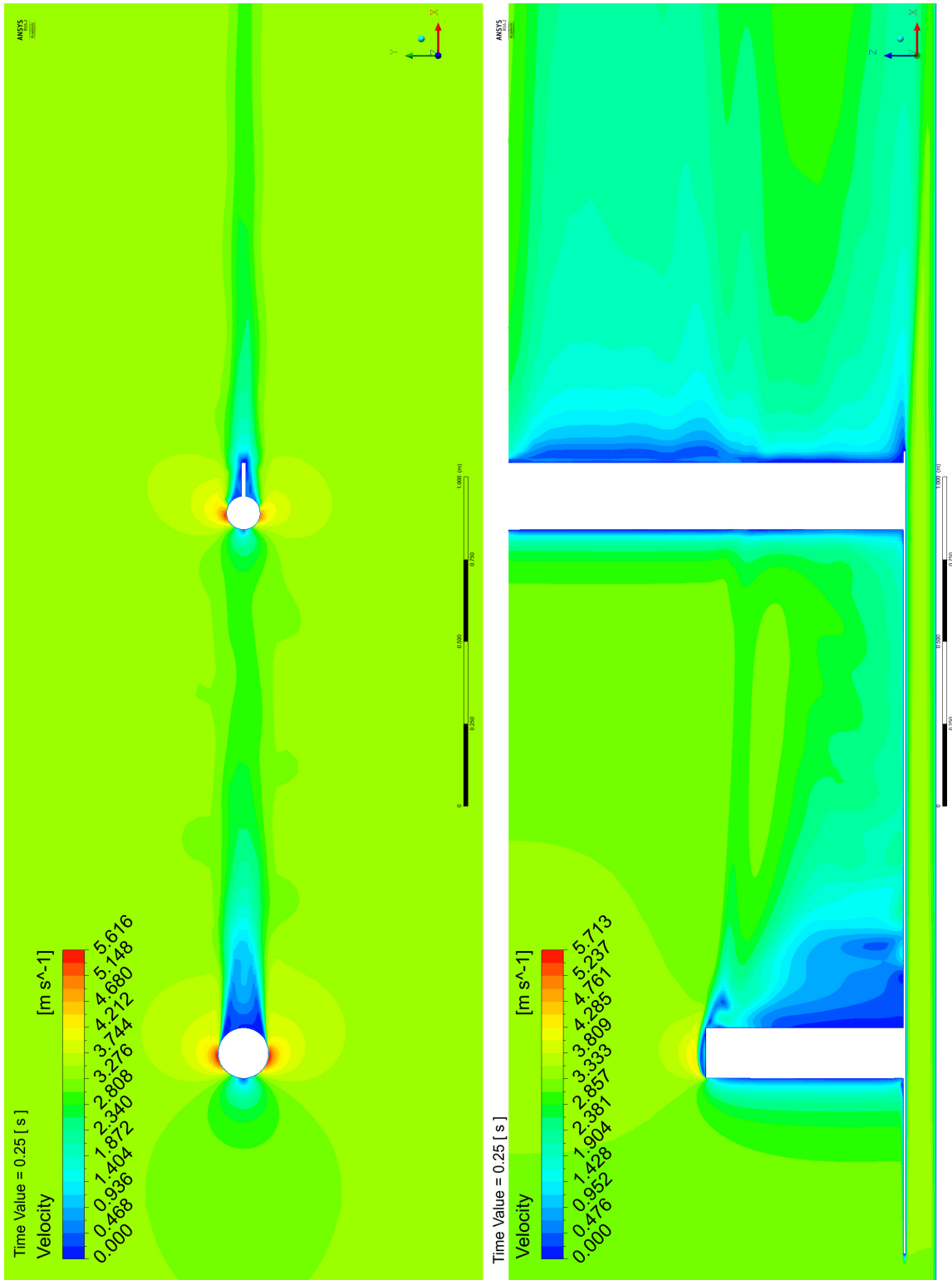


Figure A.1: Velocity plots on horizontal and vertical planes at time=0.25 sec for one-way cases

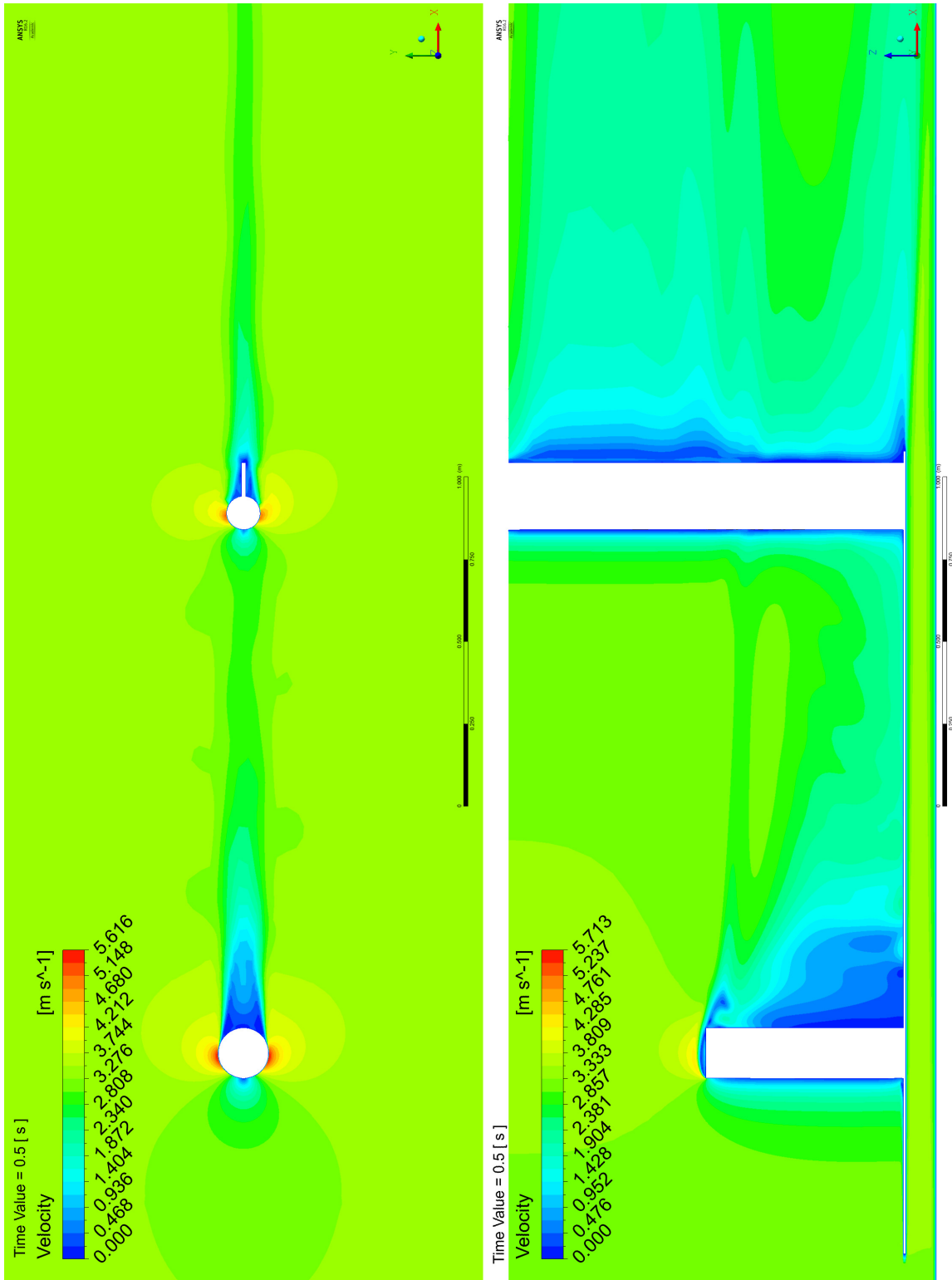


Figure A.2: Velocity plots on horizontal and vertical planes at time=0.50 sec for one-way cases

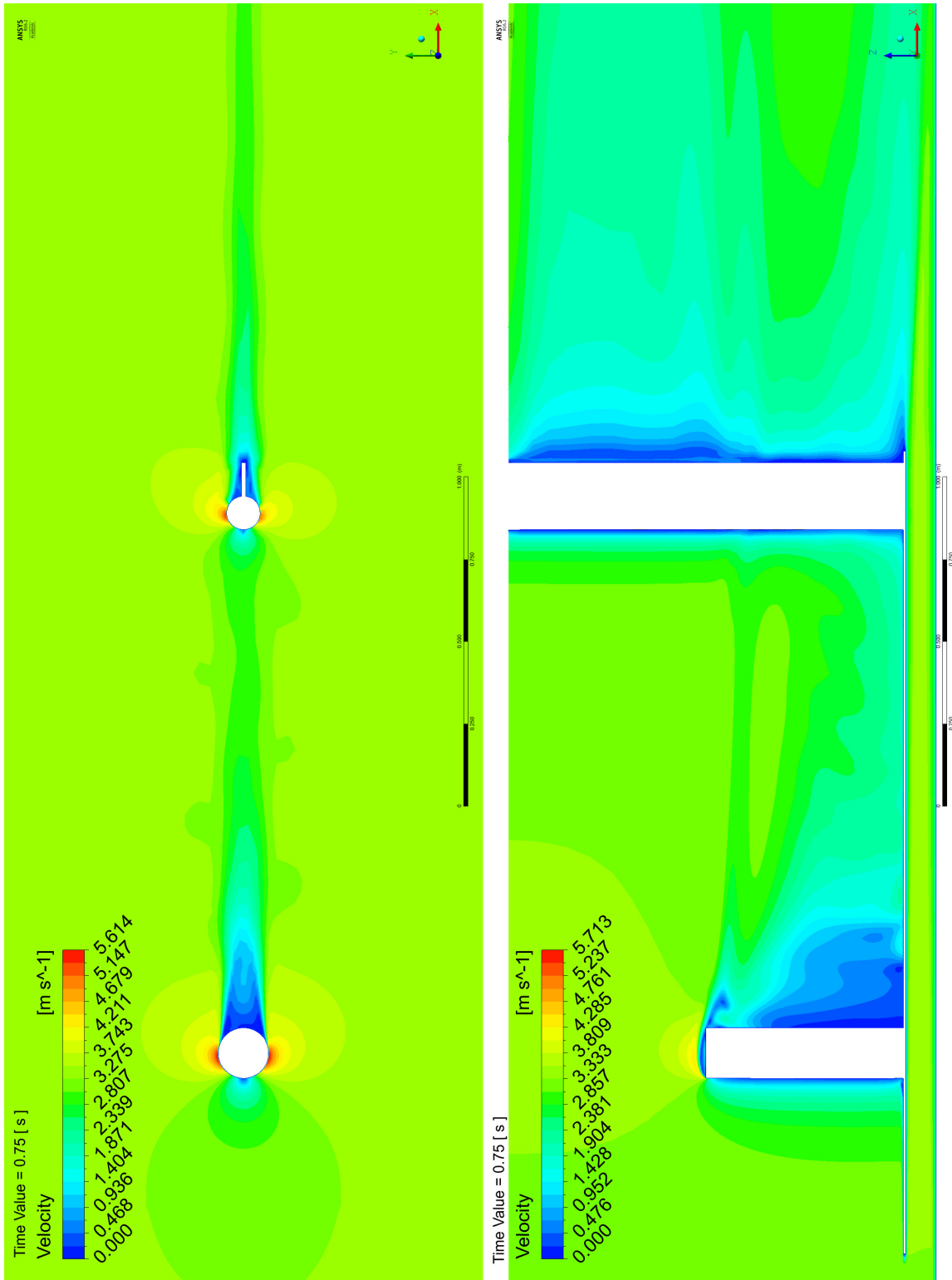


Figure A.3: Velocity plots on horizontal and vertical planes at time=0.75 sec for one-way cases

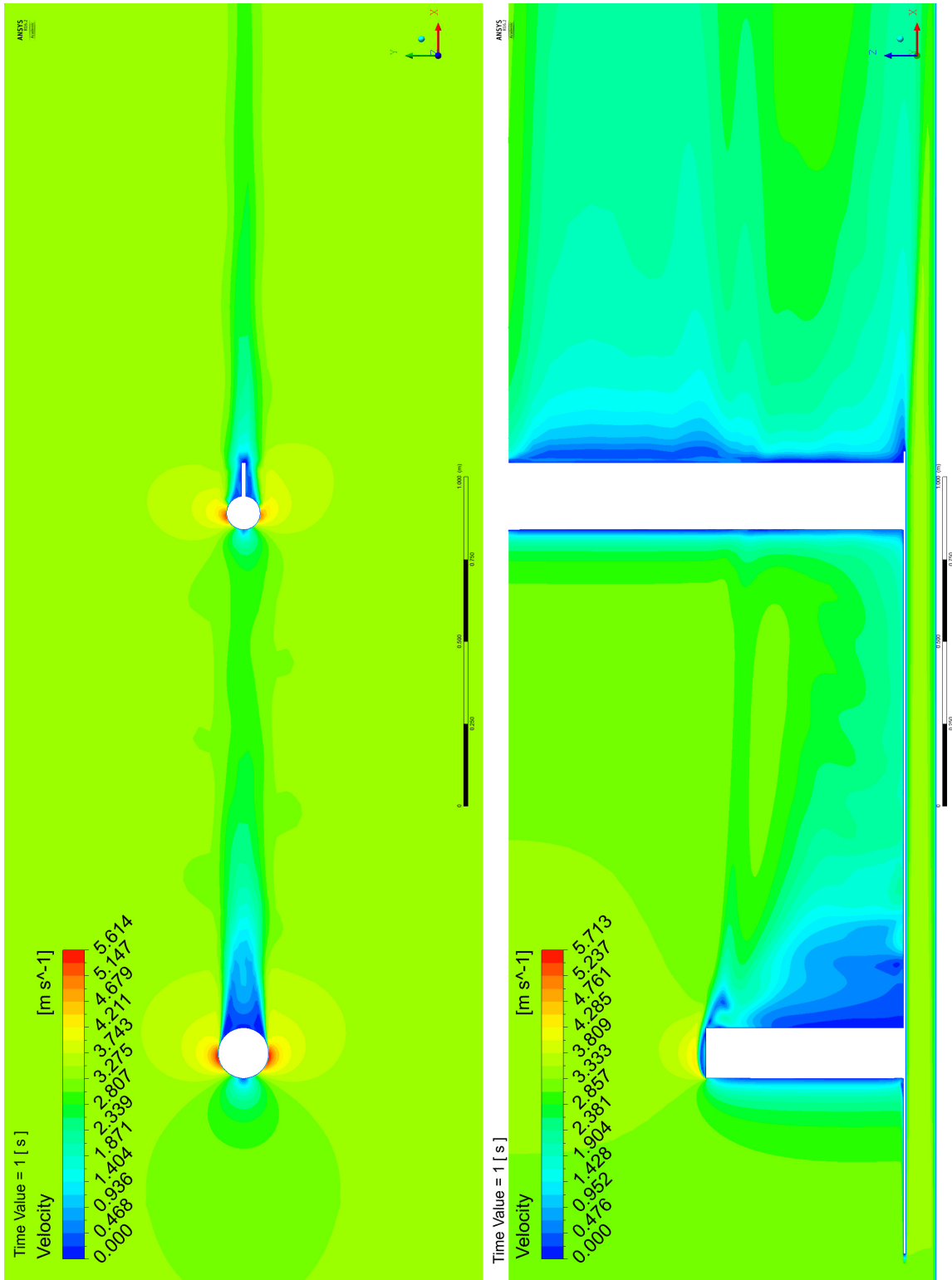


Figure A.4: Velocity plots on horizontal and vertical planes at time=1.00 sec for one-way cases

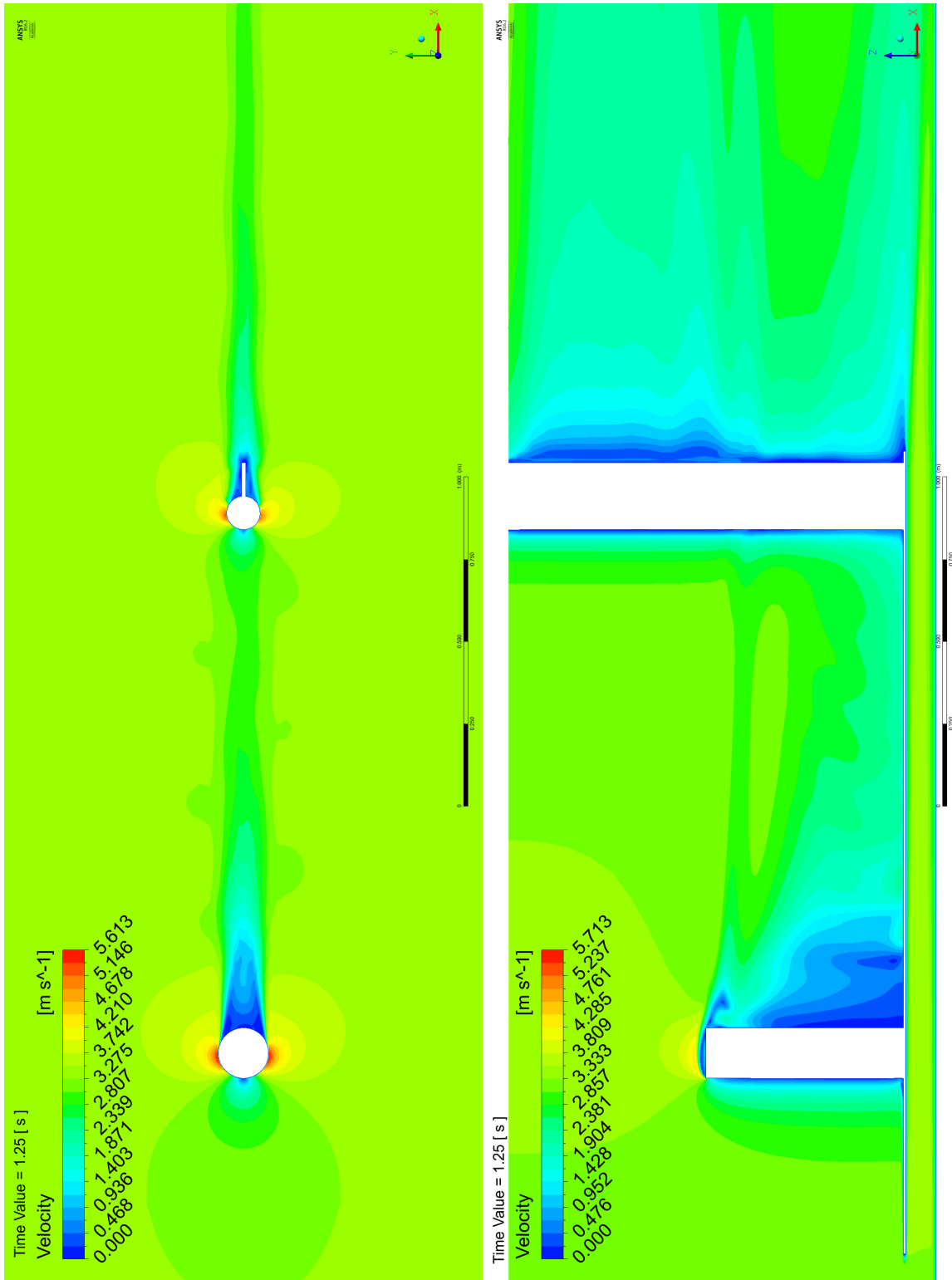


Figure A.5: Velocity plots on horizontal and vertical planes at time=1.25 sec for one-way cases

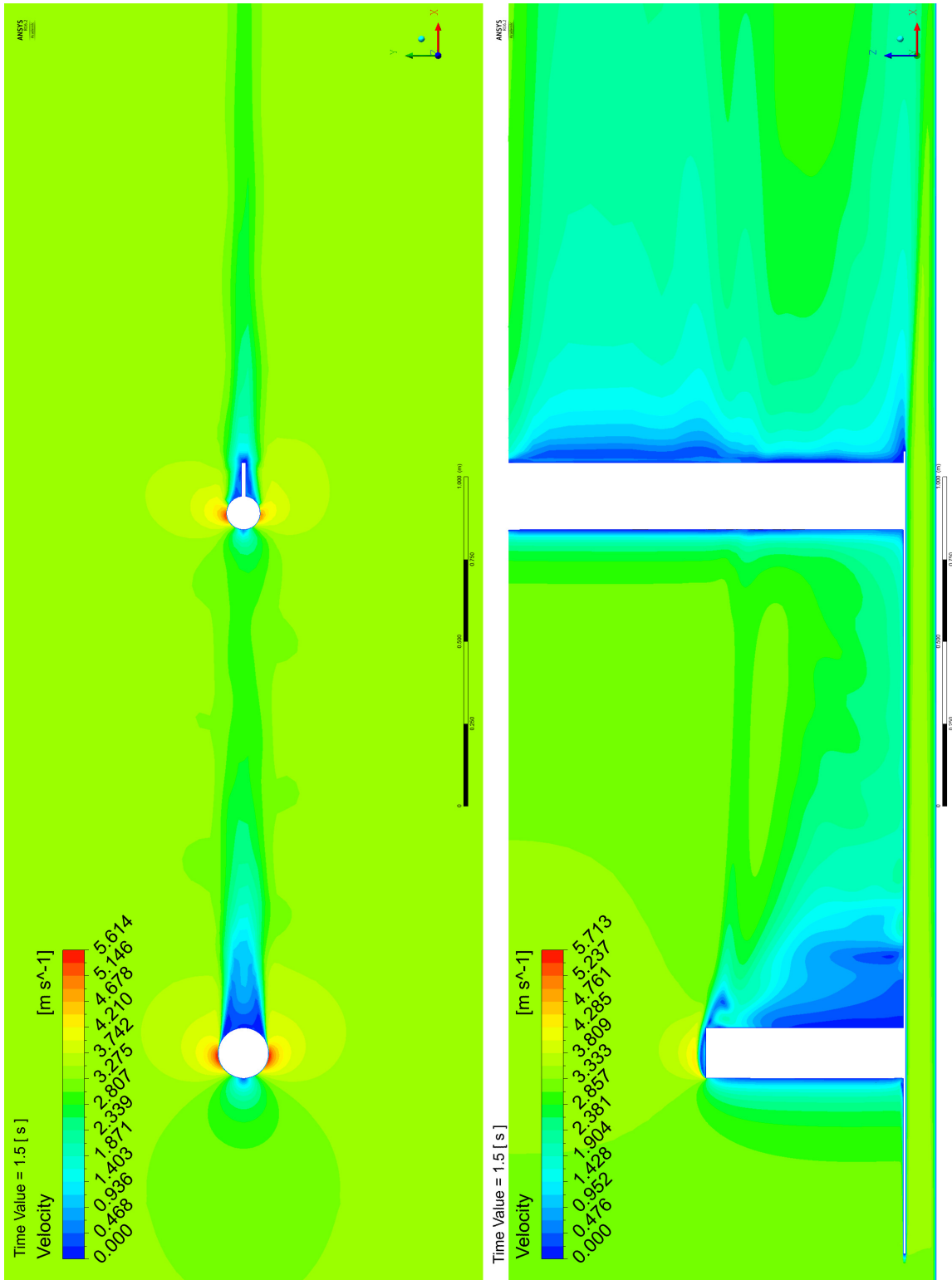


Figure A.6: Velocity plots on horizontal and vertical planes at time=1.50 sec for one-way cases

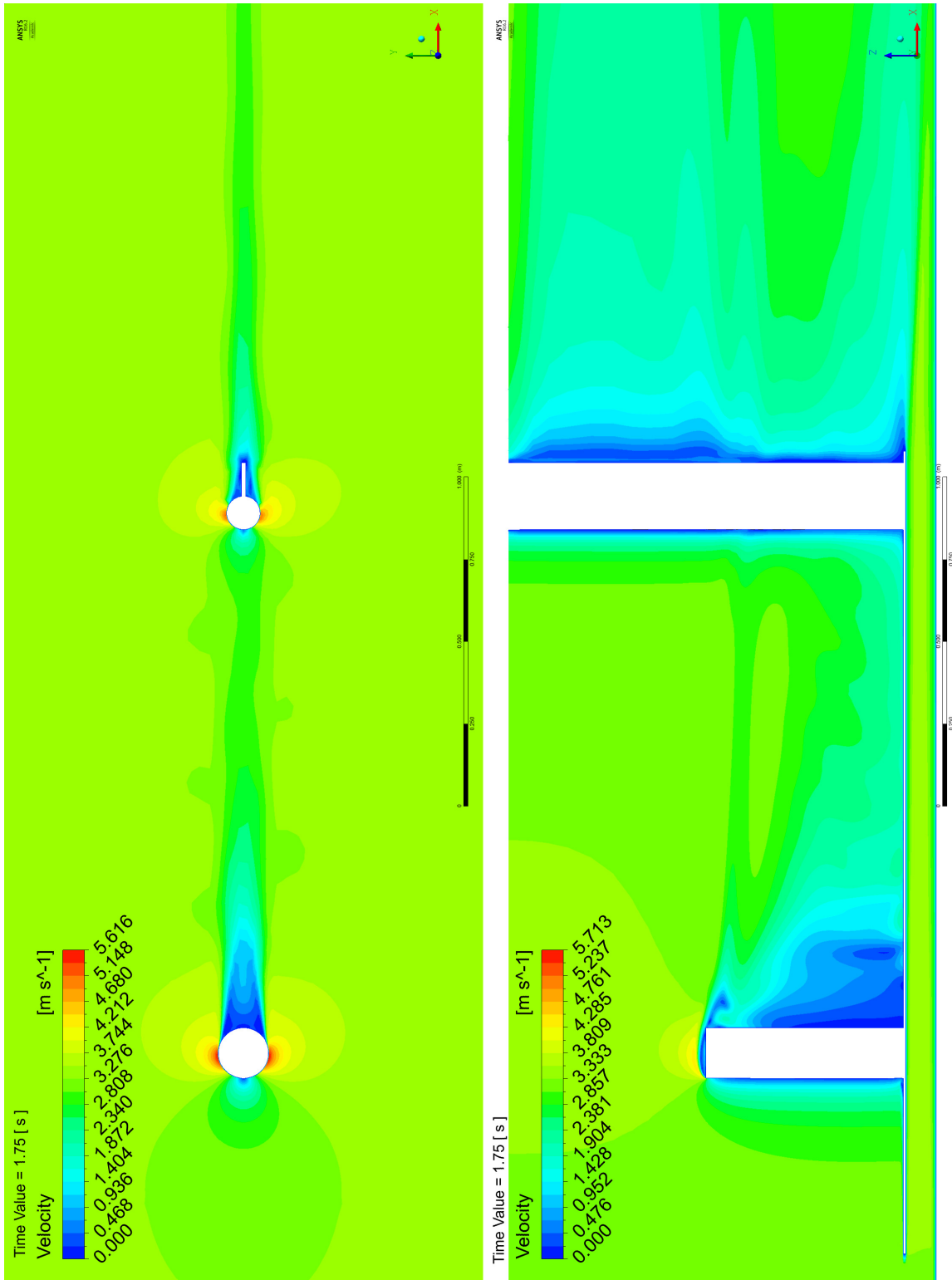


Figure A.7: Velocity plots on horizontal and vertical planes at time=1.75 sec for one-way cases

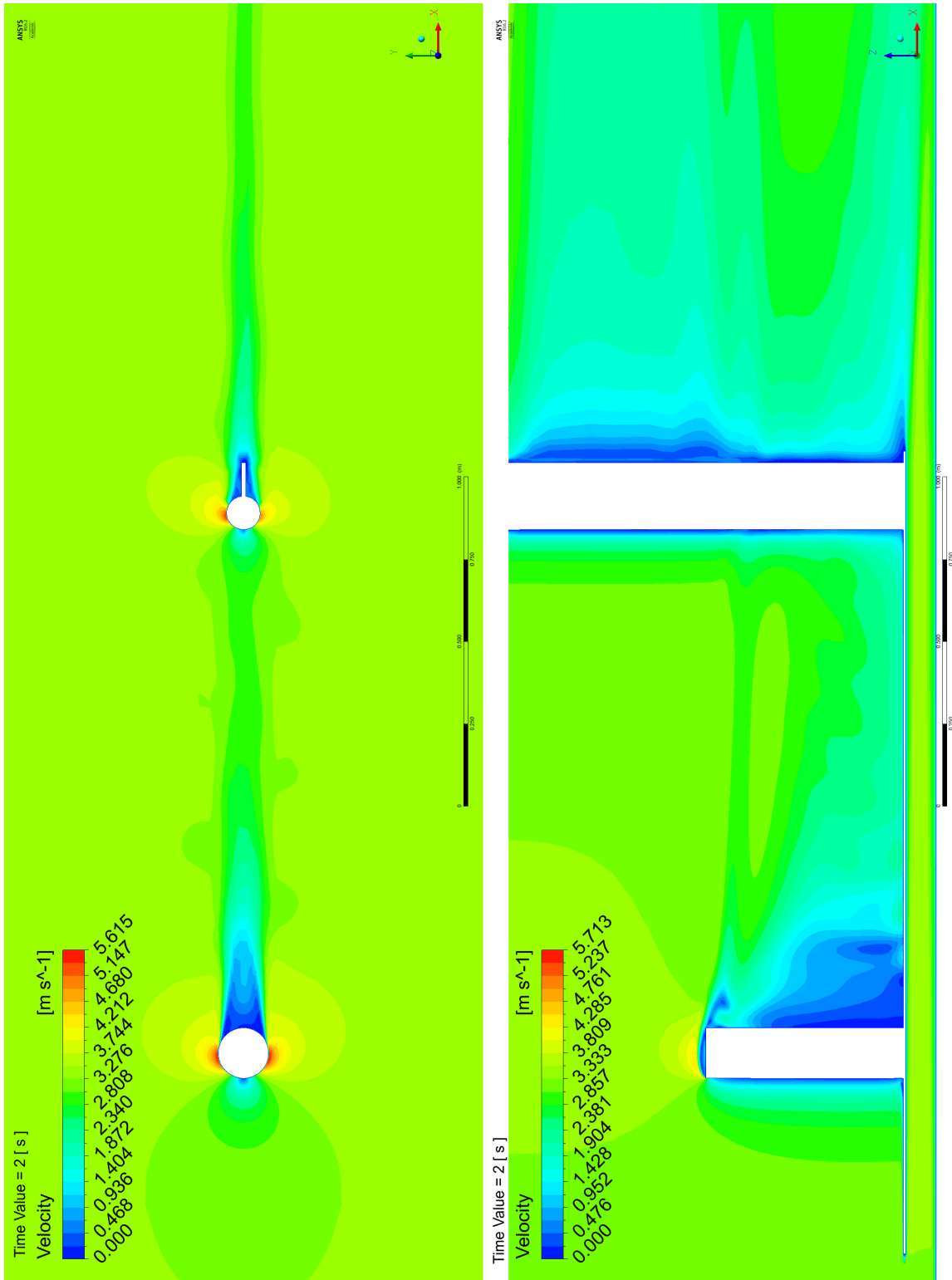


Figure A.8: Velocity plots on horizontal and vertical planes at time=2.00 sec for one-way cases

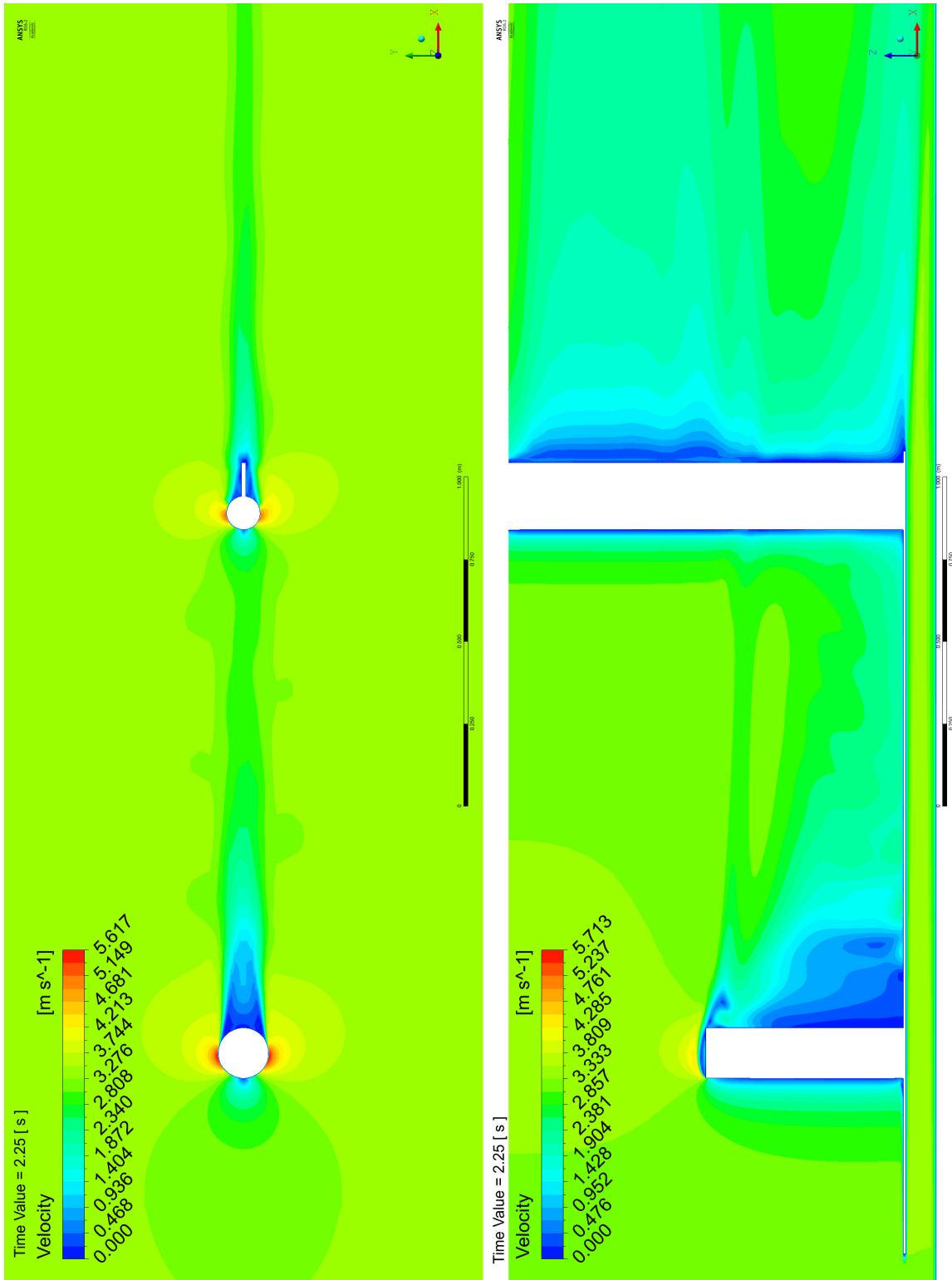


Figure A.9: Velocity plots on horizontal and vertical planes at time=2.25 sec for one-way cases

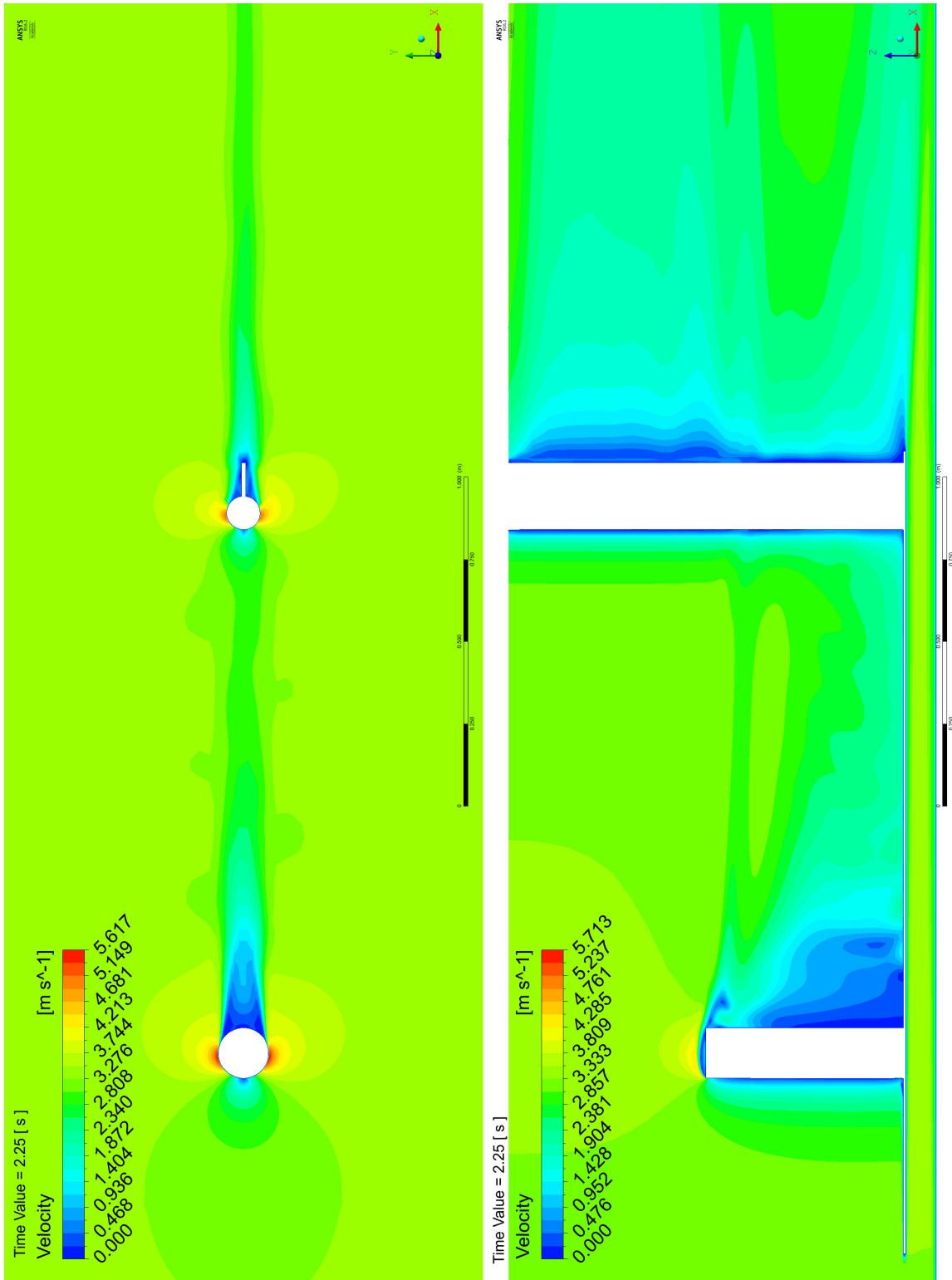


Figure A.10: Velocity plots on horizontal and vertical planes at time=2.50 sec for one-way cases

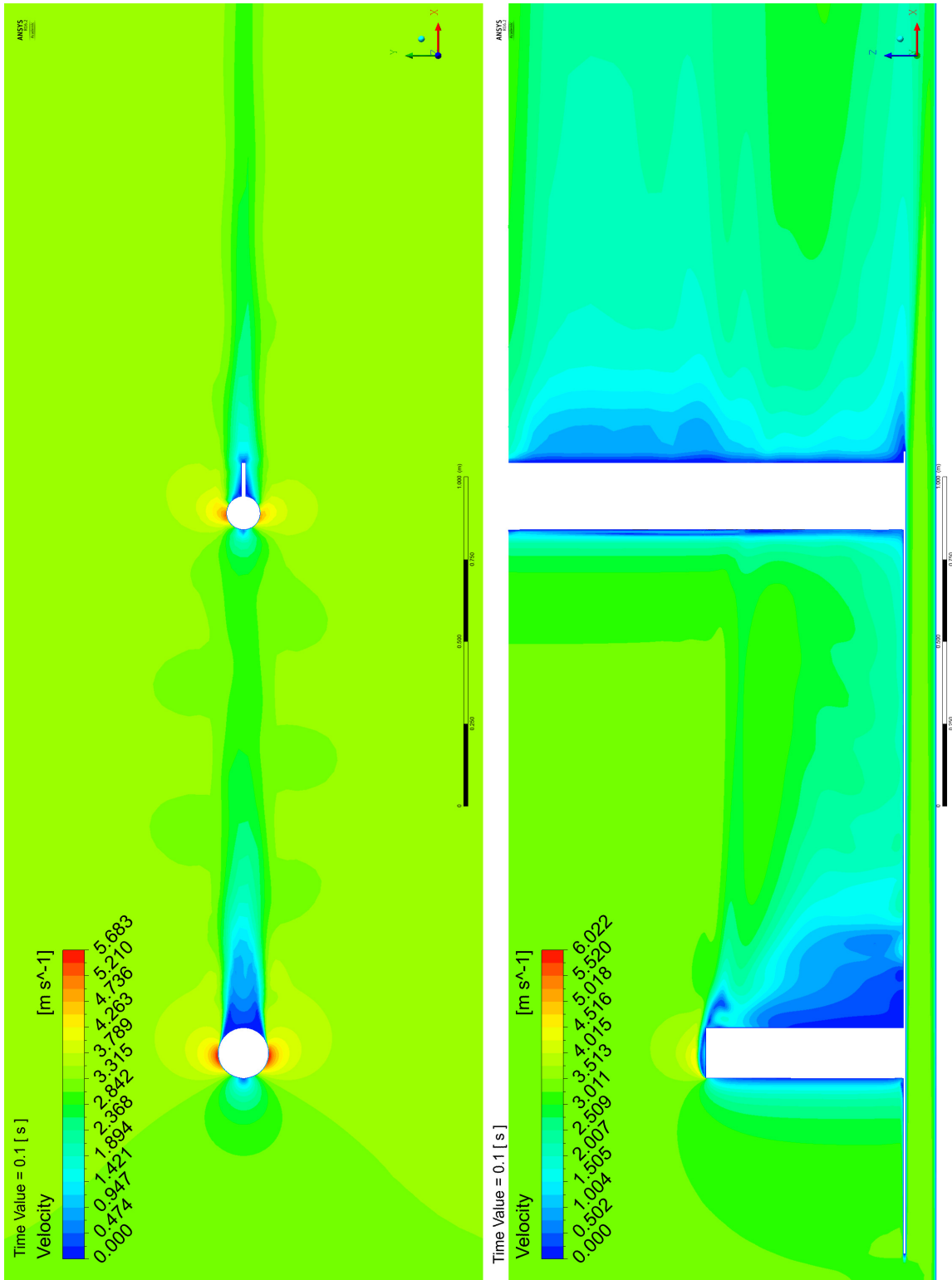


Figure A.11: Velocity plots on horizontal and vertical planes at time=0.10 sec for Case 3

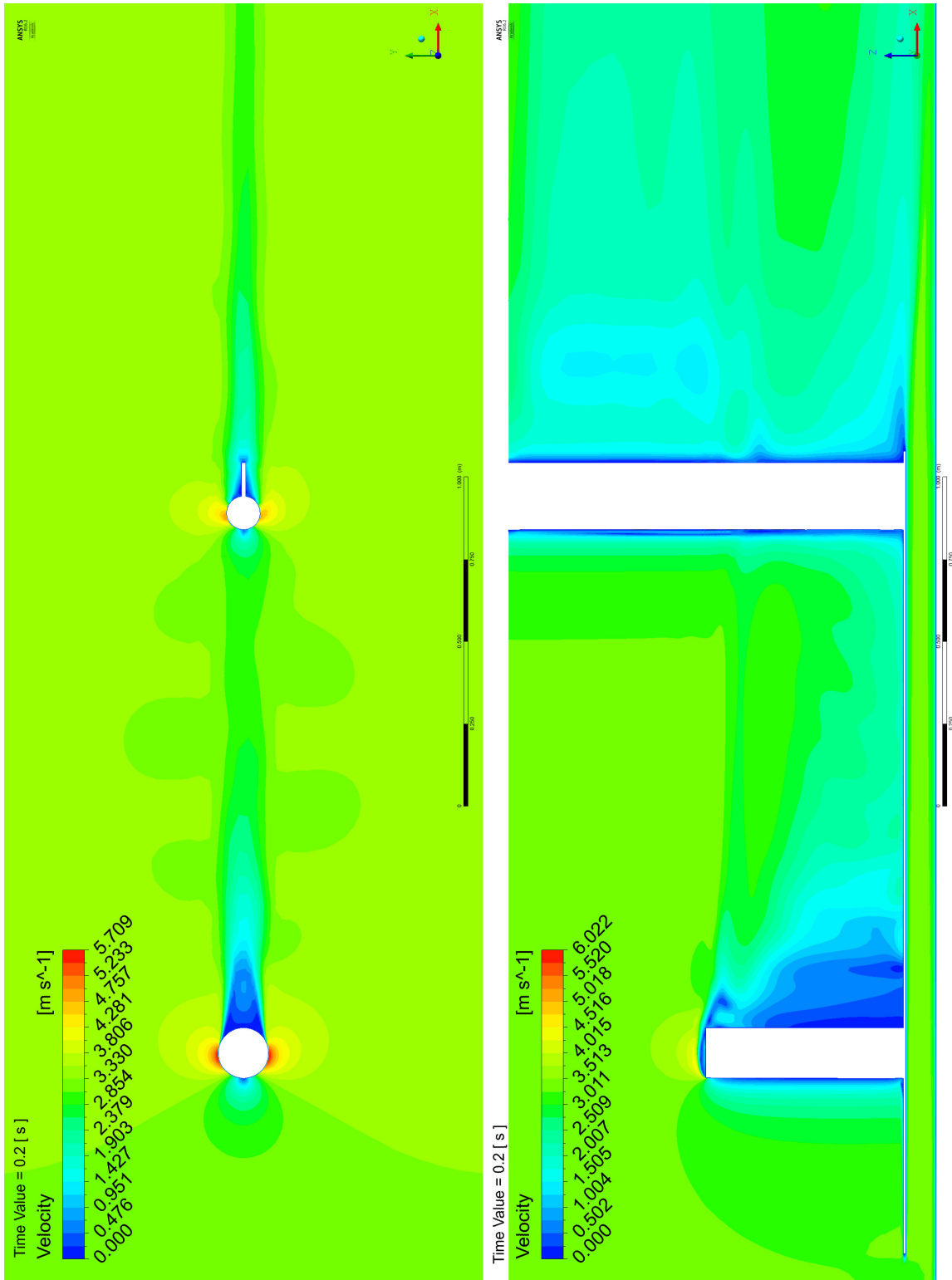


Figure A.12: Velocity plots on horizontal and vertical planes at time=0.20 sec for Case 3

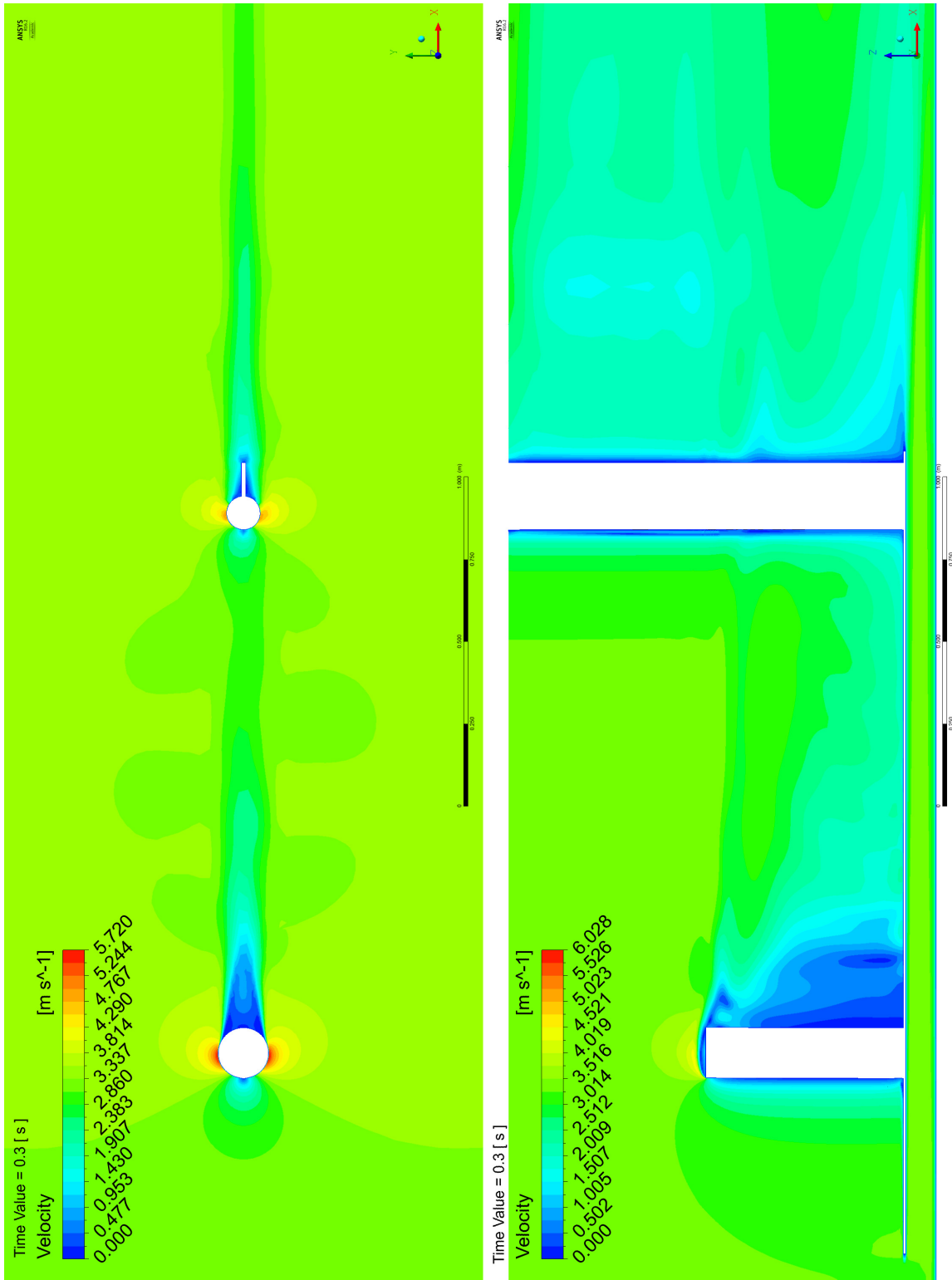


Figure A.13: Velocity plots on horizontal and vertical planes at time=0.30 sec for Case 3

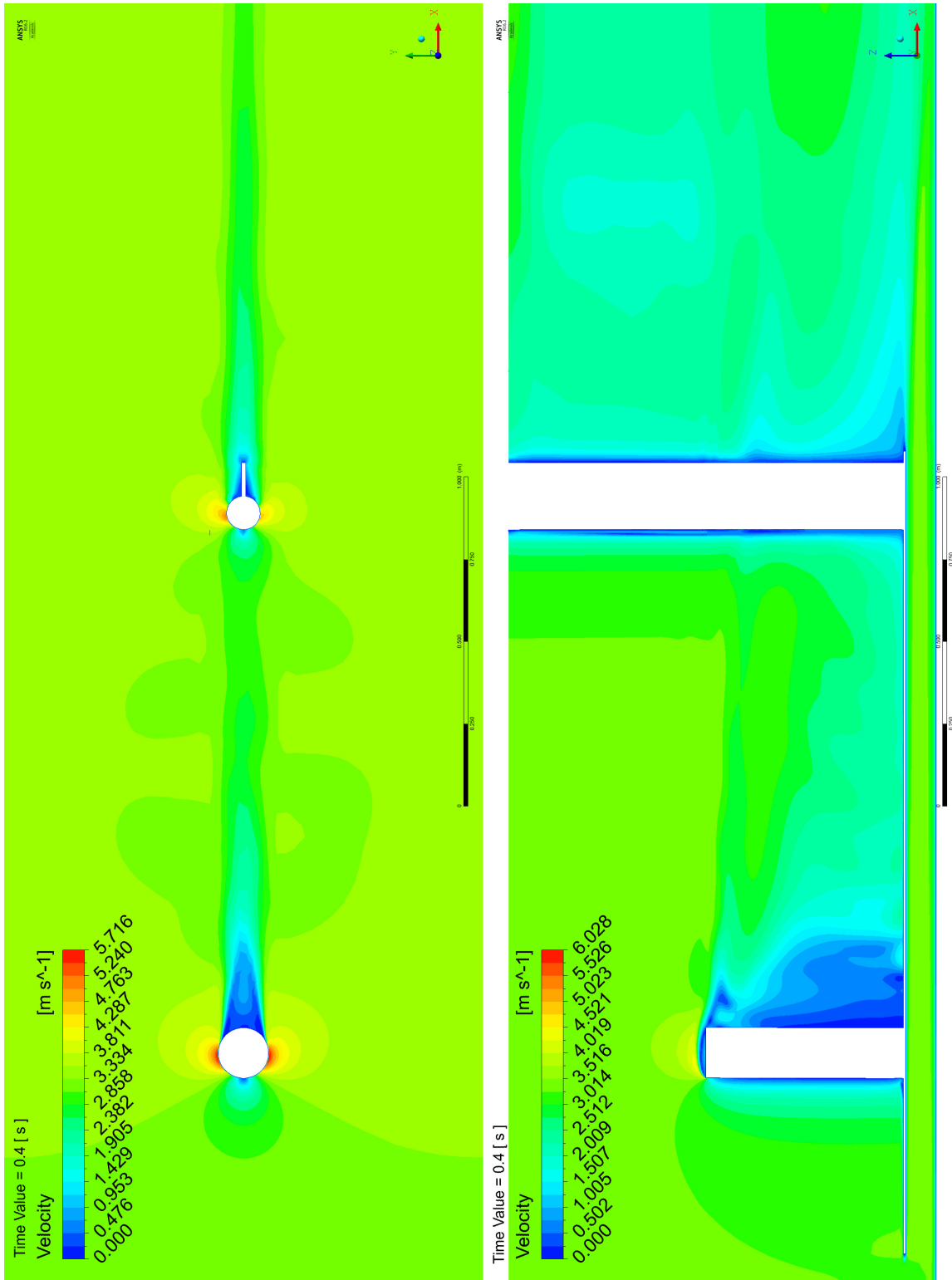


Figure A.14: Velocity plots on horizontal and vertical planes at time=0.40 sec for Case 3

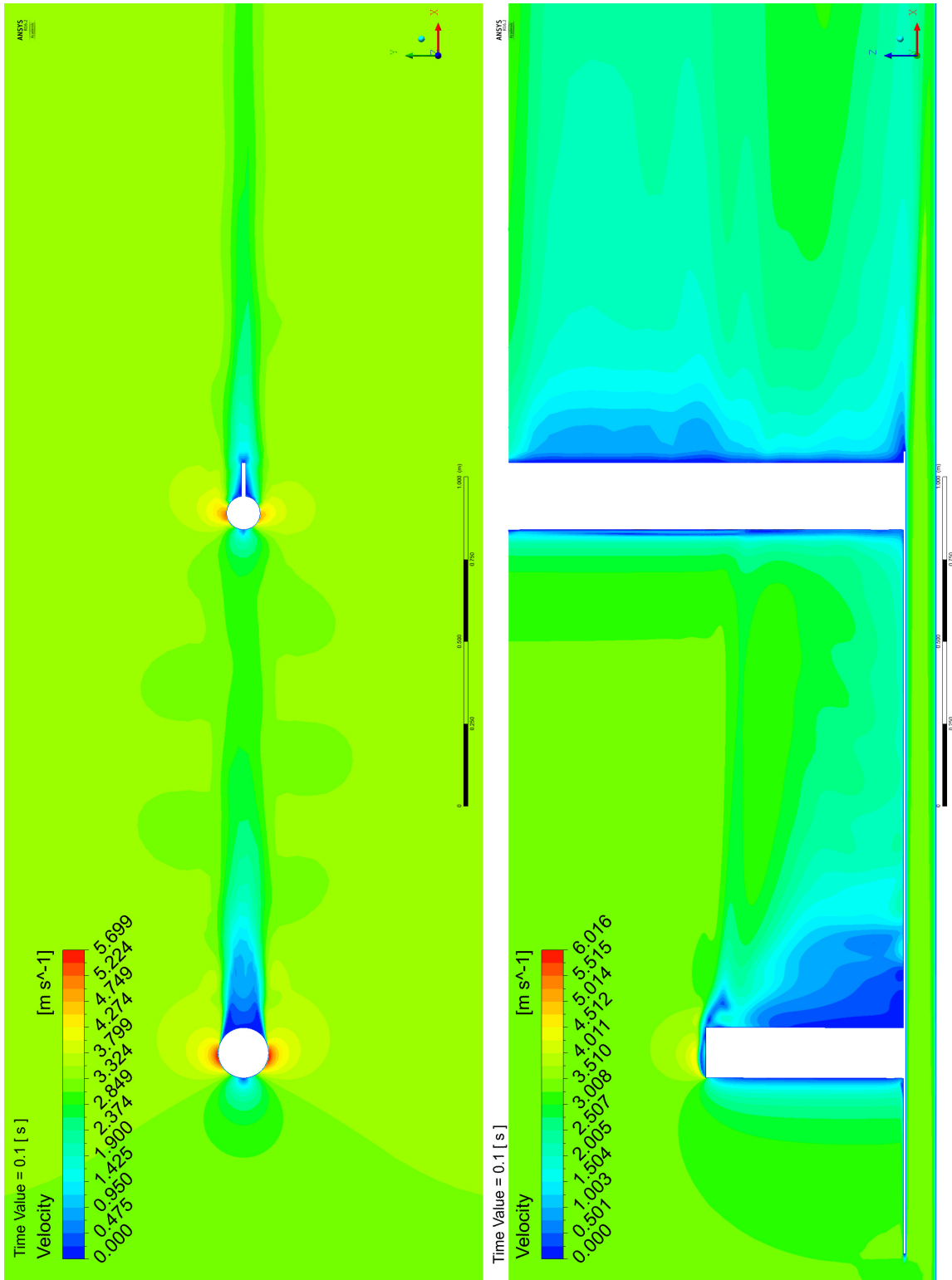


Figure A.15: Velocity plots on horizontal and vertical planes at time=0.10 sec for Case 4

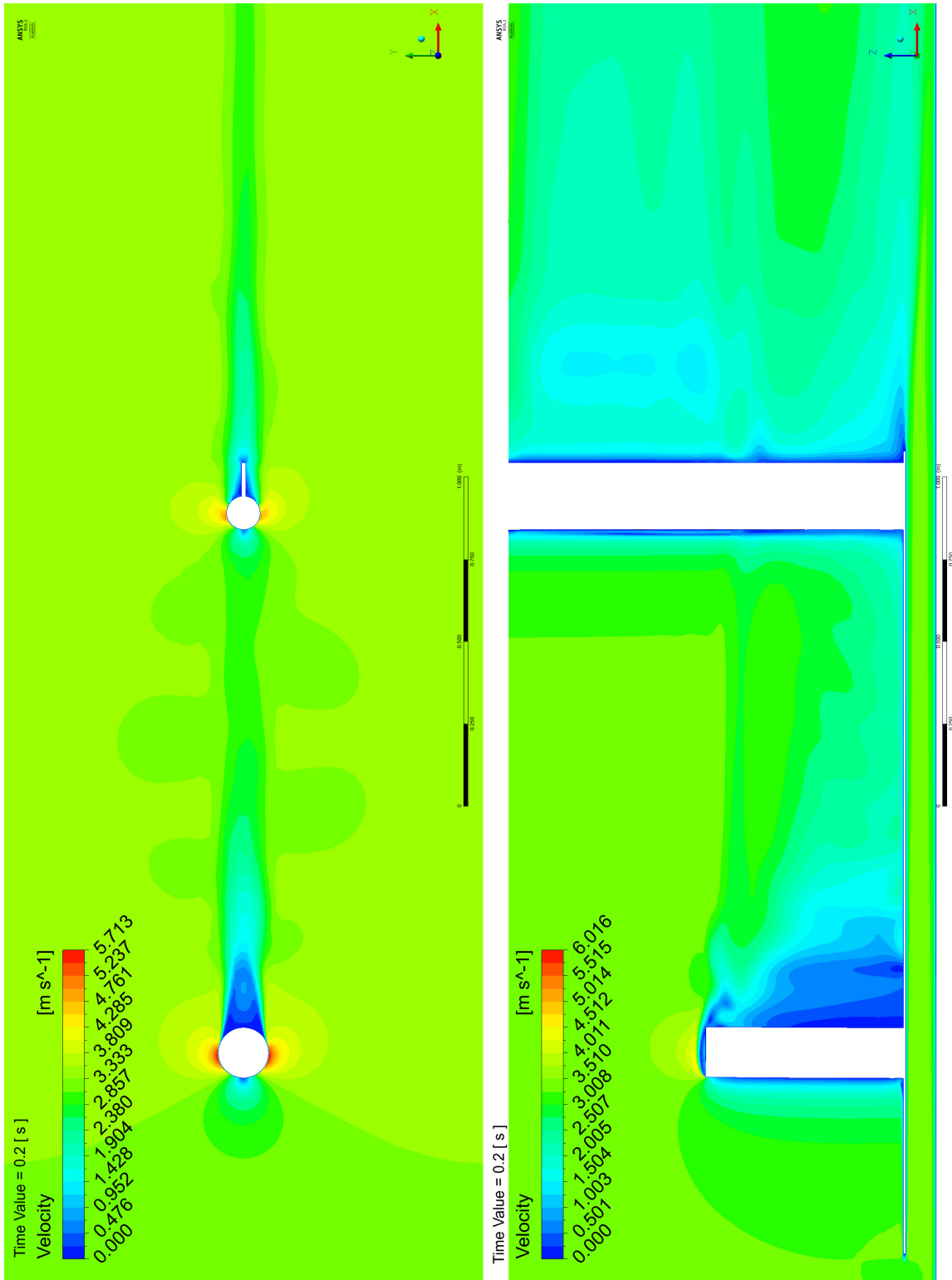


Figure A.16: Velocity plots on horizontal and vertical planes at time=0.20 sec for Case 4

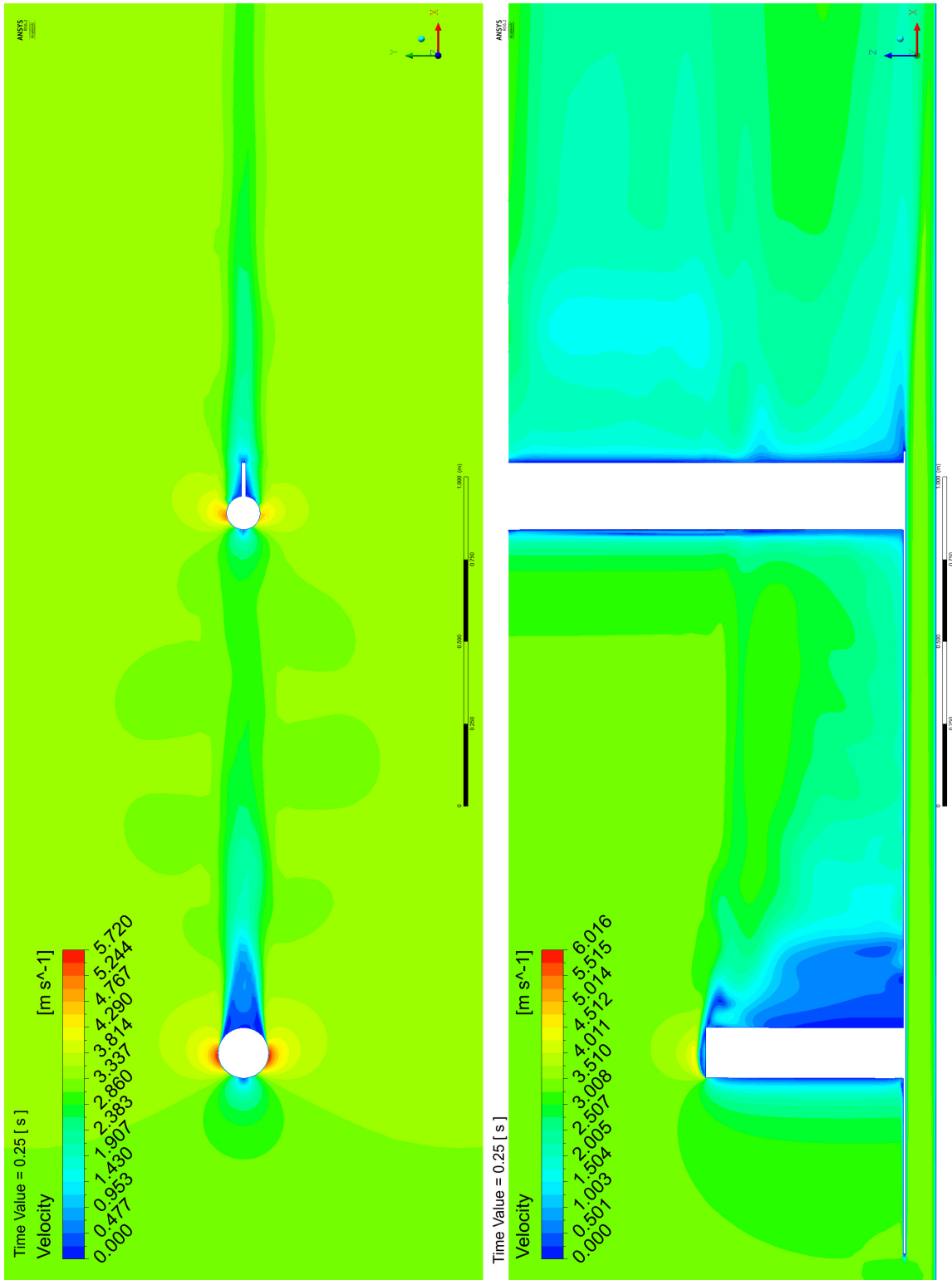


Figure A.17: Velocity plots on horizontal and vertical planes at time=0.25 sec for Case 4

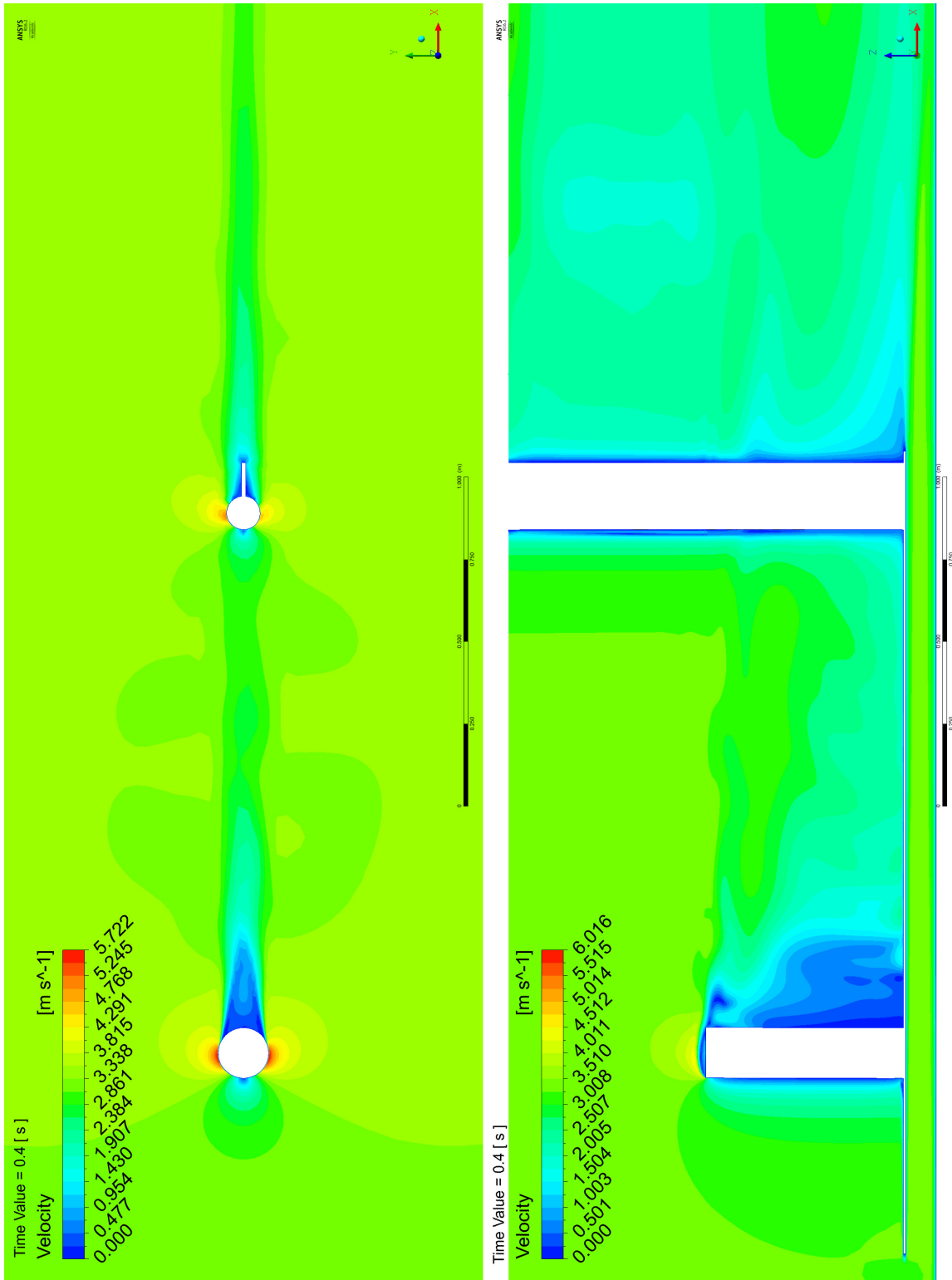


Figure A.18: Velocity plots on horizontal and vertical planes at time=0.40 sec for Case 4